Chapter 1 Introduction

The rapid development of femtosecond pulsed lasers has highlighted the laser science in the past decade. The femtosecond laser is becoming the most powerful instrument for people to research the essentiality of the nature. Femtosecond lasers are powerful tools not only for fundamental research in nonlinear optics, chemical dynamics and laser spectrometry, but also for novel biomedical applications in mini-invasive surgery and tissue imaging.

In parallel to the ongoing development of ultrafast laser system, applications in the medical field are also being studied. Due to the transparency of the human eye to visible and near infrared light, the ocular tissues are ideal objects for laser-based diagnostic and therapeutic applications. In the 1970's, Dr. Fyodorov, who comes from Russia, brought about the practical application of refractive surgery through radial keratotomy (RK). The next procedure is advent as Photorefractive Keratectomy (PRK). Today, the procedural ease, rapid visual rehabilitation, minimal post-operative discomfort, and high predictability in laser assisted in situ keratomileusis (LASIK) have made it the most frequently performed refractive surgical procedure with excimer lasers. Recently, there has been increasing interest in exploring novel applications of fs lasers for refractive surgery [1] [2]. Initiated by multiphoton absorption and laser induced optical breakdown, the high pressure laser plasma non-thermally dissociates the dense corneal tissue thereby enabling mini-invasive intrastromal cornea surgery. The laser-affected region is highly localized, leading to precise ablation with minimized side effects [3]. Theoretically femtosecond lasers offer numerous advantages over excimer lasers, but a fundamental systematical study concerning ultrafast laser tissue interactions is crucial before applying the state of the art laser technology to ophthalmic applications.

Our research group is good in the laser research field. We have already developed a few generations of ultrafast laser systems for medical research. The last one is the outstanding all

solid state femtosecond Nd:glass laser system. [4] I integrated this laser with another Nd:YAG picosecond laser to form the ultrafast laser system for the laser tissue interaction. Although the shortest pulse duration directly produced by a laser up to date is around five femtoseconds [5], the previous study from our group have already proved that a few hundred femtoseconds laser pulse is more suitable for eye surgery. So the most interesting point of this study focuses on the laser tissue interaction with the pulse width of the ultrafast laser pulses ranging from 800 femtoseconds to 20 picoseconds. The results from this dissertation also concern another Yb:KYW femtosecond laser.

This dissertation is organized into three parts. The first part introduces the three laser systems involved in this study. All of them are diode pumped all solid-state lasers. The principles for ultrafast lasers are presented. The chirped pulsed amplification (CPA) system is introduced. The novel thin disk Yb:KYW regenerative amplifier system is also described. The second part includes the theoretical concepts about the laser tissue interaction. Since we used the multi-photon microscope to evaluation the ablation effect, the basic concept about the second harmonic generation is presented in second part. The third part is the results of my systematical experiments and the discussion. This study confirmed in a new way that the plasma mediated ablation in the cornea is a function of laser pulse width. Namely the plasma spark and the second harmonic generation signal were detected at the same time. The ablation threshold is proportional to the square root of the laser pulse width, which is consistent with previous studies. The dependence of the corneal ablation threshold on the depth of the stroma is not significant in the first 200 μm.

Chapter 2 All-Solid-State Laser Systems

In this chapter we introduce some basic concepts of the ultra fast lasers. The group velocity dispersion compensation is important for controlling the pulse width in an ultra fast laser system. This aspect is always given careful consideration when designing such a system. This is the first part of this chapter. The principle of ultra short pulses is also introduced. The last part is about our ultra fast laser systems that were used in our experiments.

2.1 Introduction to ultra short laser pulses

2.1.1 Femtosecond optics

2.1.1.1 Group velocity

The group velocity of a wave is the velocity with which the variations in the shape of the wave's amplitude (known as the modulation or envelope of the wave) propagate through space.

Consider a dispersive atomic medium, or any other kind of dispersive wave propagating system, such as a transmission line, optical fiber, or waveguide. By "dispersive" here we mean any linear system in which the propagation constant $\Psi(\omega)$ as a function of frequency has any form other than a straight line through the origin, i.e., $\Psi = \omega/c$.

Suppose a gaussian pulse with the form

$$\varepsilon_0(t) = \exp(-\Gamma_0 t^2 + j\omega_0 t),\ \tilde{E}_0(\omega) = \exp[-\frac{(\omega-\omega_0)^2}{4\Gamma_0}]$$

passes into such a dispersive system, the output pulse after traveling any arbitrary distance z through the system is given by[6]:

$$\varepsilon(z,t) = \exp[\, j(\omega_0 t - \psi(\omega_0)z] \times \exp[-\Gamma(z) \times (t - \Psi'(\omega_0)z)^2]$$

$$= \exp[\, j\omega_0 (t - \frac{z}{v_\phi(\omega_0)})] \times \exp[-\Gamma(z) \times (t - \frac{z}{v_g(\omega_0)})^2]$$

where $\Gamma(z)$ is the modified gaussian pulse parameter after traveling a distance z, and where $v_\phi(\omega_0) \equiv \omega_0 / \Psi(\omega_0)$ and $v_g(\omega_0) \equiv 1/\Psi'(\omega_0)$

the second term in the above equation expresses that the pulse envelop, which retains its gaussian shape but with a modified pulse parameter $\Gamma(z)$, is delayed by the group delay time t_g given by

group delay $t_g = \dfrac{z}{v_g(\omega_0)} = \Psi'(\omega_0)z$

in other words, the pulse envelop appears to move forward with a mid band group velocity $v_g(\omega_0)$ given by

group velocity $v_g(\omega_0) = \dfrac{z}{\Psi'(\omega_0)z} = \dfrac{1}{(d\Psi/d\omega)}\Big|_{\omega=\omega_0} = (\dfrac{d\omega}{d\Psi})_{\omega=\omega_0}$

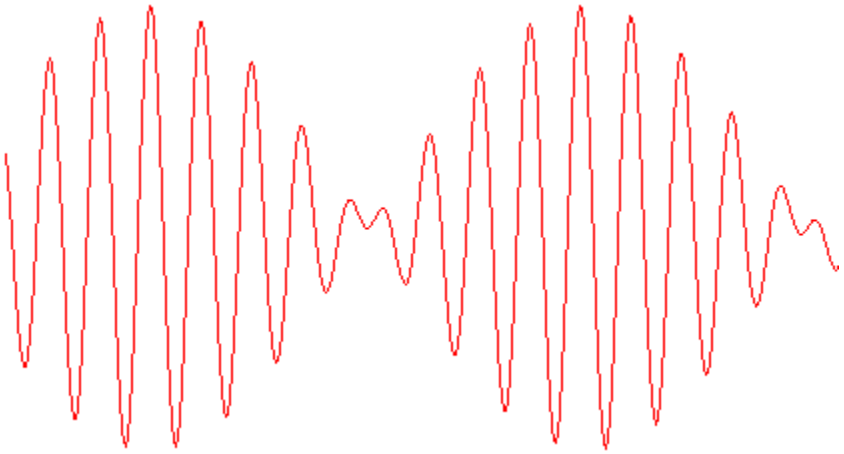

Figure 2.1: Group velocity.

2.1.1.2 Group velocity dispersion

The group velocity itself is usually a function of the wave's frequency. This results in the group velocity dispersion (GVD), which causes a short pulse of light to spread in time as a result of different frequency components of the pulse traveling at different velocities.

Consider the basic wave equation for a one dimensional signal transmission in a dispersive medium, the equation for the pulse envelope $\tilde{E}(z,t)$ given by [6]

$$\frac{\partial \tilde{E}(z,t)}{\partial z}+\frac{1}{v_g}\frac{\partial \tilde{E}(z,t)}{\partial t}-j\frac{\Psi''}{2}\frac{\partial^2 \tilde{E}(z,t)}{\partial t^2}=0$$

where v_g and Ψ'' are both evaluated at midband $\omega = \omega_0$.

If the third term in this equation equals zero, it is obvious that this equation is satisfied by any solution of the form $\tilde{E}(z,t) \equiv \tilde{E}(z-v_g t)$. This is the group velocity concept for propagation of the pulse envelope $\tilde{E}(z,t)$. It applies to much more than just the gaussian pulses.

If the third term in this equation is not equal zero, then the propagation system will have a “group velocity dispersion”, in other words a variation of group velocity with frequency. In the time domain, the term $j\frac{\Psi''}{2}\frac{\partial^2 \tilde{E}(z,t)}{\partial t^2}$ acts like a kind of generalized complex diffusion term for the pulse envelope $\tilde{E}(z,t)$. It leads to pulse broadening, pulse compression, and pulse reshaping effects.

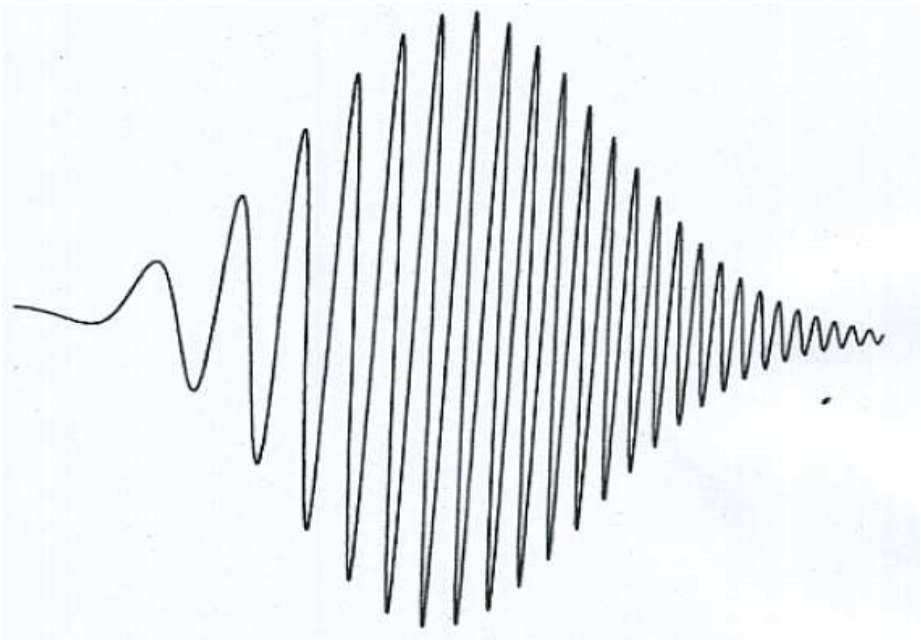

Figure 2.2: Group velocity dispersion.

2.1.1.3 Group velocity dispersion through angular dispersion

Through utilizing the spatial distribution of the frequency components behind the dispersive element, angular dispersion has been advantageously used for a long time to resolve spectra or for spectral filtering. Angular dispersion has the property of introducing group velocity dispersion, this is interesting in connection with femtosecond optics. This seems to be an undersired effect at first glance. However, optical devices based on angular dispersion can be designed which allow a continuous tuning of group velocity dispersion. This idea was first introduced for the compression of chirped pulses with diffraction gratings [7]. The concept was later generalized to prisms and prism sequences [8]. Simple examples for two and four prism sequences are given in a paper of R. L. Fork [9]. From a general point of view, the diffraction problem can be treated by solving the corresponding Fresnel integrals[10]; [11]; [12]. Another successful method is to analyze the sequence of optical elements by ray optical techniques and to calculate the optical beam path

P as a function of frequency. We expect the response of any linear element to be of the form:

$$R(\Omega)e^{-i\Psi(\Omega)}$$

Where the phase delay Ψ is related to the optical pathlength P_{OL} through

$$\Psi(\Omega)=\frac{\Omega}{c}P_{OL}(\Omega)$$

We assume that $R(\Omega)$ is to be constant over the spectral range of interest. So that it will be neglected. We know that non zero terms $\left[\left(d^n/d\Omega^n\right)\Psi\neq 0\right]$ of order n$\geqslant$2 are responsible for changes in the complex pulse envelope. In particular

$$\frac{d^2}{d\Omega^2}\Psi(\Omega)=\frac{1}{c}(2\frac{dP_{OL}}{d\Omega}+\Omega\frac{d^2P_{OL}}{d\Omega^2})=\frac{\lambda^3}{2\pi c^2}\frac{d^2P}{d\lambda^2}$$

is related to the group velocity dispersion parameter.

We can derive the relation between angular dispersion and group velocity dispersion from the following intuitive approach. Considering a light ray, which is incident onto an optical element at point Q, as shown in Figure 2.3.

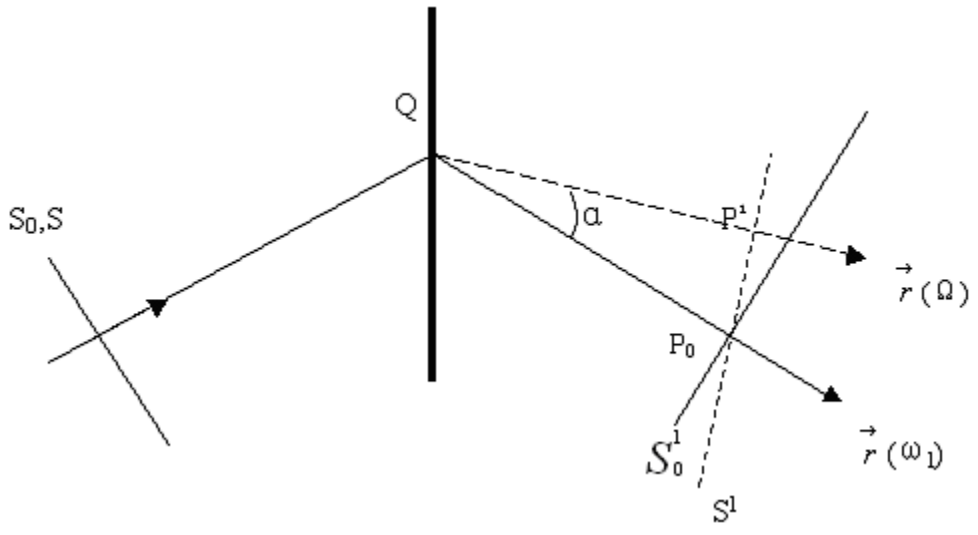

Figure 2.3: Group velocity dispersion introduced by angular dispersion.

At this point we do not specify the element, but just assume that it causes angular dispersion. Thus, different spectral components originate at Q under different angles. The center frequency ω_1 of the spectrum is described as one ray and an arbitrary frequency Ω of the spectrum is corresponding to another ray as shown in figure 2.3. The planes S, S_0 and S^1, $S_0{}^1$ are perpendicular to the ray direction and represent plane wave fronts of the incident light and diffracted light respectively. Suppose P_0 is our point of reference and is located on $\vec{r}(\omega_1)$ where $\overline{QP_0}$ =l.

A wavefront S^1 of $\vec{r}(\Omega)$ at P^1 is assumed to intersect $\vec{r}(\omega_1)$ at P_0. The optical pathlength $\overline{QP^1}$ is

$\overline{QP^1}$ =$P_{OL}(\Omega)$=$P_{OL}(\omega_1)$cos α =lcos α

Which induces the phase delay as

$$\Psi(\Omega) = \frac{\Omega}{c} l \cos\alpha$$

The dispersion constant responsible for group velocity dispersion can be achieved by twofold derivation with respect to Ω:

$$\left.\frac{d^2\Psi}{d\Omega^2}\right|_{\omega_l} = -\frac{l}{c}\left\{\sin\alpha\left[2\frac{d\alpha}{d\Omega}+\Omega\frac{d^2\alpha}{d\Omega^2}\right]+\Omega\cos\alpha\left(\frac{d\alpha}{d\Omega}\right)^2\right\}\Bigg|_{\omega l} \approx -\frac{l\omega_l}{c}\left(\left.\frac{d\alpha}{d\Omega}\right|_{\omega l}\right)^2 \qquad (2.1)$$

Where ω_1 represents the center frequency of the pulse ω_1 for which sin α <<1. The quantity $\left(d\alpha/d\Omega\right)\big|_{\omega l}$, responsible for angular dispersion, is a characteristic of the actual optical device to be considered. The dispersion parameter is always negative independent of the sign of $d\alpha/d\Omega$ and the fact that the dispersion increases with increasing distance from the diffraction point. Therefore angular dispersion always introduces negative group velocity dispersion.

Differentiation of the above equation results in the third dispersion order:

$$\left.\frac{d^3\Psi}{d\Omega^3}\right|_{\omega l} = -\frac{l}{c}\left\{\cos\alpha\left[3\left(\frac{d\alpha}{d\Omega}\right)^2 + 3\Omega\frac{d\alpha}{d\Omega}\frac{d^2\alpha}{d\Omega^2}\right] + \sin\alpha\left[3\frac{d^2\alpha}{d\Omega^2} + \Omega\frac{d^3\alpha}{d\Omega^3} - \Omega\left(\frac{d\alpha}{d\Omega}\right)^3\right]\right\}\right|_{\omega l}$$

$$\approx -\frac{3l}{c}\left[\left(\frac{d\alpha}{d\Omega}\right)^2 + \Omega\frac{d\alpha}{d\Omega}\frac{d^2\alpha}{d\Omega^2}\right]\Bigg|_{\omega l}$$

Prisms and gratings are the most widely used optical devices for angular dispersion. To determine the dispersion introduced by them we just need to specify the quantity $\alpha(\Omega)$ in the expressions derived above.

2.1.1.4 Group velocity dispersion introduced by prisms

In most cases, one likes to control the group velocity dispersion, and at the same time avoid the beam divergence introduced by angular dispersion. The simplest practicable solution to this problem is a sequence of two identical prisms that is adjusted for the angular dispersion to be compensated, as in Figure 2.4 below.

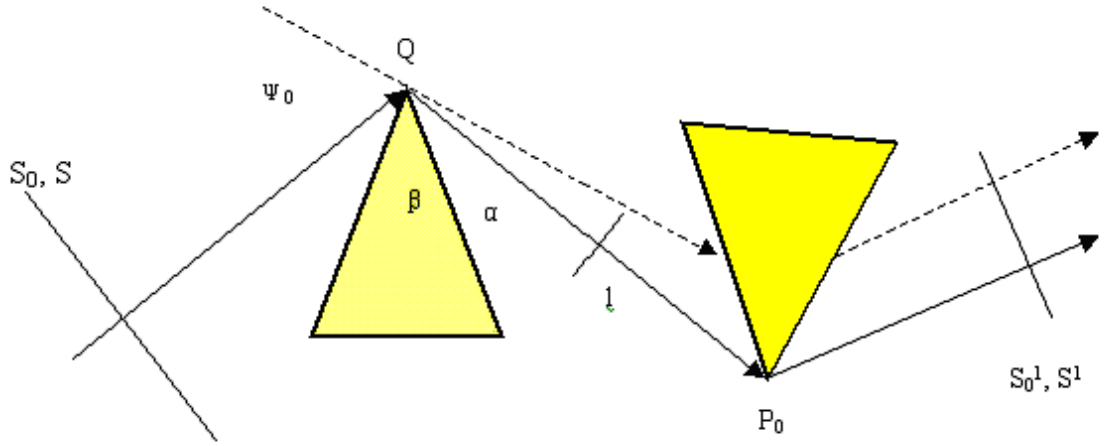

Figure 2.4: Group velocity dispersion introduced without net angular dispersion by a two prism sequence.

The effect of the first prism is a disperser producing group velocity dispersion as discussed in the above section, while the second prism produces a parallel output ray. The second prism's apex is assumed to be located at the reference point P_0 as in the Figure 2.3, so that the equation for the group velocity dispersion can be applied for the group dispersion. In order to deduce $d\alpha/d\Omega$, we use the identity

$$\frac{d\alpha}{d\Omega} = \frac{d\alpha}{dn}\frac{dn}{d\Omega} \qquad (2.2)$$

Where n is the refractive index of the prism material and

$$\frac{dn}{d\Omega} = -\frac{\lambda^2}{2\pi c}\frac{dn}{d\lambda}$$

is the material dispersion. The quantity $d\alpha/dn$ may be determined from the actual geometry, i.e., apex angle β and incidence angle ψ_0. In the case of a symmetrical beam path through the prism for the component ω_1 (it means minimum deviation) and an apex angle being chosen so that the Brewster condition is satisfied (this means minimum reflection losses) [13], we have

$$\frac{d\alpha}{dn} = -2 \qquad \frac{d^2\alpha}{dn^2} = \frac{2}{n^3} - 4n \qquad (2.3)$$

Inserting equations (2.2) and (2.3) into equation (2.1), we can get

$$\left.\frac{d^2\Psi}{d\Omega^2}\right|_{\omega l} \approx -4\frac{\omega_l}{c} l\left(\left.\frac{dn}{d\Omega}\right|_{\omega l}\right)^2$$

Expressed in terms of wavelengths as

$$\Psi''(\omega_l) = \left.\frac{d^2\Psi}{d\Omega^2}\right|_{\omega l} \approx -4l\frac{\lambda_l^3}{2\pi c^2}\left(\left.\frac{dn}{d\lambda}\right|_{\lambda l}\right)^2$$

For the third order dispersion term we obtain

$$\begin{aligned}\Psi'''(\omega_l) &= \left.\frac{d^3\Psi}{d\Omega^3}\right|_{\omega l} \\ &\approx \left.\frac{12l\lambda_l^4}{(2\pi)^2 c^3}\left\{(\frac{dn}{d\lambda})^2\left[1-\lambda_l\frac{dn}{d\lambda}(n^{-3}-2n)\right]+\lambda_l(\frac{dn}{d\lambda}\frac{d^2n}{d\lambda^2})\right\}\right|_{\lambda l}\end{aligned} \tag{2.4}$$

In deriving equation (2.4), the terms that are usually of much smaller magnitude than those considered above were neglected. In order to decide whether this prism sequence can be used to simply introduce the group velocity dispersion, we calculate the ratio of the third and second order phase terms in the Taylor expansion of the phase response:

$$\begin{aligned}R_P &= \left|\frac{b_3(\Omega-\omega_l)^3}{b_2(\Omega-\omega_l)^2}\right| \\ &= \left|\frac{\Psi'''(\omega_l)}{3\Psi''(\omega_l)}\right|\left|\Omega-\omega_l\right| \\ &\approx \left[1-\lambda_l\left.\frac{dn}{d\lambda}\right|_{\lambda l}(\frac{1}{n^3}-2n)+\lambda_l\frac{\left.\frac{d^2n}{d\lambda^2}\right|_{\lambda l}}{\left.\frac{dn}{d\lambda}\right|_{\lambda l}}\right]\frac{\Delta\lambda_l}{\lambda_l}\end{aligned}$$

here, $\left|\Omega-\omega_l\right|$ has been approximated by the spectral width of the pulse $\Delta\omega_l$, and we have used the identity $\left|\Delta\omega_l\right| = (2\pi c)\left|\Delta\lambda_l\right|/(\lambda_l^2)$. It is obvious to say, both the pulse characteristics (relative spectral width $\Delta\lambda_l / \lambda_l$) and the material parameters determine to what extent the prism

sequence can be regarded as a group velocity dispersion element. As an example, one finds $R_P \approx$ 0.1 for 20 femtosecond pulses at 620 nm for fused silica. Normally, the influence of higher order dispersion is more critical in dispersive devices in the laser resonator than in extra cavity application.

The prism introduces group velocity dispersion through angular dispersion was discussed only so far. In practice, however, the beam also passes through a certain amount of glass in each prism that causes the dispersion. Suppose L to be the cumulative mean glass path; then the additional second order dispersion parameter is

$$\Psi_L''(\omega_l) = \frac{d^2}{d\Omega^2}\left(\frac{\Omega}{c} nL\right)\Big|_{\omega l}$$

Expressed as a function of wavelength:

$$\Psi_L''(\omega_l) = \frac{\lambda_l^3}{2\pi c^2} L \frac{d^2 n}{d\lambda^2}\Big|_{\lambda l}$$

The third order dispersion term for glass is:

$$\Psi'''_L(\omega_l) = \frac{d^3}{d\Omega^3}\left(\frac{\Omega}{c} nL\right) = \left(3\frac{d^2 n}{d\Omega^2} + \Omega \frac{d^3 n}{d\Omega^3}\right)\frac{L}{c}$$

Expressed as a function of wavelength:

$$\Psi'''_L(\omega_l) = -\frac{\lambda_l^2}{(2\pi)^2 c^3}\left[3\lambda_l^2 \frac{d^2 n}{d\lambda^2} + \lambda_l^3 \frac{d^3 n}{d\lambda^3}\right] L$$

So that the total dispersion of the prism sequence is:

$$\Psi''_{tot}(\omega_l) \approx \frac{\lambda_l^3}{2\pi c^2}\left[Ln'' - 4n'^2 l\right] \qquad (2.5)$$

and

$$\Psi'''_{tot}(\omega_l) \approx \frac{\lambda_l^4}{(2\pi c)^2 c}\left[12l(n'^2\left[1 - \lambda_l n'(n^{-3} - 2n\right] + \lambda_l n' n'') - L(3n'' + \lambda_l n''')\right] \qquad (2.6)$$

To simplify the notation, we have introduced n', n'' and n''' for the derivatives of n with

respect to λ taken at λ_1. Since the angular dispersion always results in negative group velocity dispersion, positive group velocity dispersion is in the visible and near infrared spectral range where $d^2n/d\lambda^2>0$ is given by the finite glass path. This sign difference in the types of group velocity dispersion offers the possibility of tuning the group velocity dispersion by changing the cumulative mean glass path. Simply translating one of the prisms perpendicularly to its base is a convenient method, which alters the glass path while keeping the beam deflection constant. It will generally be desirable to avoid a transverse displacement of spectral components at the output of the dispersive device.

In this section we have derived approximate expressions for dispersion terms of second and third order. It is also possible by methods of pulse tracing through the prisms to determine the exact phase factor at any frequency and angle of incidence [9]; [14]; [15]; [16]; [17]. The more complex studies revealed that the group velocity dispersion and the ratio R depend on the angle of incidence and apex angle of the prism. In addition, any deviations from the Brewster condition increase the reflection losses. The optimization of the prism separation l, the glass pathlength L, and the material for the prism are particularly for the generation of sub 20 femtosecond pulses in lasers [18]; [19].

2.1.1.5 Group velocity dispersion introduced by grating

Compared with prisms gratings can produce larger dispersion. The resulting negative group velocity dispersion was first introduced by Treacy to compress pulses of a Nd:glass laser [20]. In total analogy with prisms, the simplest practical solution consists of two identical gratings arranged as in Fig. 2.5 for zero net angular dispersion. Through tracing the frequency dependent ray path we can determine the dispersion introduced by a pair of parallel gratings. The optical pathlength P_{OL} between point A and an output wavefront $\overline{PP_0}$ is frequency dependent and can

be determined with help of Figure 2.5 to be:

$$P_{OL}(\Omega) = \overline{ACP} = \frac{b}{\cos(\beta' + \alpha)}\left[1 + \cos(\beta' + \beta + \alpha\right] \qquad (2.7)$$

where β is the angle of incidence, $\beta' + \alpha$ is the diffraction angle for the frequency component Ω and b is the normal separation between G_1 and G_2.

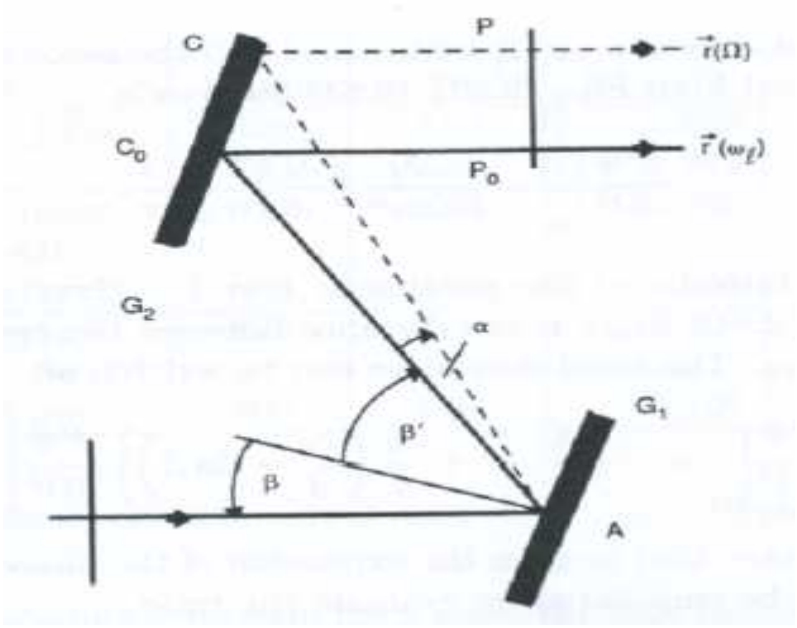

Figure 2.5: Group velocity dispersion introduced without net angular dispersion by two parallel gratings.

If we just consider the first-order diffraction, the incidence angle and the diffraction angle are related through the grating equations

$$\sin\beta - \sin\beta' = -\frac{2\pi c}{\omega_l d} \qquad (2.8)$$

and

$$\sin\beta - \sin(\beta' + \alpha) = -\frac{2\pi c}{\Omega d} \qquad (2.9)$$

Where d is the grating constant. Grating can introduce an additional phase shift of 2π at each

ruling of G_2 [10]. For this reason only the relative phase shift across $\overline{PP_0}$ matters. We may simply consider the rulings from the intersection of the normal in A with G_2. Thus, we find for $\Psi(\Omega)$:

$$\Psi(\Omega) = \frac{\Omega}{c} P_{OL}(\Omega) + 2\pi \frac{b}{d} \tan(\alpha + \beta') \qquad (2.10)$$

Because $\alpha = \alpha(\Omega)$ with $\alpha(\omega_l) = 0$, the second derivative of Ψ can be obtained from equations (2.7) to (2.10) and reads

$$\left.\frac{d^2\Psi}{d\Omega^2}\right|_{\omega_l} = -\frac{\lambda_l}{2\pi c^2}\left(\frac{\lambda_l}{d}\right)^2 \frac{b}{\sqrt{r}} \frac{1}{r} \qquad (2.11)$$

where we have introduced the parameter $r = 1-[2\pi c/(\omega_l d) - \sin\beta]^2 = \cos^2\beta'$.

In equation (2.11), $b/\sqrt{r}$ is the distance between the two gratings along the ray at frequency $\Omega = \omega_l$. The third derivative is

$$\left.\frac{d^3\Psi}{d\Omega^3}\right|_{\omega_l} = -\frac{3\lambda_l}{2\pi c r}\left[r + \frac{\lambda_l}{d}\left(\frac{\lambda_l}{d} - \sin\beta\right)\right]\left.\frac{d^2\Psi}{d\Omega^2}\right|_{\omega_l} \qquad (2.12)$$

To decide when the third term in the expansion of the phase response of the grating needs to be considered we consider the ratio

$$R_G = \left|\frac{b_3(\Omega-\omega_l)^3}{b_2(\Omega-\omega_l)^2}\right| = \left|\frac{\Psi'''(\omega_l)}{3\Psi''(\omega_l)}\right||\Omega-\omega_l| \approx \frac{\Delta\omega_l}{\omega_l}\left[1 + \frac{\lambda_l/d(\lambda_l/d - \sin\beta)}{1-(\lambda_l/d-\sin\beta)^2}\right]$$

It is possible to minimize the ratio of second and third order dispersion by changing the grating constant and the incidence angle. For example, with $\Delta\omega_l/\omega_l = 0.05$, $\lambda_l/d = 0.5$ and $\beta = 0$ degree we have $R_G \approx 0.07$.

In practice, gratings rather than prisms are used for the shaping of high power laser pulses. The reason for this is to avoid undesired nonlinear optical effects in the glass material of prisms. The shortcoming of gratings is the total transmission through a grating pair is considerably smaller as compared to a pair of prisms. Usually this value does not exceed 80 %. Therefore, and because of the easy tenability, prism sequences are used intracavity.

The spectral components at the output of the second grating have transverse displacement. This transverse displacement can be compensated by using two pairs of gratings in sequence or by sending the beam once more through the first grating pair. As a result, the overall dispersion then doubles. Tenability is achieved by changing the grating separation b. The group velocity dispersion introduced by grating is always negative.

2.1.1.6 Group velocity dispersion introduced by Gires-Tournois interferometer

The Michelson interferometer can be used to determine the dispersion of a mirror. A symmetric interference pattern can only be achieved in a well compensated Michelson interferometer with identical mirrors in both arms, which are broadband. A Michelson interferometer can be a tool to split a pulse and to generate a certain delay between the two partial pulses.

The Gires-Tournois interferometer is one type of interferometer that can be used for pulse shaping. Its striking feature is a very high and almost constant amplitude transmission accompanied by the ability to tune the spectral phase continuously. For this reason, it can be used to control the group velocity dispersion in a femtosecond laser in a similar manner as prisms and gratings. The structure of a Gires-Tournois is shown in the Figure 2.6

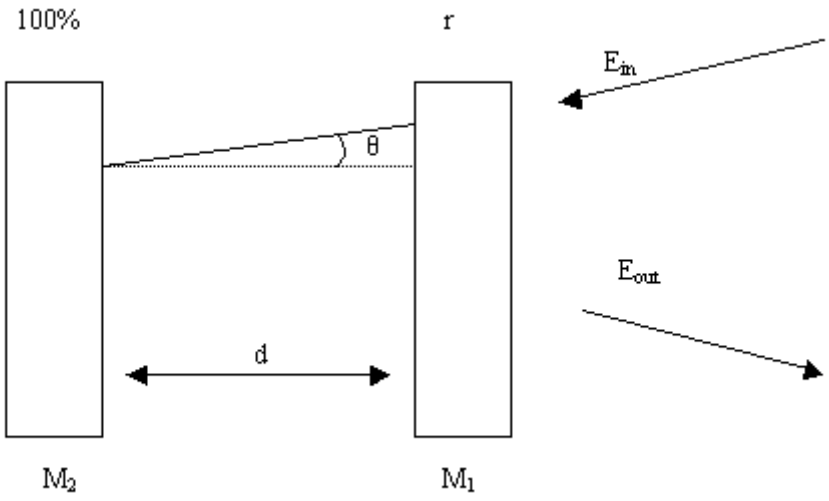

Figure 2.6: Schematic diagram of a Gires-Tournois interferometer.

A Gires-Tournois interferometer has one mirror with a reflection coefficient of 1. This is mirror M_2 in Figure 2.6. Consequently it is used in reflection. In this case the transfer function is given by

$$R(\Omega)e^{-i\Psi(\Omega)} = \frac{-r + e^{i\delta}}{1 - re^{i\delta}} \qquad (2.13)$$

where δ is the phase delay between two successive partial waves that leave the interferometer and r is the amplitude reflection of M_1. There is no change in the pulse energy because the reflectivity of the device is |R| =1. From equation (2.13) we know the phase response is

$$\Psi(\Omega) = -\arctan\left[\frac{(r^2-1)\sin\delta}{2r-(r^2+1)\cos\delta}\right]$$

Which gives for the quantity responsible for group velocity dispersion

$$\frac{d^2}{d\Omega^2}\Psi(\Omega)\bigg|_{w_l} = \frac{2r(r^2-1)\sin\delta}{(1+r-2r\cos\delta)^2}\left(\frac{d\delta}{d\Omega}\bigg|_{w_l}\right)^2$$

It is obvious that the group velocity dispersion can be turned continuously by adjusting δ which

can be either through a change of the mirror separation or through a change of the incidence angle. Gires and Tournois [21] introduced this device to adapt the pulse compression technique used in radar to optical frequencies. Duguay and Hansen applied it to pulse compression for lasers for the first time [22]. If the pulse durations are on the order of several hundred picosecond then the mirror spacing needs to be on the order of a few millimeters. If the pulse durations are on the order of several hundred femtoseconds then the mirror spacing needs to be on the order of few microns. It is nearly impossible for real implementation. Heppner and Kuhl [23] resolved this obvious practical difficulty by designing a Gires-Tournois interferometer on the basis of dielectric multiplayer systems. The structure is shown in Figure 2.7. The 100% mirror M_2 is a sequence of dielectric coating with alternating refractive index deposited on a substrate. A certain spacer of optical thickness d consisting of a series of $\lambda/2$ layers of one and the same material is placed on top of M_2. The partially reflective surface M_1 is realized by one $\lambda/4$ layer of high refractive index. Through changing the incidence angle and the number of passes through the interferometer, the dispersion of this compact device can be tuned. Figure 2.7 shows a possible arrangement which was successfully applied for group velocity dispersion adjustments in femtosecond lasers [24].

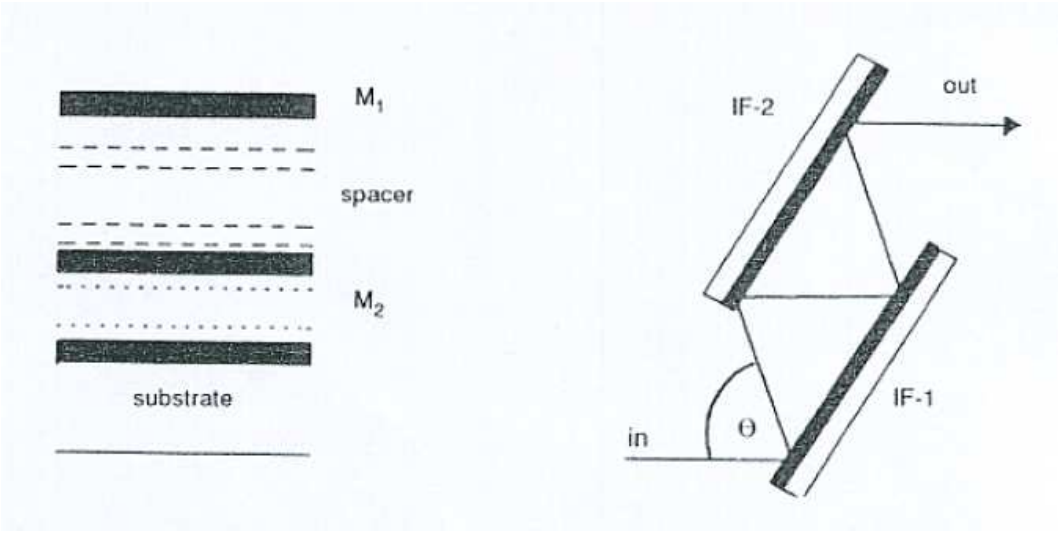

Figure 2.7: A Gires-Tournois interferometer for femtosecond laser pulses using dielectric multiayers.

2.1.1.7 Dispersion Compensation in ultra fast laser cavity

Dispersion compensation is one basic aspect for ultra fast laser systems. For getting the ultra fast pulse the dispersion compensation inside the laser cavity should be very well. Here are some simple and practical methods to discuss in this part.

2.1.1.8 One assumption of the dispersion in the laser cavity

A basic assumption that underlies many designs for chirped-pulse amplification of ultrashort pulse is that a Taylor´s series expansion of the dispersive dely of each optical component is well behaved. Here, the meaning of well behaved is that the effect of each term in the expansion produces a significantly smaller pulse broadening or distortion compared to the effect of the previous term. The phase Φ, accumulated by a pulse in a given optical element, can be expressed by a Taylor´s series expansion as

$$\phi(\omega) = \phi(\omega_0) + \left.\frac{\partial\phi}{\partial\omega}\right|_{\omega 0} (\omega - \omega_0) + \frac{1}{2!}\left.\frac{\partial^2\phi}{\partial\omega^2}\right|_{\omega 0} (\omega - \omega_0)^2 + \frac{1}{3!}\left.\frac{\partial^3\phi}{\partial\omega^3}\right|_{w0} (\omega - \omega_0)^3 + O(\Delta\omega^4)$$

here, ω describes the angular frequency and ω_0 describes the center frequency of the expansion. While the first term of this expansion is a constant, and the second term expresses an overall time shift of the pulse, the other terms represent distortions to the shape of the pulse. The group delay dispersion or quadratic phase is the coefficient of the third term. The cubic phase is the coefficient of the fourth term, and so on. The dispersive delay is related to the accumulated phase by

$$\tau(\omega) = \frac{\partial\phi(\omega)}{\partial\omega}$$

So that the dispersive delay can be represented as [25]:

$$\tau(\omega) = \left.\frac{\partial\phi}{\partial\omega}\right|_{\omega 0} + \left.\frac{\partial^2\phi}{\partial\omega^2}\right|_{\omega 0}(\omega-\omega_0) + \frac{1}{2!}\left.\frac{\partial^3\phi}{\partial\omega^3}\right|_{\omega 0}(\omega-\omega_0)^2 + \frac{1}{3!}\left.\frac{\partial^4\phi}{\partial\omega^4}\right|_{\omega 0}(\omega-\omega_0)^3 \quad (2.7)$$
$$+ O(\Delta\omega^4)$$

This basic assumption is that a Taylor´s series expansion of the dispersive delay is well behaved in the sense that each phase order in the expansion produces an effect on the pulse that is significantly smaller than the effect of the previous order. That is,

$$\left.\frac{\partial^2\phi}{\partial\omega^2}\right|_{\omega 0}(\omega-\omega_0) >> \frac{1}{2!}\left.\frac{\partial^3\phi}{\partial\omega^3}\right|_{\omega 0}(\omega-\omega_0)^2 >> \frac{1}{3!}\left.\frac{\partial^4\phi}{\partial\omega^4}\right|_{\omega 0}(\omega-\omega_0)^3 \cdots$$

Over the bandwidth of the pulse.

This assumption depends strongly on the duration and bandwitdh of the pulse. For example, if a spectrally limited Gaussian pulse centered at 795 nm has an initial full width at half maximum (FWHM) of 100 femtoseconds and propagates through 1 cm of fused silica, a material that easily satisfies the basic assumption, the intensity profile is essentially unchanged. But if the same pulse with FWHM of 10 femtoseconds passes the same fused silica, the intensity profile broadens to over 100 femtosecond FWHM.

2.1.1.9 Group velocity dispersion introduced by prims

In most cases, one likes to control the group velocity dispersion, and at the same time avoid the beam divergence introduced by angular dispersion. The simplest practicable solution to this problem is two identical prisms sequence that is adjusted for the angular dispersion to be compensated. The total dispersion of the prim sequence is [26]:

$$\phi''_{tot}(\omega_l) \approx \frac{\lambda_l^3}{2\pi c^2}\left[Ln'' - 4n'^2 l\right]$$

Here, n' and n'' is the derivatives of n with respect to λ taken at λ_l. While the angular dispersion always results in negative group velocity dispersion, the finite glass path gives rise to

positive GVD in the visible and near infrared spectral range. This sign difference in the types of group velocity dispersion offers the possibility of tuning the GVD by changing L and l.

2.1.1.10 Group velocity dispersion introduced by gratings

To produce larger angular dispersion than prisms and in order to avoid undesired nonlinear optical effects in the galss material, the gratings are normally used outside of the laser cavity. The group velocity dispersion introduced by a gratings pair is:

$$\left.\frac{d^2\Psi}{d\Omega^2}\right|_{\omega_l} = -\frac{\lambda_l}{2\pi c^2}\left(\frac{\lambda_l}{d}\right)^2 \frac{b}{\sqrt{r}}\frac{1}{r}$$

where the parameter r = $\cos^2 \beta^1$ and b/$\sqrt{r}$ is the distance between the two gratings along the ray at $\Omega = \omega_1$.

2.1.1.11 Group velocity dispersion introduced by GTI mirrors

The Gires-Tournois interferometer is one type of interferometer that can be used for pulse shaping. Its striking feature is a very high and almost constant amplitude transmission accompianed by the ability to tune the spectral phase continuously. For this reason, it can be used to control the group velocity dispersion in a femtosecond laser in a similar manner as prisms and gratings. The group velocity dispersion introduced by the GTI mirrors is:

$$\left.\frac{d^2}{d\Omega^2}\Psi(\Omega)\right|_{w_l} = \frac{2r(r^2-1)\sin\delta}{(1+r-2r\cos\delta)^2}\left(\left.\frac{d\delta}{d\Omega}\right|_{w_l}\right)^2$$

where δ is the phase delay between two successive partial waves that leave the interferometer

and r is the amplitude reflection of the 100% reflection mirror.

2.1.2 Ultrashort sources

2.1.2.1 Mode locking

A broadband gain medium is required by a mode locked femtosecond laser, which will sustain over 100,000 longitudinal modes in a typical laser cavity. To term mode locking originates from the description of the laser in the frequency domain. The sum of the radiation of each of longitudinal modes makes up the emission. In a free running laser, the phases of a comb of equally spaced modes (frequency spacingΔ) can be a set of random numbers. The time domain transformation of such a frequency spectrum is an infinite series of identical bursts of incoherent light, spaced in time by $\tau_{RT}=2\pi/\Delta$, which is the time needed to complete a cavity round trip. Mode locking, which forces all the modes to have equal phase, implies in the time domain that all the waves of different frequency will add constructively at one point. The result is a very intense and short burst of light. An over whelming proportion of ultrashort sources is based on some mode locking mechanism.

2.1.2.2 Passive mode locking

In order to favour operation of pulsed over continuous radiation, some intensity dependent loss or dispersion mechanism is used in the case of passive mode locking. Active mode locking is another type of mechanism: a coupling is introduced between cavity modes, locking them in phase. In hybrid and doubly mode locked lasers, both mechanisms of mode locking mentioned

previously are used. In parallel to this categorization in active and passive lasers, one can also classify the lasers as being modulated inside (the most common approach) or outside (usually in a coupled cavity) the laser.

A gain medium and a positive feedback element are two essential components in the cavity of a passively mode locked laser. In the case of the latter, it has a device or material that has losses decreasing with intensity or energy. Because of the progressive decrease in attenuation, a positive feedback element has the effect of sharpening the leading edge of a pulse.

Gain saturation also has effect on the pulse evolution. A good example is a laser with a saturable absorber. In the time after the absorber has bleached, there is a net gain inside the cavity. In the time before absorber recovers (within a time t_s), there is also a net gain for any disturbance that follows the pulse in the cavity. It needs a time, which the saturation energy density has been reached in the gain medium: $W(t'_s)=W_{sg.}$ Let us define this time as t'_s. For best cavity conditions, saturation in the gain medium will be reached at a time $t'_s > t_s$. Because the laser pulse is being amplified, it will deplete the gain medium. The result is a net negative gain in the cavity, in which small disturbances will be damped. It is essential for the operation of a passively mode locked laser that the gain saturates at a higher energy than the characteristic energy of the positive feedback, to ensure a time window $t_s<t< t'_s$ during which pulse amplification can occur. In this time window, the losses are saturated, as the gain has not yet saturated. In this time window the pulse leading edge steepens. New gave a detailed analytical and numerical treatment of the pulse evolution because of saturable gain and absorption [27] [28].

2.1.2.3 Elements of a femtosecond laser

A femtosecond laser has a few basic elements:

A broadband gain medium

A laser cavity

An output coupler

A dispersive element

A phase modulator

A gain/loss process controlled by the pulse intensity or energy

The items listed above refer more to function than to physical elements. For example, the gain rod in a Nd:glass laser can cumulate the functions of gain, phase modulator, loss modulation, and gain modulation. To generate femtosecond pulses, there is most often a dispersive mechanism of pulse compression present, with phase modulation to broaden the pulse bandwidth, and dispersion to eliminate the chirp and compress the pulse.

2.1.2.4 Pulse formation

Any free running oscillator generates a signal originating from noise. The radiation from a femtosecond laser is no different. In continuously pumped lasers, spontaneous emission from the active medium will introduce the noise. After the first mode locked laser was achieved, numerous theories and computer simulations were introduced to explain the evolution from noise to a regular train of pulses [[29]]. One basic requirement for this transition from noise to pulsed operation to occur is that the pump power has to exceed a given threshold P_{th}. Sometimes this threshold is higher than the power required to sustain mode locking. For this reason a mode locked laser will not always restart if its operation has been interrupted.

The first step of a complex pulse evolution is emergence of a pulse from noise. Such a pulse may contain sub femtosecond noise pulses and be as long as a fraction of the cavity round trip time. Subsequently, this pulse will be submitted to several compression mechanisms that will bring it successively to the picosecond and femtosecond range. First, a loss (saturable absorption) and gain (synchronous pumping, gain saturation) mechanism will steepen the leading and trailing

edges of the pulse, reducing its duration down to a few picoseconds. Then the next coming effect is dispersive mechanisms, such as self phase modulation and compression, which take over from the picosecond to femtosecond range. On another side, there are mechanisms of pulse broadening that prevent pulse compression from proceeding indefinitely in the cavity. The bandwidth limitation of the cavity is the most obvious and simple broadening effect. This occurs in some lasers like glass lasers and Nd:YAG lasers. Higher order dispersion of optical components and nonlinear effects introduce other pulse width limitations.

When the pulse reproduces itself after an integer number of cavity round trips, then a “steady state” is reached. In such a situation, such pulse parameters as gain and loss, compression and broadening mechanisms, as well as shaping effects, balance each other.

2.1.2.5 Pulse compression mechanisms

A qualitative overview of the various processes that can contribute to pulse shortening is described here. A femtosecond laser requires a strong compression mechanism, but may not be sufficient to achieve stable operation. In the following a subscript “a” is used for the physical parameters relating to an absorber, and a subscript “g” is used for the parameters relating to the gain medium.

2.1.2.6 Gain saturation

Only the case of small gain factors is considered here. Before the saturation energy of the gain medium is reached, the leading edge of the pulse is amplified. In some conditions, fractional reduction in pulse occurring, the width of the pulse is reduced.

2.1.2.7 Absorber saturation

Consider a cavity with saturable losses. As the pulse circulates in such a cavity, linear absorption erodes its leading edge. If the energy relaxation time T_{1a} of the absorber is shorter than the pulse duration τ_p, a part of the leading edge up to the saturation intensity I_{sa} is clipped. Once the intracavity pulse has been compressed down to a range where $\tau_p << T_{1a}$, at the time t_s the absorption saturates. At the same time the saturation energy density W_{sa} has been reached. A maximum compression can be achieved if an optimum ratio of pulse energy density to saturation energy is satisfied.

2.1.2.8 Phase modulation and dispersion

Absorption and saturation (a resonant effect), and a non-resonant intensity dependent index of refraction are the most important self phase modulation mechanisms in a femtosecond laser. Another name for the latter effect is the Kerr effect. Rigorously speaking, the optical Kerr effect is the birefringence induced by an optical field. A material with a large Kerr effect has a large intensity dependent index of refraction, which is the primary effect of interest here.

The saturation effect will uniformly reduce the whole absorption line in a homogeneously broadened absorber. The amplitude of dispersion line associated with the resonance is correspondingly reduced as a consequence of Kramers-Kronig relations. The saturable absorber of most femtosecond dye lasers has its peak absorption at a shorter wavelength than the laser wavelength. Therefore, the index of refraction will generally decrease with increasing saturation. There will be a sweep of index of refraction during the pulse, resulting in a phase modulation.

The phase modulation can be either downchirp or upchirp. In the condition of satutable absorbers at relatively low intensity downchirp occurs. Generally Kerr effect induces Upchirp. Upchrip is

proportional to minus the time derivative of the pulse intensity. This chirp is dominant in solid state lasers (for instance, in the Ti:sapphire laser) or in femtosecond dye lasers where the intensity is sufficiently high for the Kerr effect of the solvent to dominate. Prism arrangemet with large negative dispersion is generally used for intracacity pulse compression for such upchrip.

2.1.2.9 Self lensing effects

Self phase modulation is intensity dependent. The result is to be a function of the transverse coordinate. A self-induced negative lens associates with the downchirp or upchirp, in other words, self-defocusing. Either increasing the overlap between the cavity mode and the pump pulse or increasing the transmission through an aperture can modulate the gain with this effect. In some lasers, the self-defocusing is used in conjunction with an aperture to truncate the pulse tail.

Nearly all ultrshort pulse mode locked lasers have self-lensing effect. As a result of self-lensing, the size of the cavity modes is modified, leading to an increase or reduction of losses because

1, there is a change in transmission through an aperture

2, there is a change in spatial overlap between the cavity mode and the pump beam.

In general the nonlinear interaction leads to a phase shift which, to a first approximation, can be assumed to be quadratic in the radial coordinate $\Delta\psi(r) \approx Br^2$. The radial phase variation of a spherical wave of curvature R is $\psi(r) = -k_l r^2 / 2R$. Given a quadratic radial phase variation $B(t)r^2$, the beam will focus in a distance f_{nl} given by

$$f_{nl} = \frac{k_l}{2B(t)} \qquad (2.7)$$

2.1.2.10 Kerr lensing

The Kerr effect is a change in the refractive index of a material in response to the intensity of an external electric field.

The optical Kerr effect is the special case in which the external electric field is from light itself, such as that from a laser. The electric field produces a slowly varying refractive index, which then acts on the light. This intensity-dependent refractive index is responsible for effects like self-focusing and self-phase modulation, and is the basis for Kerr lens mode locking.

Kerr-lens mode locking is a method of mode locking lasers via a nonlinear optical process known as the optical Kerr effect. This method allows the generation of pulses of light with duration as short as a few femtoseconds.

Because of the non-uniform power density distribution in a Gaussian beam (as found in laser resonators) the refractive index changes across the beam profile; the refractive index experienced by the beam is greater in the center of the beam than at the edge. Therefore a rod of an active Kerr medium works like a lens for high intensity light. In the laser cavity short bursts of light will then be focused differently to continuous waves (cw). By aligning the cavity in a way such that the resonator is more lossy for cw light than for pulses, the pulsed regime is favored and the laser will turn to pulsed operation (mode locked). The favoring of different regimes and pulse lengths can be achieved by the cavity design (stability of the cavity), but is often supported by an aperture, that simply cuts off (hard aperture) or attenuates (soft aperture) the cw beam at the focal region of the pulsed beam.

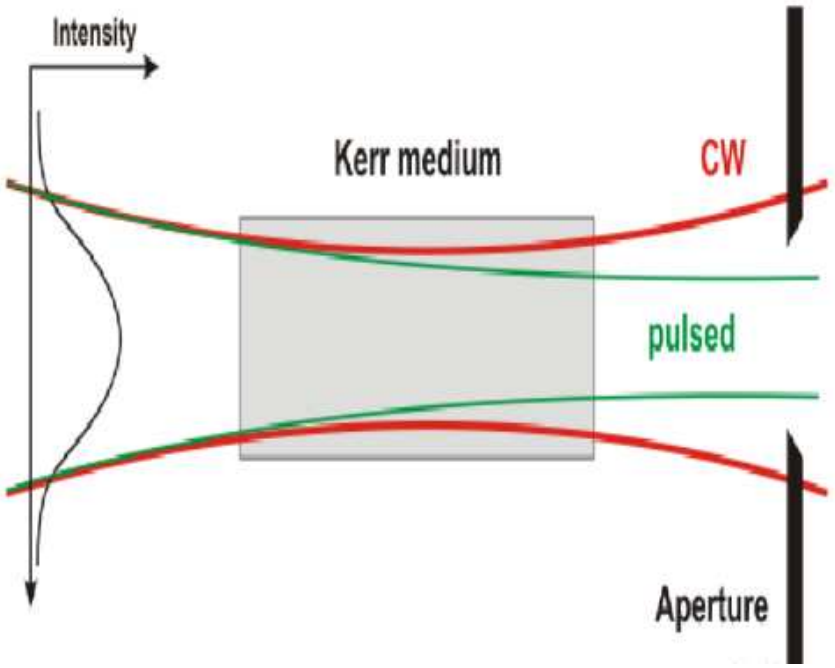

Figure 2.8: The principle of Kerr Lensing effect.

Let us consider a Kerr medium with a thickness of d. Let us suppose that d is small compared to either the Raleigh range ρ_0 or the induced focal length f_{nl}. A guassian beam is incident. The waist of this laser beam is ω_0. The nonlinear index introduces such a phase shift:

$$\Delta\psi(r,t) = -k_l d\,\frac{\bar{n}_2 I(r,t)}{n_0} \approx -k_l d\,\frac{\bar{n}_2 I(t)}{n_0}\left(1-\frac{2r^2}{\omega_0^2}\right) \qquad (2.8)$$

where I(t) = I (r = 0, t) is the intensity on axis. From equation (2.8) we get $B \approx 2\bar{n}_2 k_l I(t) d/(n_0 \omega_0^2)$. Substituting in equation (2.7), we find for the Kerr effect induced lensing:

$$f_{nl} = \frac{n_0 \pi \omega_0^4}{8\bar{n}_2 P d}$$

where $P = \pi \omega_0^2 I(t)/2$ is the power.

ABCD matrix can be used [30] to evaluate the intensity dependent losses introduced by Kerr lensing in a particular cavity [31]. The ABCD matrix of the resonator is calculated at such a position, which is starting from a reference plane at the position of the Kerr medium. For low intensity, for which the Kerr effect is negligible, $M_0 = \begin{pmatrix} A_0 & B_0 \\ C_0 & D_0 \end{pmatrix}$ is the ABCD matrix. At high intensity, this matrix is modified by the nonlinear lensing effect as follows:

$$M = \begin{pmatrix} 1 & 0 \\ -\frac{1}{f_{nl}} & 1 \end{pmatrix} \begin{pmatrix} A_0 & B_0 \\ C_0 & D_0 \end{pmatrix}$$

$$= \begin{pmatrix} A & B \\ C & D \end{pmatrix}$$

$$= M_0 + \begin{pmatrix} 0 & 0 \\ -\frac{A_0}{f_{nl}} & -\frac{B_0}{f_{nl}} \end{pmatrix}$$

Here f_{nl} is a quantity dependent on time. The complex beam parameter $\tilde{q}$ uniquely characterizes a Gaussian beam. The inverse complex radius of curvature of the beam, at the location of the Kerr medium, $\tilde{s} = 1/\tilde{q} = 1/R - i\lambda_l/(\pi\omega^2)$ is a solution (eigenmode) of the cavity round trip equation:

$$\tilde{s} = \tilde{s}_0 + \delta\tilde{s} = \frac{C + D\tilde{s}}{A + B\tilde{s}} \qquad (2.9)$$

where $\tilde{s}_0$ is the eigenmode if not considering the Kerr lensing. Multiplying both sides of equation (2.9) by the denominator then differentiating after this, and that the variation of the matrix elements A and B is null in the particular case of Kerr lensing. It will introduce:

$$\delta\tilde{s} = \frac{\delta C + \tilde{s}_0 \delta D}{A_0 + 2B_0\tilde{s} - D_0}$$
$$= \frac{1}{f_{nl}}\left[\frac{-(A_0 + B_0\tilde{s}_0)}{A_0 + 2B_0\tilde{s}_0 - D_0}\right]$$
$$= \frac{8\bar{n}_2 P\pi d\left|\mathrm{Im}(\tilde{s}_0)\right|^2}{n_0\lambda_l^2}\left[\frac{-(A_0 + B_0\tilde{s}_0)}{A_0 + 2B_0 s_0 - D_0}\right]$$

where the substitutions $\delta C = -A_0 / f_{nl}$, $\delta D = -B_0 / f_{nl}$, and $\omega_0^2 = \lambda_l / [\pi|\mathrm{Im}(\tilde{s}_0)|]$ have been made.

The meaning of the change in the complex beam parameter $\delta\tilde{s}$ is that the lensing effect results in a change in beam size at any location in the cavity. There is a positon where, ideally, the self-lensing results in the largest reduction in beam size. Typically, an aperture is used at such a particular location of the cavity. The ABCD matrix that connects the reference point of the cavity (location of the Kerr lens) to the position of the aperture is. $M_m = \begin{pmatrix} A_m & B_m \\ C_m & D_m \end{pmatrix}$. The complex beam parameter at the aperture is:

$$\tilde{s}_m = \frac{C_m + D_m\tilde{s}}{A_m + B_m\tilde{s}}$$

The relationship of the relative change in beam size at the aperture δ w_m/w_m and the change in inverse complex radius of curvature $\delta\tilde{s}_m$ is:

$$\frac{\delta w_m}{w_m} = -\frac{1}{2}\frac{\mathrm{Im}(\delta\tilde{s}_m)}{\mathrm{Im}(\tilde{s}_m)}$$

The change in beam parameter $\delta\tilde{s}$ at the point of reference can infer the change in beam parameter at the aperture $\delta\tilde{s}_m$:

$$\delta\tilde{s}_m = \frac{[(A_m + B_m\tilde{s}_0)D_m - (C_m + D_m\tilde{s}_0)B_m]}{(A_m + B_m\tilde{s}_0)^2}\delta\tilde{s}$$
$$= \left[\frac{-(A_0 + B_0\tilde{s}_0)}{(A_0 + 2B_0 s_0 - D_0)(A_m + B_m\tilde{s}_0)^2}\right]\frac{8\bar{n}_2 P\pi d\left|\mathrm{Im}(\tilde{s}_0)\right|^2}{n_0\lambda_l^2} \qquad (2.10)$$

All of the information necessary to estimate the effect of Kerr induced lensing on a cavity is contained in the equation (2.10). As a coarse estimate, an effective diameter w_a for the aperture could be defined, such that the transmission factor would be $P_2 / P_1 \approx (w_a / w_m)^2$, where P_2 and P_1 are the power of the pulse respectively after and before the aperture. It follows that:

$$\Delta P = P_2 - P_1$$
$$= -P_1(1 - \frac{w_a^2}{w_m^2})$$
$$= -P_1\left[1 - \frac{w_a^2}{w_{m0}^2}(1 - 2\frac{\delta w_m}{w_{m0}^2})\right] \qquad (2.11)$$
$$\approx \frac{aP_1}{1 + \frac{P_1}{P_S}}$$

where $a = 1 - (w_a / w_{m0})^2$ is the power loss coefficient at the aperture, w_{m0} is the beam size at zero power at the aperture ($w_m = w_{m0} + \delta w_m$), and

$$P_S = (\frac{w_a}{w_{m0}})^2 \mathrm{Im}(\tilde{s}_m)\left[1 - (\frac{w_a}{w_{m0}})^2\right]\frac{P}{\mathrm{Im}(\delta\tilde{s}_m)}$$

is the equivalent "saturation power" of the Kerr lens aperture combination which can be calculated by substituting expression (2.10) for δw_m. To the first order, the action of Kerr lensing combined with an aperture on the pulse power is similar to the action of a fast saturable absorber on the pulse intensity. The stronger absorption on the pulse leading and trailing edges than at the pulse peak results in the pulse compression.

2.1.2.11 Additive pulse mode locking

To subtract some energy from the pulse wings and transfer it to the pulse center is a simple method to compress a pulse. An implementation of this idea is additive pulse mode locking. In the situation of additive pulse mode locking, the output pulse is reinjected into the laser, with a phase modulation such that the pulse center and leading edge add in phase with the intracavity pulse, and the pulse tail out of phase. An auxiliary cavity is necessary other than the main cavity in order to “reinject” a fraction of the output pulse.

2.2 Three ultra fast laser systems

Diode pumped all-solid-state ultra fast lasers are promising for mini-invasive refractive surgery and keratoplasty. A fundamental systematical study concerning ultra fast laser tissue interactions is crucial before applying the state of the art laser technology to ophthalmic applications. Three diode pumped all-solid-state ultra fast lasers, namely, a Nd:glass femtosecond laser, a Yb:KYW femtosecond laser, and a Nd:YAG picosecond laser are involved in this research. The pulse width of the ultra fast laser ranges from 800 femtoseconds to 20 picoseconds.

2.2.1 Nd:glass femtosecond laser

Refractive surgery in the pursuit of perfect vision (e.g. 20/10) requires firstly an exact measurement of aberrations induced by the eye [[32]], and then a sophisticated surgical approach. A recent extension of wavefront measurement techniques and adaptive optics to ophthalmology has quantitatively characterized the quality of the human eye. The next milestone towards perfect

vision is developing a more efficient and precise laser scalpel and evaluating minimal-invasive laser surgery strategies. Femtosecond all-solid-state MOPA lasers based on passive mode locking and chirped pulse amplification are excellent candidates for eye surgery due to their stability, ultra-high intensity, and compact tabletop size. Furthermore, taking into account the peak emission in the near IR and diffraction limited focusing abilities, surgical laser systems performing precise intrastromal incisions for corneal flap resection and intrastromal corneal reshaping promise significant improvement over today's Photorefractive Keratectomy (PRK) and Laser Assisted In Situ Keratomileusis (LASIK) techniques which utilize UV excimer lasers. Through dispersion control and optimized regenerative amplification, a compact femtosecond all-solid-state laser with pulsed energy well above the LIOB threshold and a kHz repetition rate is constructed [[33]].

For self-starting, reliable femtosecond pulse generation, a semiconductor saturable absorber mirror (SESAM) produces sub 200 femtosecond pulses with a megahertz repetition rate. The pulse energy available from passively mode locked oscillators is at present limited to values around 1 nJ by the available pump power (several Watts) and high repetition rate (typically 100 MHz, in our case 76 MHz). The output pulses from this oscillator laser have to be temporally stretched in order to avoid distortion or damage to optical components in the following amplification stage. [[34]] Here, we take direct advantage of the broad spectrum associated with ultrashort pulses. Stretching is achieved by beam dispersion and subsequent time domain redistribution (chirp) of its spectral components. The stretched pulses are then coupled into the amplifier laser with an electro-optic crystal (Pockel`s cell). To provide the necessary pulse energy required by practical applications of short-pulse laser systems, a successful design approach modularizes the laser system units dedicated to pulse generation and amplification. Such a system is commonly termed *master oscillator-power-amplifier* (MOPA). The idea is to use a small, well controllable oscillator laser to generate a train of low-energy ultrashort pulses and to amplify the pulses to useful energy levels by a separate amplification stage. For ultrashort pulse amplification

the following properties are important: sufficient bandwidth, high gain, low noise, and good beam quality. An amplification scheme that provides efficient energy extraction from the amplifier laser medium, excellent amplitude stability and a nearly diffraction limited output beam, is the concept of *regenerative chirped pulse amplification*. Inside the regenerative amplifier, the pulse is circulated through the active laser material and gains energy upon each pass. This buildup process saturates to the maximum pulse energy after approximately 100 round-trips. At this point, all the extractable energy has been transferred to the pulse and inevitable cavity losses then begin to reduce the pulse energy. After reaching the buildup maximum, the pulse is therefore ejected from the amplifier. The amplified pulses are recompressed in a grating compression stage to 800 femtoseconds. Due to the limited amplification bandwidth of the laser active material (gain narrowing) and uncompensated higher order dispersion, the original pulse duration cannot be fully recovered in a simple grating compressor.

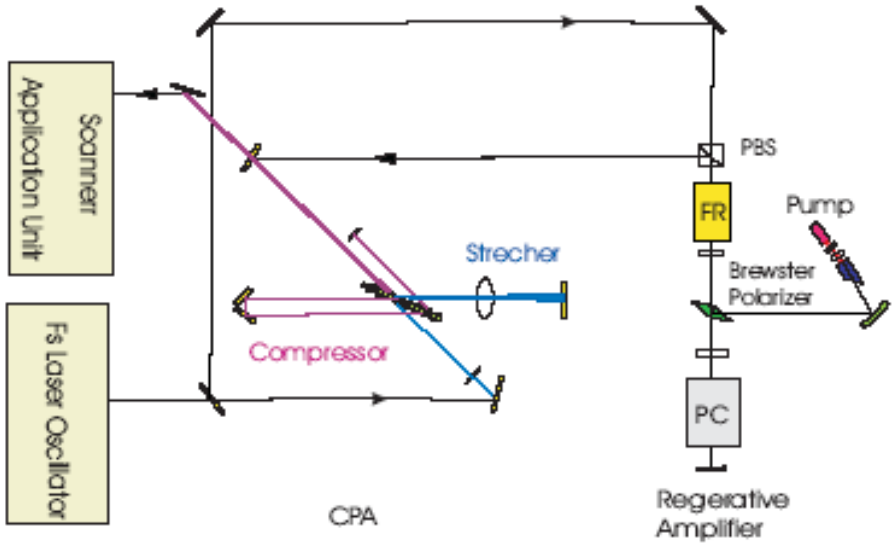

Figure 2.9: Schematic drawing of the diode pumped Nd:glass fs surgical laser system. The seed pulse from the Nd:glass fs pulse oscillator is amplified by a Chirped-Pulse-Amplification unit. The pulse is stretched and compressed by a single holographic transmission grating. FR: Faraday Rotator, PBS: Polarized Beam Splitter, λ/4: Quarter waveplate.

2.2.2 Yb:KYW femtosecond laser

Usually chirped pulse amplification (CPA) technology is applied to amplify ultra shorts pulses [[35]]. A disadvantage of this technology is its relative complexity and the requirement for very precise alignment of the stretcher and compressor. The thin disk regenerative amplifier concept uses a large cross sectional area to avoid high peak intensities and thus eliminates the need for CPA. One such laser system is involved in my research. It is a thin disk Yb:KYW femtosecond laser system [[36]]. This system consists of an oscillator, a telescope, a beam separation unit, and an amplifier.

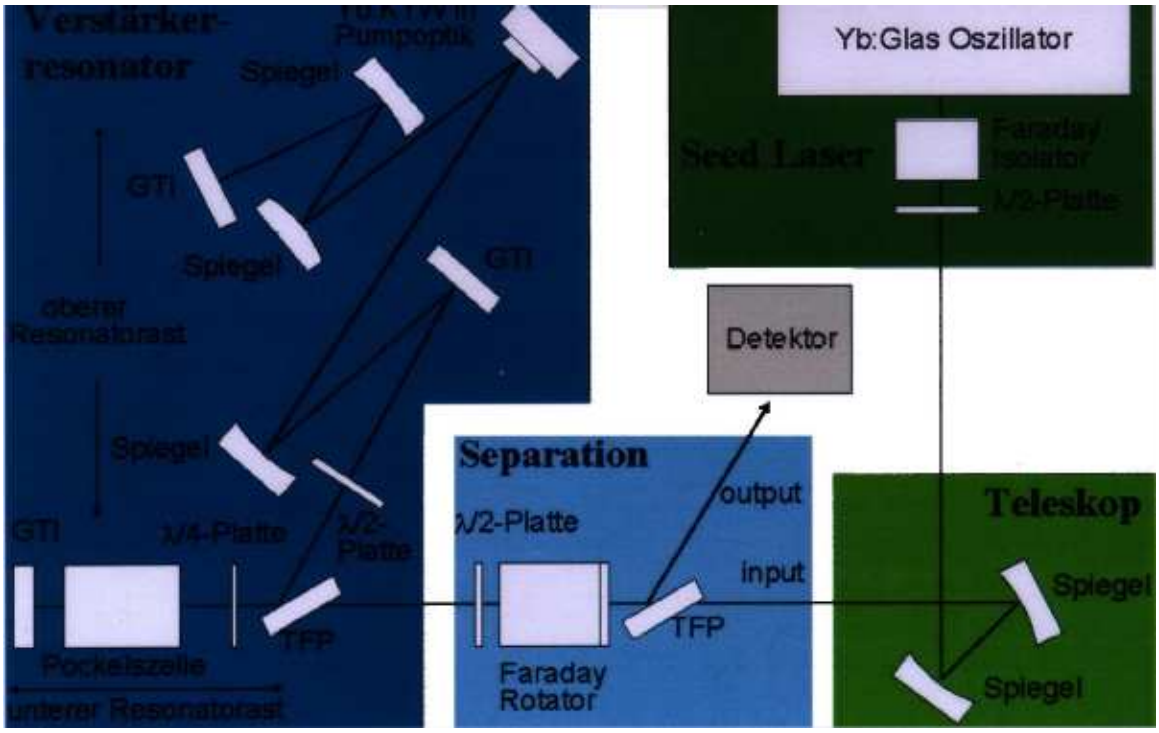

Figure 2.10: Schematic drawing of the diode pumped Yb:KYW femtosecond laser system. A thin disk amplification unit amplifies the seed pulse from the oscillator.

2.2.3 Nd:YAG picosecond laser

The Nd:YAG picosecond all-solid-state laser has a simpler structure compared with the other two laser systems. Neither pulse stretching nor dispersion contra is required. One may get a 20 picoseconds pulse with 200 μm maximum pulse energy.

Chapter 3 Ultra fast laser tissue interaction

3.1 Human eye and the structure of the cornea

3.1.1 Anatomy of human eye

The human eye is the organ, which gives us the sense of sight, allowing us to learn more about the surrounding world than any of the other five senses. We use our eyes in almost everything we do, whether reading, working, watching television, writing a letter, driving a car, or countless other activities. Sight is the most precious of the five senses, and many people fear blindness more than any other disability.

The eye allows us to see and interpret the shapes, colors, and dimensions of objects in the world by processing the light they reflected or given off. The eye is able to see in dim light or bright light, but it cannot see objects when light is absent. The eye changes light rays into electrical signals then sends them to the brain, which interprets these electrical signals as visual images.

The eye is set in a protective cone-shaped cavity in the skull called the orbit or socket and measures approximately one inch in diameter. The orbit is surrounded by layers of soft, fatty tissue, which protect the eye and enable it to turn easily.

Six muscles regulate the motion of the eye. Among the more important parts of the human eye are the iris, cornea, lens, retina, conjunctiva, the macula, and the optic nerve.

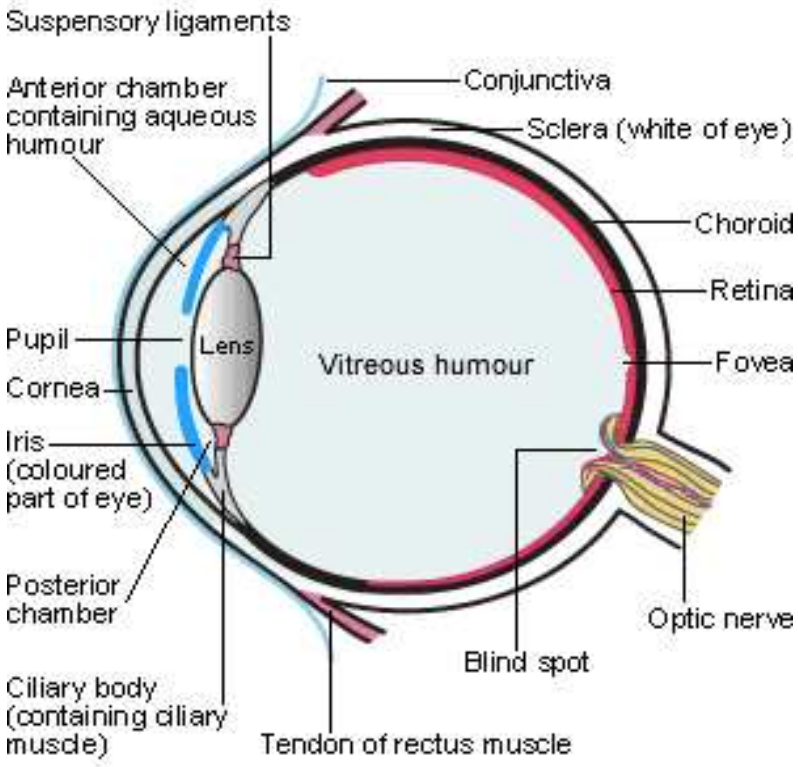

Figure 3.1: Anatomy of human eye

3.1.2 Structure of the cornea

We obtain more than 80% of our information from the external world by means of visual function. Good vision depends on the cornea and lens as refractive components. The cornea serves as the gateway into the eye for external images. Maintenance of corneal shape and transparency is critical for refraction. The cornea accounts for more than two-thirds of the total refractive power of the eye. A slight change in the corneal contour may thus result in refractive error. Small changes in the smoothness of the corneal surface or in the total thickness of the cornea also can lead to visual distortion. Recently, however, refractive surgery for the transparent cornea has been introduced. In this procedure, the curvature of the cornea is modified either by cutting the stroma

or by laser ablation of normal corneal tissue. Given the clinical efficacy of refractive surgery, it is important to understand the anatomic and physiological responses to surgical injuries of the cornea in addition to corneal pathology.

The cornea is a transparent avascular tissue that is exposed to the external environment. The anterior corneal surface is covered by the tear film, and the posterior surface is bathed directly by the aqueous humor. The transparent cornea is continuous with the opaque sclera and the semitransparent conjunctiva. The highly vascularized limbus, which contains a reservoir of pluripotential stem cells, constitutes the transition zone between the cornea and sclera. The shape of the anterior corneal surface is convex and aspheric. The anterior surface is transversely oval as a result of scleralization superiorly and inferiorly.

The adult human cornea measures 11 to 12 mm horizontally and 9 to 11 mm vertically. It is approximately 0.5 mm thick at the center, and its thickness increases gradually toward the periphery, where it is about 0.7 mm thick. The curvature of the corneal surface is not constant, being greatest at the center and smallest at the periphery. The radius of curvature is between 7.5 and 8.0 mm at the central 3mm optical zone of the cornea where the surface is almost spherical. The refractive power of the cornea is 40 to 44 diopters and constitutes about two-thirds of the total refractive power of the eye.

The optical properties of the cornea are determined by its transparency, surface smoothness, contour, and refractive index. Corneal transparency decreases when collagen fibers becomes heterogeneous (as occurs in fibrosis or edema); incident rays are scattered randomly and the cornea loses its transparency.

The corneal epithelium and tear film contribute to the maintenance of the arrangement of collagen fibers in the stroma. Both the mean diameter of each collagen fiber and the mean distance between collagen fibers are relatively homogeneous and are less than half of the wavelength of visible light (400 to 700 nm). This anatomic arrangement is thought to be responsible for the fact that scattering of an incident ray of light by each collagen fiber is

canceled by interference from other scattered rays, allowing light to pass through the cornea. In individuals with dry eye, the loss of normal lubrication and reduced supply of biologically active substances result in superficial punctate keratopathy, which is characterized by a rough corneal surface. Given that the spherocylindrical surface of the cornea has both a minor and a major axis, changes in corneal contour caused by pathological conditions, such as scarring, thinning, or keratoconus, or by refractive surgery, render the surface regularly or irregularly astigmatic.

Both the anterior and posterior surfaces of the cornea contribute to its optical function. The total refractive index of the cornea reflects the sum of refraction at these two interfaces as well as the transmission properties of the tissue. The refractive indices of air, tear fluid, corneal tissue, and aqueous humor are 1.000, 1.336, 1.376, and 1.336, respectively. The refractive power of a curved surface is determined by the refractive index and the radius of curvature. Refractive power at the central corneal is about ＋43 diopters, being the sum of that at the air-tear (＋44 diopters), tear-cornea (＋5 diopters), and cornea-aqueous humor (－6 diopters) interfaces. Most keratometry and topography measurements assume a standard refractive index of 1.3375.

The structure of the cornea is relatively simple compared with that of other parts of the body. Other avascular tissues of the body include the lens, vitreous body, and components of joints. The cell types that constitute the cornea include epithelial cells, keratocytes (corneal fibroblasts), and endothelial cells. Epithelial cells are derived from the epidermal ectoderm, whereas keratocytes and endothelial cells are of neural crest (neuroectodermal) origin. The precise arrangement of the various components of the cornea contributes to its transparency and strength. The cornea consists of three different cellular layers and two interfaces: the epithelium, bowman´s layer, the stroma, Descement´s membrance, and the endothelium. Components of the cornea interact with each other to maintain the integrity and function of the tissue.

The cornea is suffused by the tear film anteriorly and by the aqueous humor posteriorly. It contains almost all of the aqueous components of blood, including albumin and globulins, but few of the cellular components. This characteristic is important for understanding both the

regulatory mechanisms that underlie maintenance of normal corneal integrity and the pathobiology of various corneal diseases. Alterations in the components of tear fluid or the aqueous humor may result in pathological changes in the cornea.

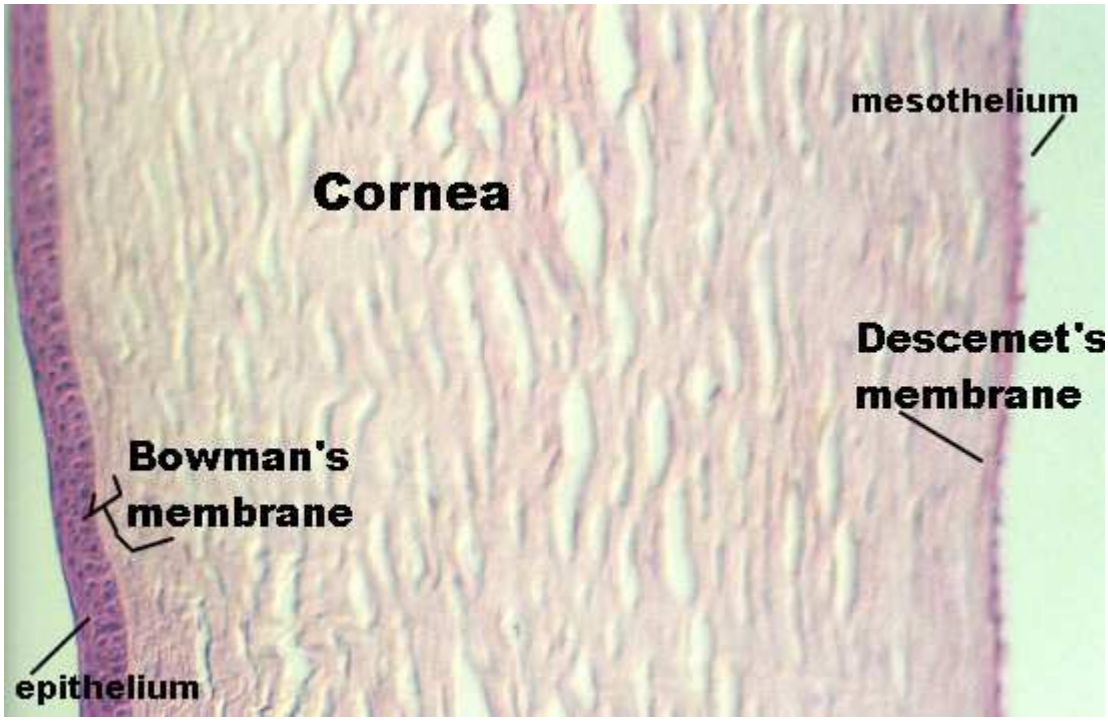

Figure 3.2: Structure of cornea. An overview of the cornea proper is shown below. The thicker epithelium is facing anteriorly (left). (Therefore, the outside of the eye would be to the left.) Underneath the epithelium is Bowman's membrane, which is a condensed region that begins the cornea proper. Finally Descemet's membrane lies at the opposite side, just underneath the mesothelium. The anterior chamber faces to the right.

3.1.2.1 Epithelium

The corneal and conjunctival epithelia are continuous and together form the ocular surface. The

corneal epithelium is composed of nonkeratinized, stratified squamous epithelial cells. The thickness of the corneal epithelium of humans is approximately 50 micron, which is about 10% of the total thickness of the cornea. Epithelium is constant over the entire corneal surface. The corneal epithelium consists of five or six layers of three different types of epithelial cells: two or three layers of superficial cells, two or three layers of wing cells, and a monolayer of columnar basal cells, the latter of which adhere to the basement membrane adjacent to Bowman´s layer.

The epithelium, together with the tear film, contributes to maintenance of the optically smooth corneal surface. In individuals with dry eye, the surface of the corneal epithelium is dehydrated and becomes pitted and irregular. This loss of smoothness of the epithelial surface results in degradation of the optical image and consequent blurred vision. Another important physiological role of the corneal epithelium is to provide a barrier to external biological and chemical substances insults. The presence of junctional complexes between adjacent corneal epithelial cells prevents passage of chemical substances into the deeper layers of the cornea.

3.1.2.2 Bowman`s layer

An acellular membrance-like zone known as Bowman`s layer is at the interface between the corneal epithelium and stroma in humans. It is 12 micron thick. It is a random arrangement of collagen fibers and proteoglycans. The collagen fibers in Bowman`s layer are primarily collagen types Ⅰ and Ⅲ. The diameter of these fibers is 20 to 30 micron, which is smaller than that of the collagen fibers present in the corneal stroma which is 22.5 to 35 micron thick.

Bowman´s layer is considered to be the anterior portion of the corneal stroma. The anterior surface of this layer, which faces the basement membrane, is smooth. Given that the collagen fibers in Bowman`s layer are synthesized and secreted by stromal keratocytes, they appear continuous with those in the stroma.

3.1.2.3 Stroma

The stroma constitutes the largest portion, more than 90%, of the cornea. Many characteristics of the cornea, including its physical strength, stability of shape, and transparency, are largely attributable to the anatomic and biochemical properties of the stroma. The uniform arrangement and continuous slow production and degradation of collagen fibers in the stroma are essential for corneal transparency.

The corneal stroma consists of extracellular matrix, keratocytes, namely corneal fibroblasts, and nerve fibers. The cellular components occupy only 2% to 3% of the total volume [37]. More than 70% of the dry weight of the cornea is the collagen. These collagens are mostly type Ⅰ, with smaller amounts of types Ⅲ, Ⅴ, and Ⅵ [38][39].

Individual collagen fibers in the corneal stroma can be observed by transmission electron microscopy. The collagen fibers in the stroma are highly uniform in diameter with change from 22.5 nm to 35nm [40]. The distance between the collagen fibers is also highly uniform [41]. The regular arrangement of collagen fibers is a major determinant of corneal transparency. Any disturbance in the uniformity of interfiber distance will cause the loss of corneal transparency. Each collagen fiber exhibits a characteristic cross-striation pattern with a periodicity of l67 nm. In the corneal stroma, the collagen fibers form about 300 lamella [42]. Each lamella courses parallel to the surface of the cornea from limbus to limbus. Between collagen fibers in the corneal stroma are various glycosaminoglycans and most of them are hyaluronan. These glycosaminoglycans bind to core proteins to form proteoglycans. Glycosaminoglycans have the ability to absorb and retain large amounts of water. The major glycosaminolycan is hyaluronan in the embryonic eye. Proteoglycans are thought to modulate collagen fibrillogenesis [43]. Keratocytes are the predominant cellular components of the corneal stroma. The spindle-shaped keratocytes are scattered between the lamella in cross-section. These cells extend long process and the process of neighboring cells are connected at their tips by gap junctions [44]. The gap junctions in these cells

are functional and serve to transmit intercellular signals.

Keratocytes possess an extensive intracellular cytoskeleton, including prominent actin filaments. This property allows the cells to contract and may be responsible for the maintenance of corneal shape and for the packed structure of collagen.

3.1.2.4 Descemet´s membrane

Descemet´s membrane is a thin layer adjacent to the stroma. Collagen fibers in the stroma are not continuous with those in Descemet´s membrane. Descemet´s membrane adheres tightly to the posterior surface of the corneal stroma and reflects any change in the shape of the stroma.

3.1.2.5 Endothelium

A single layer of corneal endothelial cells covers the posterior surface of Descemet´s membrane in a well-arranged mosaic pattern. These cells are uniformly 5 micron thick and 20 micron wide and are polygonal in shape. The most important physiological function of the endothelium is regulation of the water content of the corneal stroma.

3.1.3 Collagen

Collagen is the major structural protein in the human body. About one quarter of all the protein in the human body is collagen. It is nearly everywhere and it is a relatively simple molecule. Collagen, as the most abundant protein in the human body, determines the unique physiological

and optical properties of the connective tissues including cornea. Collagen is composed of three chains that are wound together in a tight triple helix. There is also another property of collagen: it is able to generate second harmonics signals (SHG). This is a result of the non-centrosymmetric build up of the collagen fibrils.

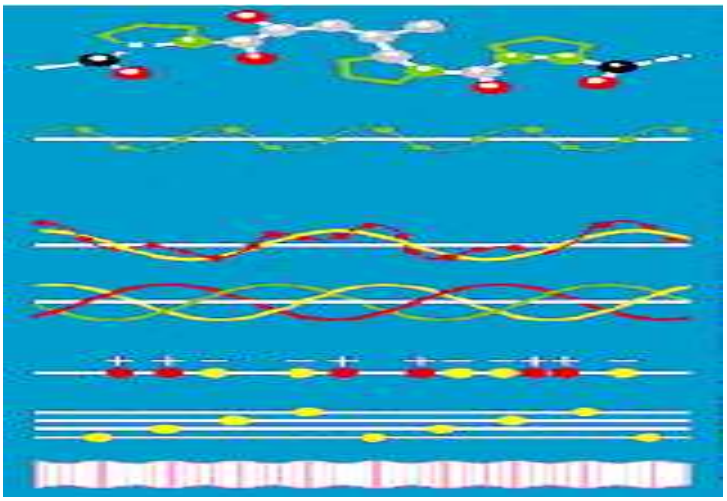

Figure 3.3: Schematic of the collagen structure. Starting at the top with the molecular structure and ending in a schematic drawing of a collagen fibril as it can be seen in electron microscope pictures.

3.2 Laser tissue interaction

Numerous studies investigated the interaction of pulsed laser radiation with bulk material. A common finding is that the short pulse damage is deterministic in nature and the threshold is lower with shorter laser pulses. There are a few different types of laser tissue interaction, which are described here.

There are five types of laser tissue interaction: photochemical interactions, thermal interactions, photoablation, plasma-induced ablation, and photodisruption [45]. All these seemingly different

interaction types share a single common datum: the characteristic energy density ranges from approximately 1 J/cm^2 to 1000 J/cm^2. Thus a single parameter distinguishes and primarily controls these processes: the duration of laser exposure which is mainly identical with the interaction time itself.

The map of laser tissue interactions is shown below. The unit of power density is W/cm^2, the unit of exposure time is seconds. Two diagonals show constant energy fluences at 1 J/cm^2 and 1000 J/cm^2. Divided by time scale there are four regions: continuous wave or exposure times bigger than one second for photochemical interaction; exposure times from one minute to one microsecond for thermal interactions; exposure times from one microsecond to one nanosecond for photoablation; exposure times smaller than one nanosecond for plasma induced ablation and photodisruption. The difference between the latter two is attributed to different energy densities.

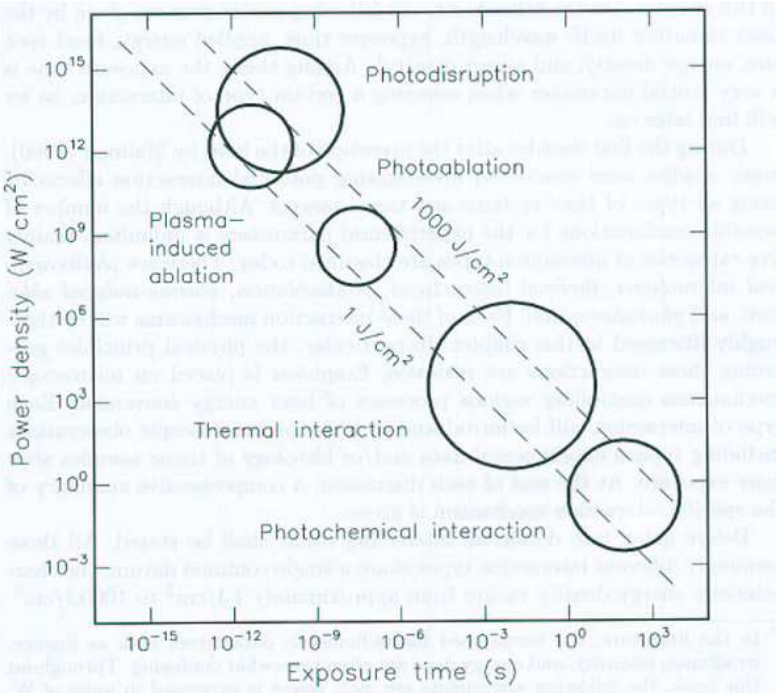

Figure 3.4: Map of laser tissue interactions. Modified from Boulnois [46].

3.2.1 Photochemical Interaction

Photochemical interactions take place at very low power densities, for example 1 W/cm^2, and long exposure times range from seconds to continuous wave. The main idea of photochemical is to use a chromophore receptor acting as a catalyst. Its excited states have the ability to store energy transferred from resonant absorption, and their deactivation leads to toxic compounds leaving the photosensitizer in its original state. This is the reason its other name is photosensitized oxidation.

.2.2 Thermal Interaction

The name thermal interaction comes from the increase in local temperature which is the significant parameter change. Either continuous wave lasers or pulsed lasers can induce the thermal effects. While photochemical processes are often governed by a specific reaction pathway, thermal effects generally tend to be nonspecific according to Parrish and Deutsch [47]. Different in the duration and peak value of the tissue temperature achieved, the thermal interaction can be distinguished as four types: coagulation, vaporization, varbonization, and melting.

3.2.3 Photoablation

Srinivasan and Mayne-Banton discovered the phtoablation effect first [48]. They identified it as ablative photodecomposition, in other words that material is decomposed when exposed to highly intense laser irradiation. The precision of the etching process and the lack of thermal damage to

adjacent tissue are the main advantages of this ablation. Excimer lasers have the photoablation ability to direct breaking of molecular bonds by high energy UV photos and are popular in refractive corneal surgery today.

3.2.4 Plasma-Induced Ablation

A phenomenon called optical breakdown will occur when obtaining power densities exceeding 10^{11} W/cm^2 in solids and fluids or 10^{14} W/cm^2 in air. A bright plasma spark is clearly visible with this effect. Without thermal or mechanical damage the tissue can be removed very cleanly and well defined by this effect. Another name for plasma induced ablation is plasma mediated ablation. It was investigated and discussed by Teng et al [49], Stern et al [50], and Niemz et al [51]. Both synonyms express a generally well-accepted interpretation that this kind of ablation is primarily caused by plasma ionization itself. The local electric field strength E is the most important parameter of plasma-induced ablation and it determines when optical breakdown is achieved. If E exceeds a certain threshold value, it means the applied electric field forces the ionization of molecules and atoms; then the breakdown occurs. The local power density I is expressed by the electric field strength as:

$$I(r,z,t) = \frac{1}{2}\varepsilon_0 cE^2$$

where ε_0 is the dielectric constant and c is the speed of light. Plasma generation due to an intense electric field is called dielectric breakdown normally. The name optical breakdown especially emphasizes that light is strongly absorbed by the plasma.

Puliafito and Steinert describe the initiation of plasma generation as a two-fold process [52]. Either Q-switched pulses in the nanosecond range or mode locked laser pulses in the picosecond or femtosecond range can induce the microplasma. The release of electrons due to thermal ionization, which is called thermionic emission, is the initial process for the generation of free

electrons in Q-switched pulses. The intense laser pulses induce the high electric field which cause multi-photon ionization in mode locked pulses. Normally coherent absorption of several photons provides the energy needed for multi-photon ionization. Multi-photon ionization is achievable only during high peak intensities as in picosecond or femtosecond laser pulses because of the coherence requirement. In both cases at beginning a few electrons initiate an avalanche effect, leading to the accumulation of free electrons and ions. The first step is that a free electron absorbs a photon and accelerates. The second step is that the accelerated electron collides with another atom and ionizes it. The result is two free electrons and both have less individual kinetic energy than the initial electron. The third step is that these free electrons absorb photons, accelerate, strike other atoms, and release two more electrons. These steps will continue on and more and more free electrons will be induced.

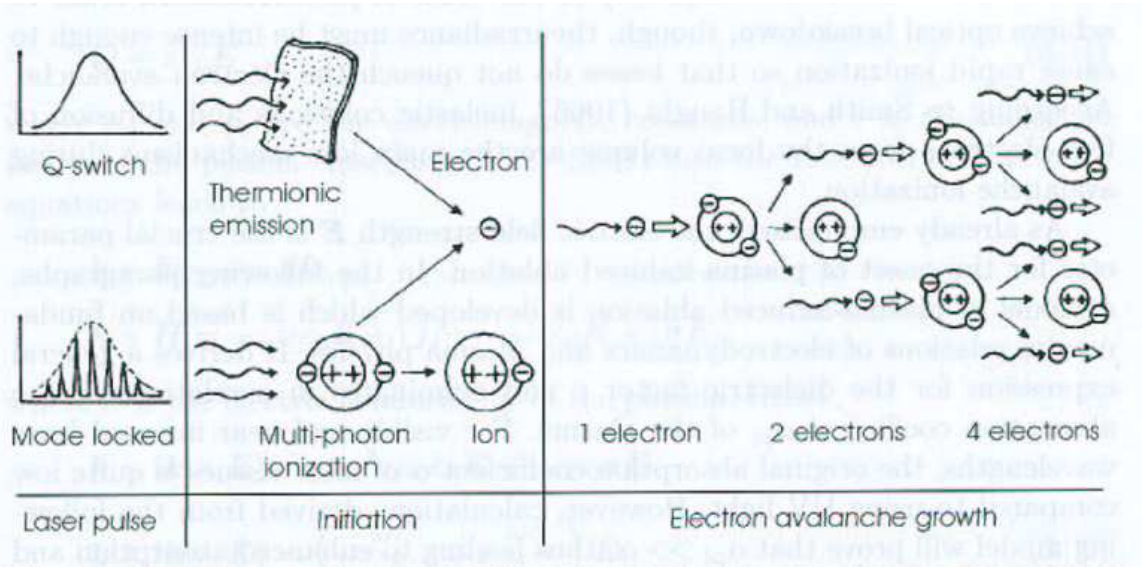

Figure 3.5: Initiation of ionization with subsequent electron avalanche.

Due to the increased absorption coefficient of the induced plasma one important feature of optical breakdown is that it renders an energy deposition in nominally weakly absorbing media.

Therefore transparent tissue like cornea can become a target of medical laser application. In order to achieve optical breakdown the irradiance must be intense enough to cause rapid ionization so that losses do not quench the electron avalanche. Smith and Haught indicated that during the avalanche ionization process the main loss mechanisms are inelastic collisions and diffusion of free electrons from the local volume [53].

3.2.5 Photodisruption

Plasma formation and shock wave generation are physical effects associated with optical breakdown. Cavitation and jet formation may additionally take place if breakdown occurs inside soft tissues or fluids. Different from the plasma induced ablation, secondary effects of the plasma at higher pulse energies like shock waves become more significant. After Krasnov introduced the photodisruption effect Aron-Rosa et al and Kankhauser et al further investigated [54][55][56]. The tissue is split by mechanical forces during photodisruption. In the breakdown region the effect is plasma induced ablation while in the adjacent region the effects are shock wave and cavitation. Since adjacent tissue can be damaged by disruptive forces, the presence of these effects is often an undesired but associated symptom. Picosecond and femtosecond pulses can reduce the disruptive effects with the ability to generate of high peak intensities with considerably lower pulse energies. Niemz found that in the case of picosecond pulses ablation without mechanical side effects takes place at incident power densities of a few times the plasma threshold [57]. The difference between the plasma induced ablation and photodisruption is the different power energy during the process as shown in Figure 3.6.

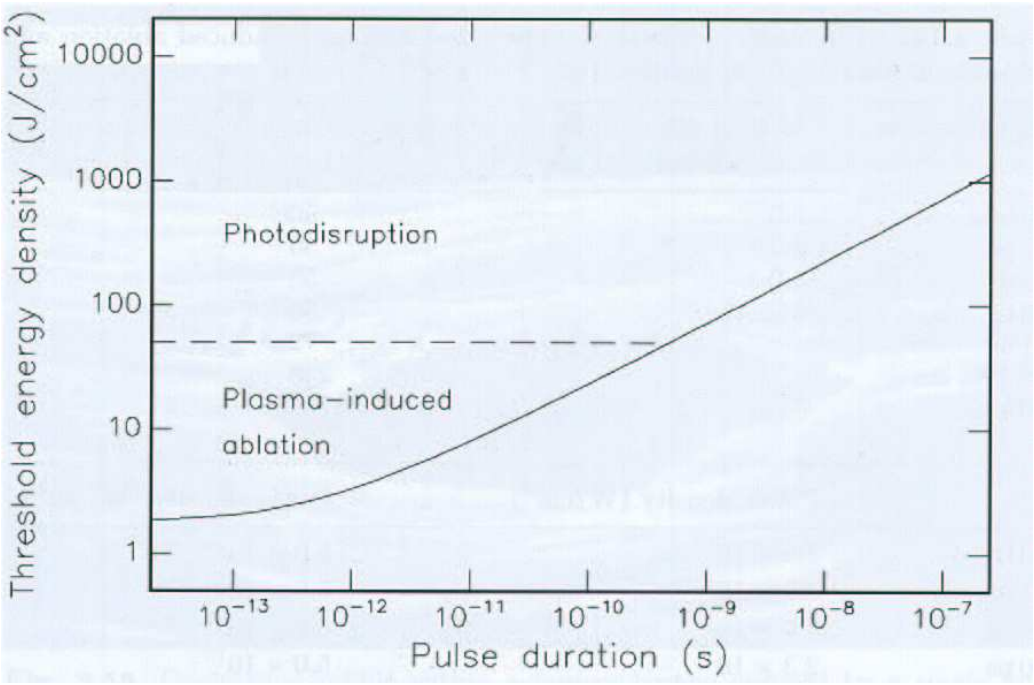

Figure 3.6: Distinction of plasma induced ablation and photodisruption according to applied energy density.

Photodisruption is a multi-cause mechanical effect starting with optical breakdown. Shock wave generation and cavitation are the primary mechanisms, completed by jet formation if cavitations collapse in fluids and near a solid boundary. Their relations to each other is shown in Figure 3.7.

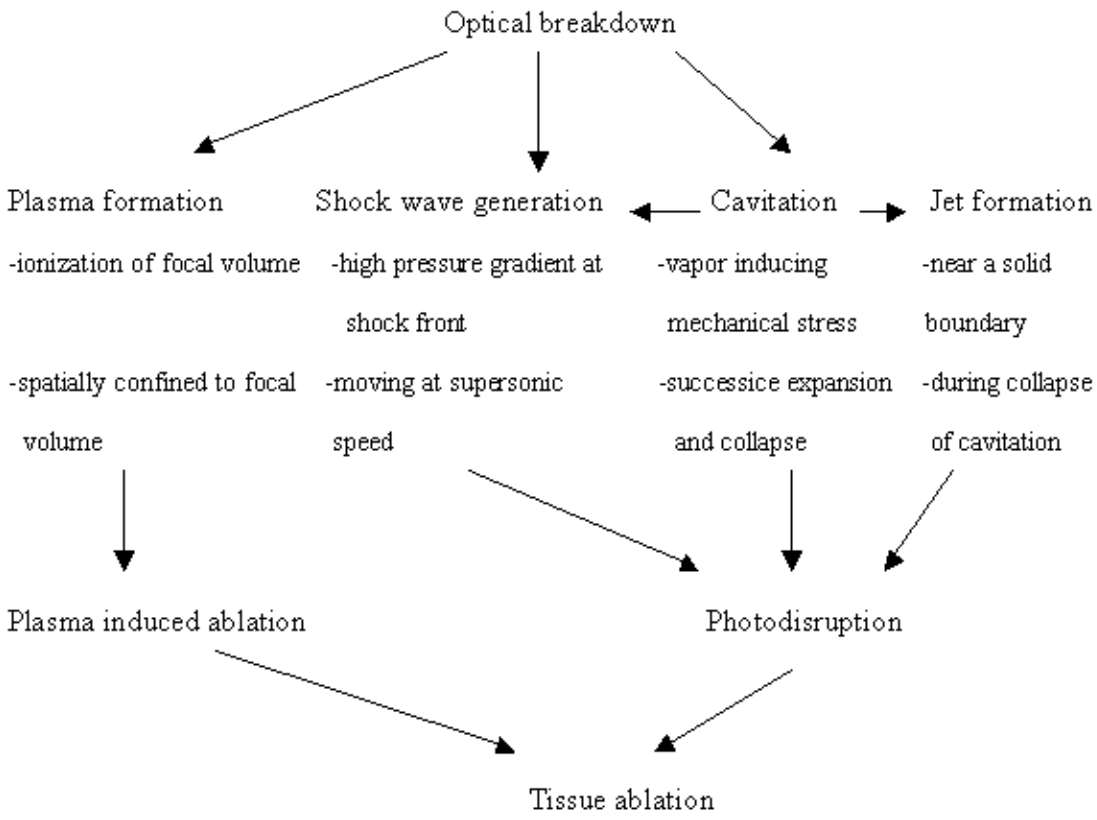

Figure 3.7: Physical processes associated with optical breakdown.

Plasma formation, shock wave generation, cavitation, and jet formation take place on different time scales. Plasma formation begins during the laser pulse and lasts for a few nanoseconds. This is the same time for the free electrons to diffuse into the surrounding medium. Shock wave generation starts during plasma formation and is associated with the plasma expansion. After it generation of the shock wave propagates into adjacent tissue and slows down to an ordinary acoustic wave. Cavitation is a macroscopic effect and cavitation bubble performs several oscillations of expansion and collapses.

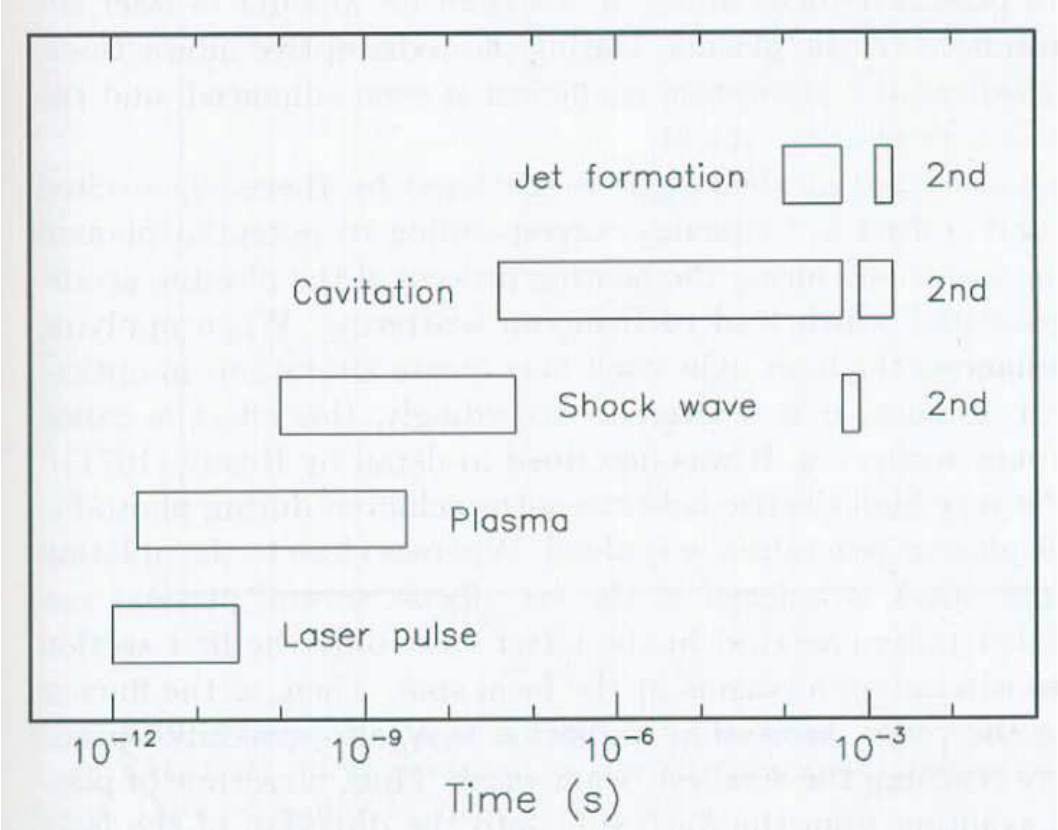

Figure 3.8: Time scale of the processes that compose the photodisruption.

3.3 Second harmonic generation in collagen

Collagen, as the major component of corneal tissue, displays the unique properties of second harmonic generation (SHG) [58]. We used the second harmonic gereration for a threshold experiment and for the microscopic effects of femtosecond laser intrastromal surgery. Here we introduce the principle of second harmonic generation.

Collagen is composed of three parallel, intertwined, polar helices. In collagen type I two of these strands are the same while the third one is slightly different. As a result of this, the collagen molecule has cylindrical symmetry about its long axis. Here we choose the polar axis as the z axis, choose x and y axis as an arbitrary orthogonal set in a plane that is normal to the z axis. Induced

by optical fields $\vec{E}(\omega)$, the components of the harmonic generation $\vec{P}(2\omega)$ are [59]:

$$
\begin{aligned}
P_z(2\omega) &= \beta_3 E_z^2(\omega) + \beta_1\left[E_x^2(\omega) + E_y^2(y)\right] \\
P_x(2\omega) &= 2\beta_1 E_x(\omega) E_z(\omega) \qquad (3.1) \\
P_y(2\omega) &= 2\beta_1 E_y(\omega) E_z(\omega)
\end{aligned}
$$

where $\beta_3 = \beta_{zzz}$, $\beta_1 = \beta_{zxx} = \beta_{zyy} = \beta_{xzx} = \beta_{yzy} = \ldots$

These equations follow from the form of the C_∞ piezoelectric tensor as given by Fukada [60], the formal equivalence to the hyperpolarizability tensor, and the assumed validity of the Kleinman [61] symmetry conditions. Kleinman symmetry means that all of the elements in the nonlinear susceptibility tensor that are connected by permutation of indices that are equal.

Within a fibril the collagen molecules are aligned parallel so that the above equations also describe the second harmonic generation by a single fiber as

$\beta_{fibril} = N\,\beta_{molecule}$

here N is the number of the molecules inside the fibril. From this point a fibril can be treated like a simple, supergiant molecule. This assumption is approximately correct as long as the sample geometry and fibril dimensions are such that the relative phases of the various optical fields do not vary appreciably over an individual fibril. The experiment setup as Figure 3.9 was used by Shmuel Roth and Isaac Freund [59].

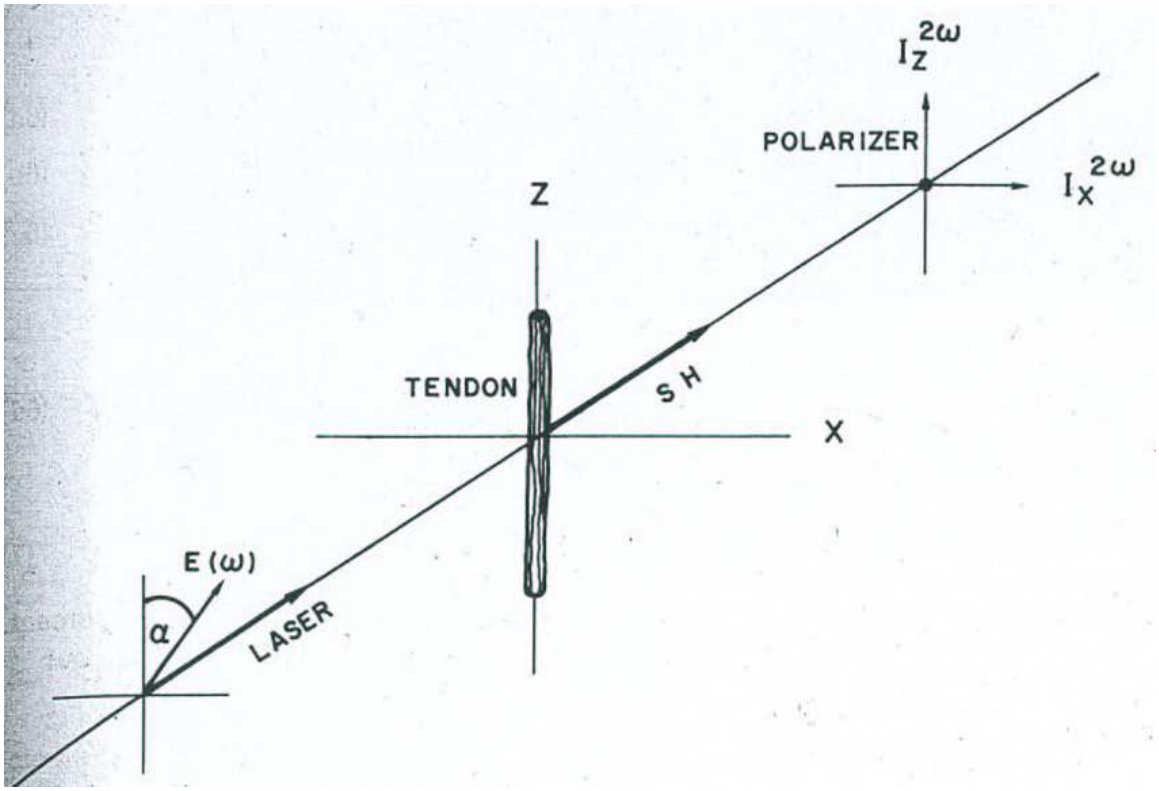

Figure 3.9: Setup to explain the second harmonic generation in collagen.

With this experimental geometry Shmuel Roth and Isaac Freund measured the intensity of second harmonic generation for which the harmonic is polarized parallel to the tendon axis, $I_Z^{2\omega}(\alpha)$, and normal to the tendon axis $I_X^{2\omega}(\alpha)$, as a function of the angle α that the incident laser polarization makes relative to the Z- axis. The external reference frame is denoted by XYZ as shown in Figure 3.9, the fibril reference frame by xyz as in equation (3.1), and we assume the z axis, the fibril axis, to be the polar angle θ and the azimuthal angle ϕ relative to the XYZ frame.

At the location of the fibril the incident laser field consists of two orthogonal components oriented along the tendon Z- and X-axes which is written for unit amplitude as

$$E_Z(\omega) = \cos\alpha$$
$$E_X(\omega) = e^{i\delta}\sin\alpha \qquad (3.2)$$

in the birefringent tendon the two components of the laser propagete with different phase velocities so that we have the factor $e^{i\delta}$ in the the equation (3.2). The components of the fields in equation (3.2) give rise to the fields $E_X(\omega)$, $E_Y(\omega)$ and $E_Z(\omega)$ of equation (3.1) in the fibril reference frame. These produce the nonlinear polarizations of equation (3.1), which then combine in the tendon frame as macroscopic components which may be written as

$$P_j(2\omega) = A_j + B_j e^{i\delta} + C_j e^{2i\delta}$$

Within the tendon the relative phase δ varies from location to location. Because of this we average $\left|P_j(2\omega)\right|^2$ over all δ, writing for the second harmonic intensity $I_j^{2\omega} = \left|P_j(2\omega)\right|^2$, with

$$\left|P_j(2\omega)\right|^2 = A_j^2 + B_j^2 + C_j^2$$

Assuming cylindrical symmetry about the tendon axis for the distribution of fibril orientations, A^2, B^2, and C^2 of the equation above are averaged over all ϕ. A normalized distribution function $\Pi(\theta)$ is used to describe the orientation distribution of the fibrils. The reason for this arises from the fact that stretching the tendon does not completely straighten the individual fibers but leaves a residual wavy pattern. This can be approximated by a sinusoid running along the Z axis with the displacement, for example, in the X-Z plane we have

X=a sin(kZ)

The angle θ that the fibrils comprising the fiber make with the Z axis is easily seen to be

$\theta = \tan^{-1}[\text{akcos}(kZ)]$

by introducing this normalized distribution function $\Pi(\theta)$ which describes the fibril orientations then we obtain

$$I_Z^{2\omega}(\alpha) = Q\sin^4\alpha + R\sin^2 2\alpha + S\cos^4\alpha$$
$$I_X^{2\omega}(\alpha) = T\sin^4\alpha + Q\sin^2 2\alpha + R\cos^4\alpha \qquad (3.3)$$

with

$$Q = \frac{1}{8}\left\{(3\rho^2 - 10\rho + 11)I_2 + (-6\rho^2 + 28\rho - 30)I_4 + (3\rho^2 - 18\rho + 27)I_6\right\}$$
$$R = \frac{1}{2}\left\{1 + (2\rho - 7)I_2 + (\rho^2 - 8\rho + 15)I_4 + (-\rho^2 + 6\rho - 9)I_6\right\}$$
$$S = 9I_2 + (6\rho - 18)I_4 + (\rho^2 - 6\rho + 9)I_6 \qquad (3.4)$$
$$T = \frac{1}{16}\left\{\begin{array}{l}(5\rho^2 + 6\rho + 9) + (-15\rho^2 + 18\rho + 9)I_2 + (15\rho^2 - 54\rho + 27)I_4 \\ + (-5\rho^2 + 30\rho - 45)I_6\end{array}\right\}$$

where $\rho = \beta_3/\beta_1$,

$$I_m = \int_0^{\theta_{max}} d\theta \cos^m\theta \prod(\theta) \qquad (3.5)$$

the maximum possible angular displacement is θ_{max}. All constants are neglected in equation (3.4) since the results of measurement are always of relative intensities. In equation (3.5) $\theta_{max} = \tan^{-1}(ak)$. $\prod(\theta)d\theta$ may be seen to be proportional to the length of arc over which θ changes by no more than $d\theta$, in other words, $\prod(\theta)$ is proportional to one over the curvature, so that except for normalization,

$$\prod(\theta) = \left[k\cos^2\theta\sqrt{(ak)^2 - \sin^2\theta\left[1 + (ak)^2\right]}\right]^{-1}$$

To verify these consideratins a perfectly ordered array of fibrils is considered, i.e., $\theta_{max} = 0$, since this represents a reasonable first approximation to the actual situation and provides a useful initial guide to the interpretation of the measurements. With this assumption it may be written

$$I_Z^{2\omega}(\alpha) = \beta_1^2\sin^4\alpha + \beta_3^2\cos^4\alpha$$
$$I_X^{2\omega}(\alpha) = \beta_1^2\sin^2 2\alpha \qquad (3.6)$$

A plot of equation (3.6) can be seen as Figure 3.10.

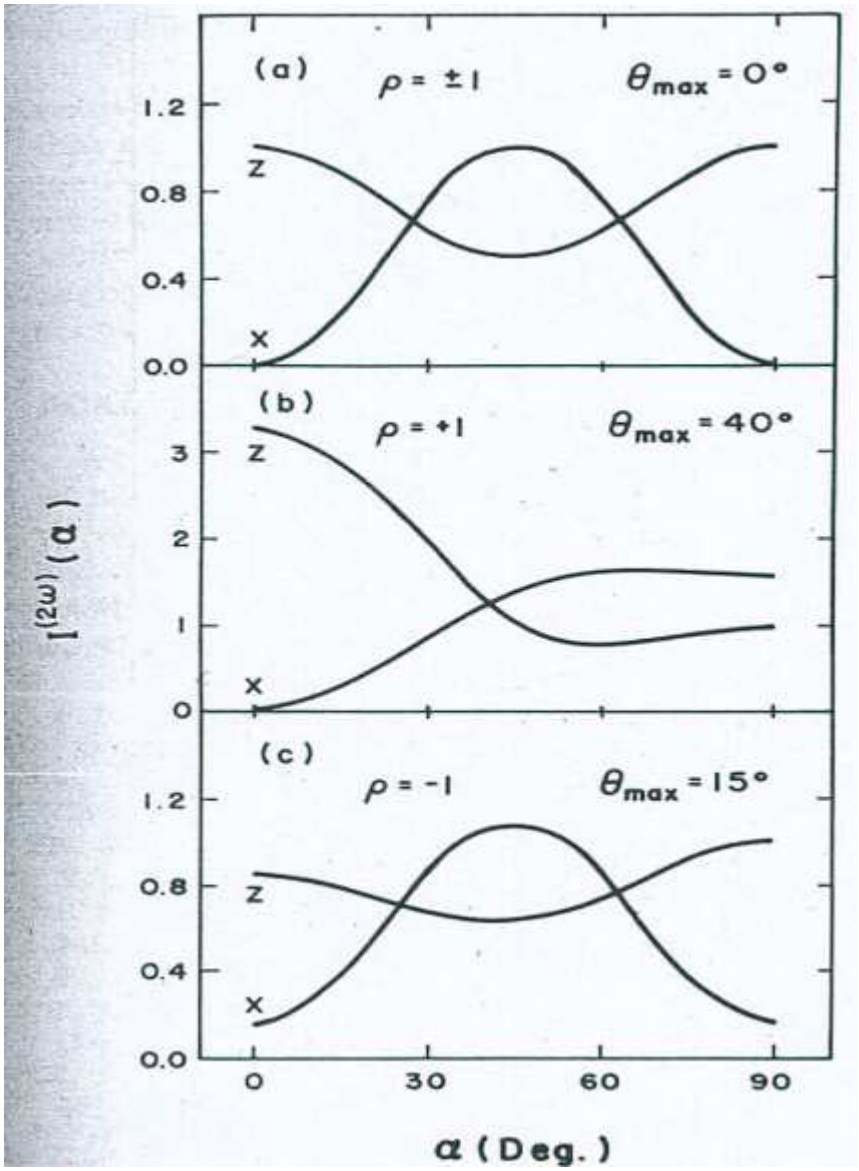

Figure 3.10: Calculated $I^{2\omega}$ curves for different values of ρ and θ_{max}. (a) Perfectly ordered tendon, equation (3.6); (b) equation (3.3) and (3.4) for $\rho > 0$; (c) equation (3.3) and (3.4) for $\rho < 0$.

Chapter 4 Nonlinear Laser-Tissue Interactions Experiments

In this chapter the experiments and results of my Ph.D study are described. It is composed of five parts. The first part introduces the preparation of the experiments, including the sample preparation and the knife-edge method. The second part introduces a new method to determine the threshold of the cornea, i.e. detecting the plasma spark and the second harmonic generation signal at the same time. The third part introduces our ultra fast laser system and microscope method determining the threshold. The fourth part introduces the results coming from the multi-photon microscope by second harmonic generation. The last part introduces the effect of spot split grating.

4.1 Preparation for experiments

4.1.1 Porcine cornea preparation

All excised porcine eyeballs were obtained from the local slaughterhouse. The corneas were cut just before the experiment to insure that the corneas were in a status similar to the live ones. Some corneas already had damaged epithelium so we carefully removed the epithelium before the experiment. Some corneas had intact epithelium so we retained all the parts of the cornea to experiment. The cornea was translated between experiment shots, so that each site was illuminated only once. During the experiment the 4% Phosphate Buffered Saline (PBS, pH 7.4) solution was sprayed regularly on all the samples in order to prevent them from dehydration. After the experiment the tissues were immediately fixed with freshly prepared paraformaldehyde

(4% in PBS, pH 7.4) to be checked by multi-photon microscope later.

4.1.2 Knife-edge method of determining the focus size

The application of lasers to investigate biophysical phenomena requires knowledge of the waist diameter of a focus beam. Although techniques such as ray tracing [62], multiphoton ionization yields [63], and fluorescence correlation spectroscopy [64] predict accurate results, such methods are either too complicated for most general applications or they rely on specific experimental procedures not easily adaptable to other experiments. Correlation of the square of the diameter of a spot burned by the laser beam with the logarithm of the normalized power absorbed is another direct method for determining beam diameters [65]. In addition, a photoelectric detector array can probe directly the intensity profile of the laser [66].

Another method involves gradual eclipsing of the laser beam by a sharp knife-edge [67]. The intensity of the unmasked portion of the laser beam was measured while the knife-edge intersected the laser beam in a direction perpendicular to the propagation axis of the laser beam. If the laser beam is in the TEM_{00} mode then the beam profile is described by the Gaussian line shape [68], that the signal measured by this method is represented by an integrated Gaussian function. In principle the laser beam diameter can be determined. This method is simple, inexpensive, and pretty effective at the same time. It has traditionally been used with mechanical scanning laser beam width measurements as in our case [69]. The experiment setup is shown in Figure 4.1. By moving the knife-edge we measured a series of power. The different values between the two adjacent points will shape a Gaussian line. The full width at half maximum (FWHM) in the fitting line is considered as the width of the laser beam.

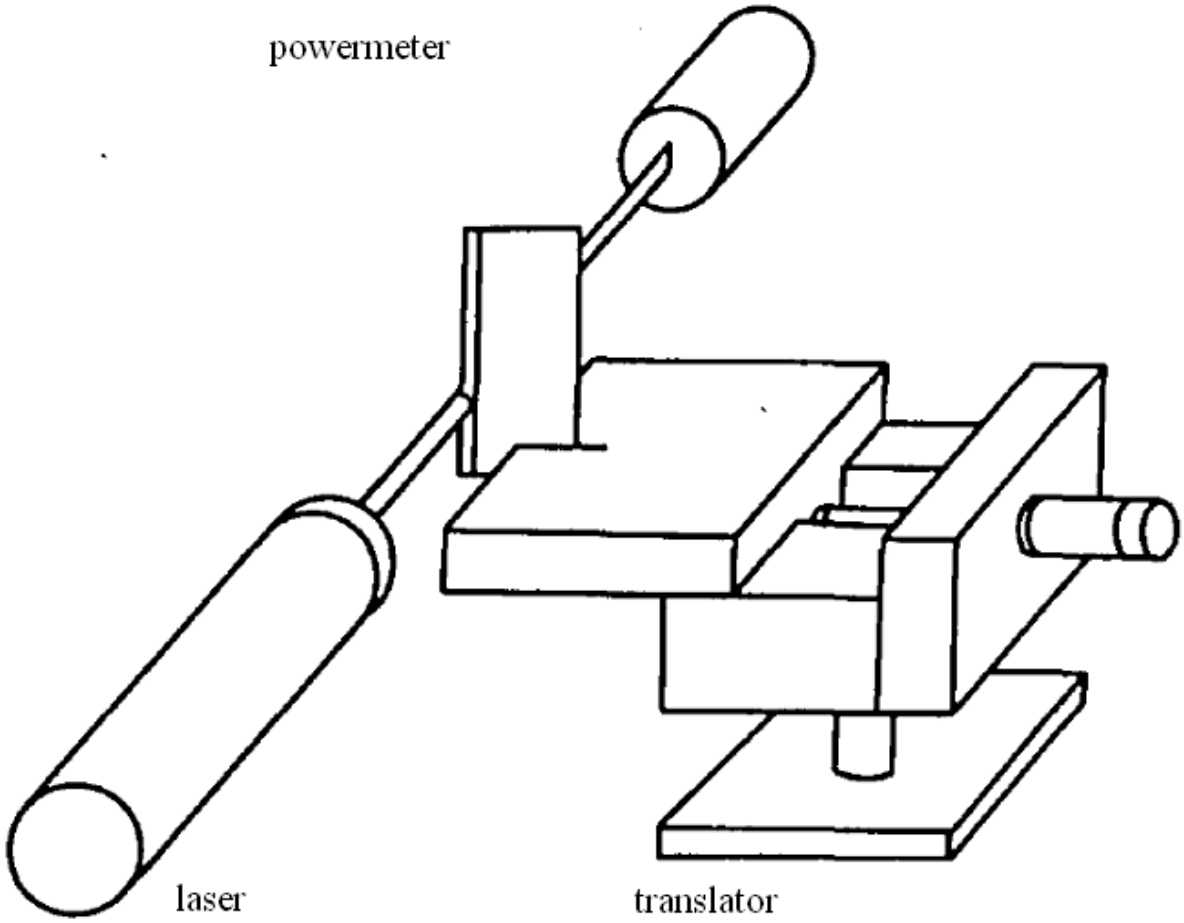

Figure 4.1: Knife-edge method to measure the spot size of the focus laser beam.

Though observing the intensity of plasma coming from the paper in the focus point of laser beam, one can roughly determine the position of the focus objective's focus point and lable it as the zero point in the laser beam's propagation axis. In front of and behind this zero position I measured a series of spot sizes with the knife-edge method. The data of the knife-edge method measured in the zero position is listed in Table 4.1. The two pictures below are laser beam width at zero point and laser beam width at a five micron meters behind this zero point.

Table 4.1 knife-edge data at zero point.

Position (mm)	Measured power (mW)	Calculated power (mW)
22.418	5.300	0.000
22.415	5.300	0.240
22.410	5.060	0.770
22.405	4.290	0.920
22.400	3.370	1.300
22.395	2.070	0.860
22.390	1.210	0.460
22.385	0.750	0.220
22.380	0.530	0.280
22.375	0.250	0.070
22.370	0.180	0.030
22.365	0.150	0.070
22.360	0.080	0.072
22.355	0.008	0.001
background	0.007	

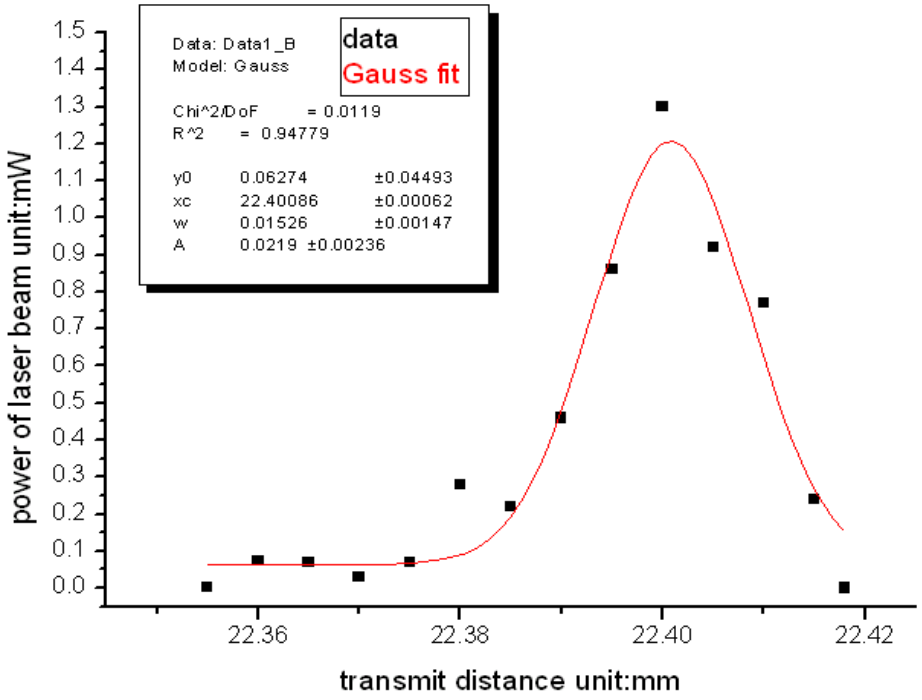

Figure 4.2: Calculated power distribution based on knife-edge measurement at zero position.

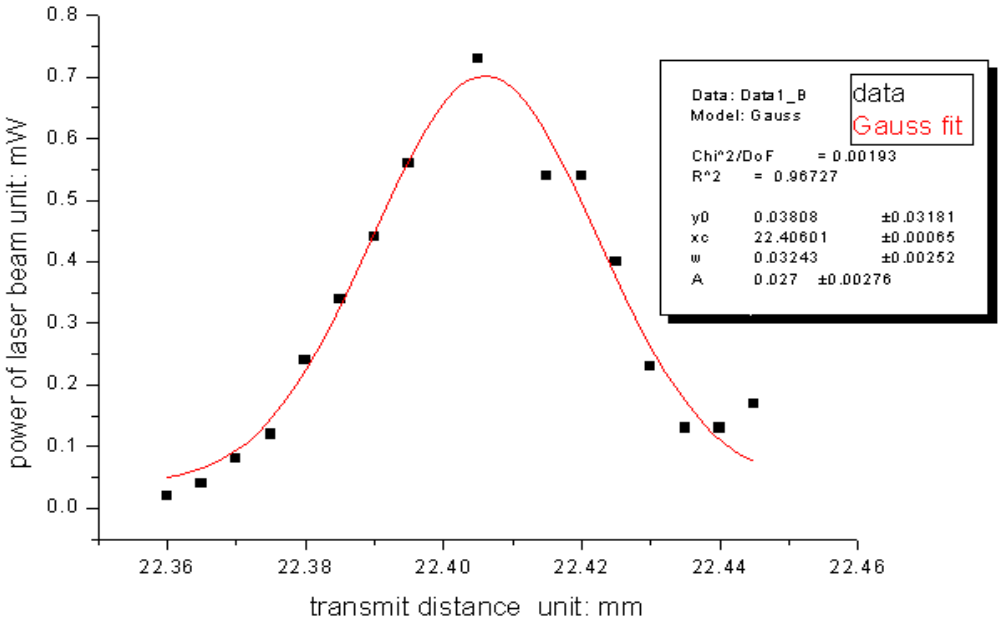

Figure 4.3: Calculated power distribution based on knife-edge measurement at a position five micron meters behind the zero point.

By processing all data with the standard full width at half maximum (FWHM) a curve of the focus laser beam diameter near to the focus point was drawn. The picture is shown below. From the figure it appears that the spot size of the focus point is about 20 micron meters. It is really small and is very difficult to measure precisely. From Figure 4.2 and Figure 4.3 it is obvious that the data in Figure 4.3 is better than the data in Figure 4.2 for distribution as a Gauss function. The reason is because the smaller focal point is the more difficult it is to measure precisely.

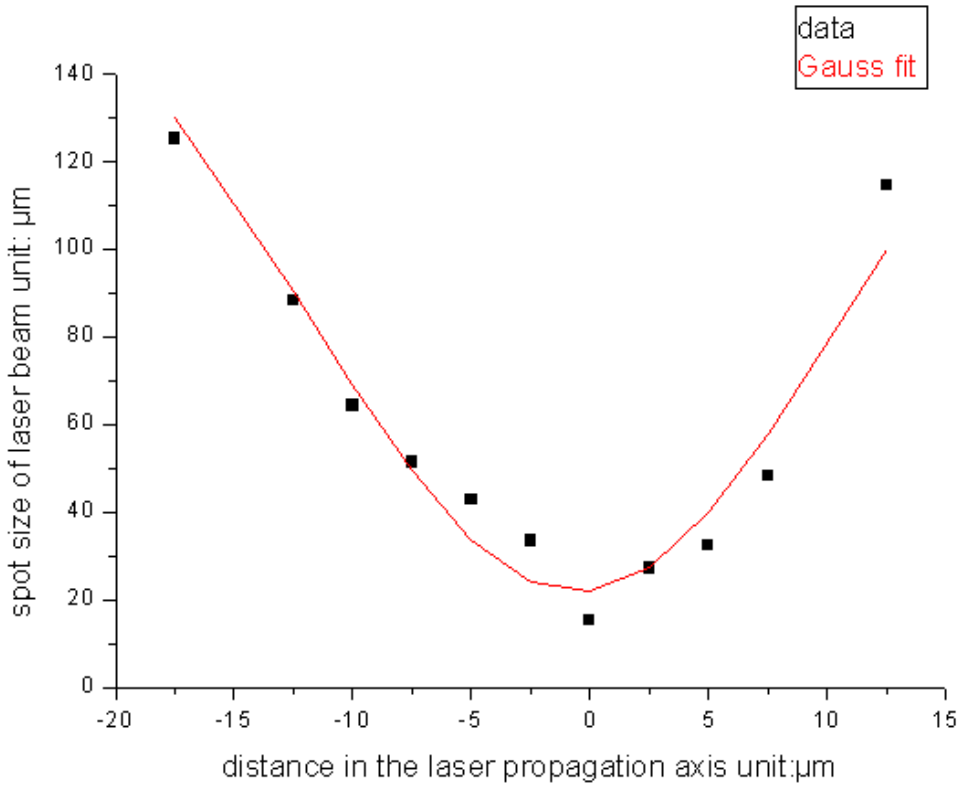

Figure 4.4: Focal spot size near the focus point of the focus objective, which was used in the experiment.

In all the experiments we used the beam expander to full-fill the focus objective, so that we believe the objective is fully used and the diameter of the focal point can be calculated from the formula as [70]

$$h = 0.61\frac{\lambda}{NA}$$

For our Nd:glass femtosecond laser the wavelength is 1054 nm; the radius of focus point size after our focus objective is 5.36 μm because the numerical aperture of the focus objective is 0.12 and the index refractive of air is 1. For our Nd:YAG picosecond laser the radius of focus point size is the same with the same objective. For our Yb:KYW femtosecond laser the radius of focus point size is 5.24 μm for a running wavelength at 1030 nm and is 5.29 μm for a running wavelength at 1040 nm. Then the focal point areas for these lasers are 9.03 $\times$ 10^{-7} cm^2, 8.63 $\times$ 10^{-7} cm^2, and 8.79 $\times$ 10^{-7} cm^2.

4.2 Combined plasma and SHG signals for determination of the threshold

In the last decade, a lot of research in the field of femtosecond eye surgery has proved that it has the advantage of combining high ablation precision with minimized side effects [71][72]. In the year 2000, the first in-vivo studies on flap creation with femtosecond laser as the first procedure of LASIK were evaluated in USA and reported in 2003[73]. The most promising application of femtosecond laser eye surgery is the introstromal ablation [74][75]. More and more reports about this research field appeared in animal experiments [76][77]. Initiated by multi-photon absorption and laser induced optical breakdown, the high-pressure laser plasma non-thermally dissociates the dense corneal tissue thereby enabling mini-invasive intrastromal cornea surgery. The laser-affected region is highly localized, leading to precise ablation with minimized side effects [78]. For best eye surgery results it is important to do the ablation on energies that near the cornea threshold. It is also necessary to know the femtosecond laser ablation threshold dependence on corneal depth and laser pulse width. The threshold ablation was detected by different methods in former research including fluorescein angiography (FA) [79]; scattered light detecting [78], CCD camera checking of the plasma spark [80], and monitoring individual plasma emissions by a lens [81].

Here we report a new method to determine the threshold of the cornea, i.e. detecting the plasma spark and the second harmonic generation signal at the same time. We use the same objective for focusing the laser to the cornea sample and for collecting the plasma spark signal. Since the most promising application of femtosecond laser eye surgery is the intra-stromal ablation, knowing the ablation threshold dependence on corneal depth is of significant importance.

Laser-induced plasma mediated ablation, also known as laser-induced breakdown, relies on nonlinear absorption in the target that is achieved when a material specific irradiance threshold is

exceeded [82]. Plasma formation thus plays an important role in interactions of high power laser irradiation with matter. The threshold radiant exposure for breakdown determines the possible precision of the laser effects used for ablation or dissection. The plasma spark becomes an important signal for the threshold. At the same time the second harmonic generation signals will decrease because the collagen in the focus point is damaged and looses the ability to generate the second harmonic generation signals. In this report the threshold was determined by the plasma spark and the second harmonic generation at the same time. The SHG signal from the cornea collagen helps to focus the laser beam precisely to the tissues at different depths. Porcine cornea samples were treated with three diode pumped all-solid-state ultra fast lasers, namely, a Yb:KYW femtosecond laser [83], a Nd:glass femtosecond laser [4], and a Nd:YAG picosecond laser. The pulse width of the ultra fast laser ranges from 800 femtoseconds to 20 picoseconds. The Nd:glass femtosecond laser is a femtosecond all-solid-state laser based on passive mode locking and chirped pulse amplification (CPA) [84]. For self-starting, reliable femtosecond pulse generation, a semiconductor saturable absorber mirror (SESAM), as one of the end mirrors in the oscillator, produces sub 200 femtosecond pulses at 76 MHZ repetition rates [85] [86]. The output pulses from this oscillator laser are temporally stretched in CPA in order to avoid damage to the optical components in the following amplification stage. The stretched pulses are then coupled into the amplifier laser cavity with an electro-optic crystal (Pockel´s cell) [87]. After reaching the buildup maximum, the pulse is ejected from the amplifier cavity. The amplified pulses are compressed in a grating compression stage to femtoseconds [88]. Due to the gain narrowing effect and uncompensated higher order dispersion, the original pulse duration cannot be fully recovered in a simple grating compressor. The best record is 800 femtoseconds. By changing the distance between the retro reflector and the grating we can easily change the pulse width continuously from 1.6 picoseconds to 5 picoseconds as shown in Figure 4.5.

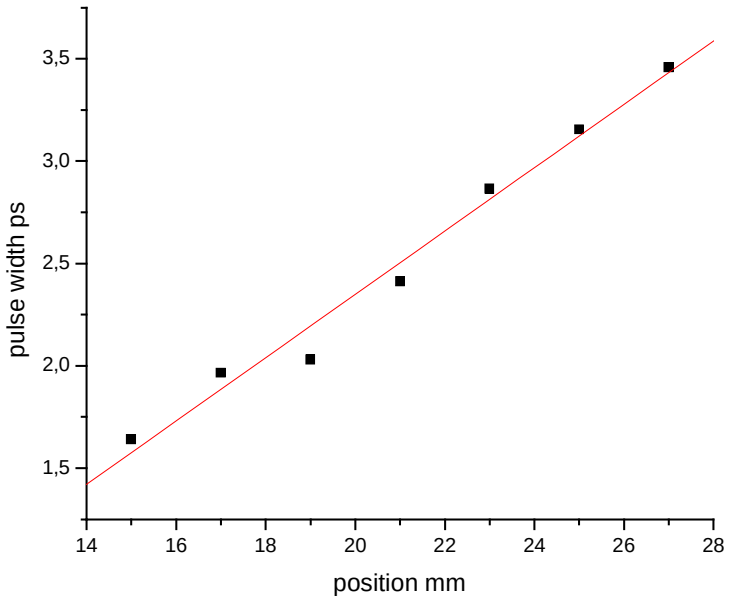

Figure 4.5: Change of pulse width with movement of the position of retro reflector in Nd:glass femtosecond laser system.

Usually chirped pulse amplification (CPA) technology is applied to amplify ultra-short pulses [89]. A disadvantage of this technology is its relative complexity and the requirement for precise alignment of the stretcher and compressor. The thin disk regenerative amplifier concept uses a large cross sectional area to avoid high peak intensity and thus eliminates the need for CPA [83]. GTI mirrors are employed in the regenerative amplifier to compensate the GVD [90]. The Yb:KYW femtosecond laser involved in this research is a system which consists of an oscillator, a telescope, a beam separation unit, and an amplifier. The best record of pulse width with it is 600 femtoseconds. Since the GVD in the system is not yet compensated for by the GTI mirrors, the pulse width increases with the number of roundtrips in the amplifier. When the pulse energy reaches a high level because of the self phase modulation, the pulse width will not increases again. Figure 4.6 and Figure 4.7 show the pulse width as a function of roundtrips for two different wavelengths. In Figure 4.6 the laser is running at wavelength 1041 nm and in Figure 4.7 the laser

is running at wavelength 1030 nm. For a different open time of the Pockel´s cell it requires a different roundtrip time in the amplifier. All the measurements are done with the same pumping current of the crystal in the amplifier to be sure that other conditions are the same and that just the roundtrip times change.

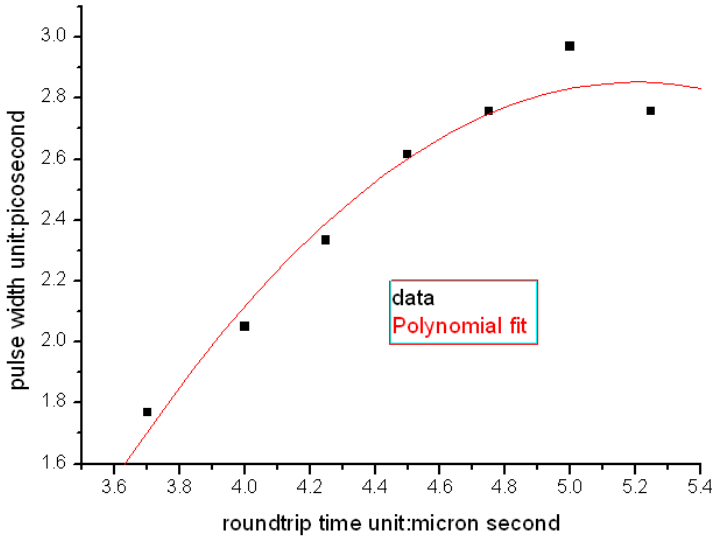

Figure 4.6: Pulse width as a function of the roundtrip time at wavelength 1041 nm.

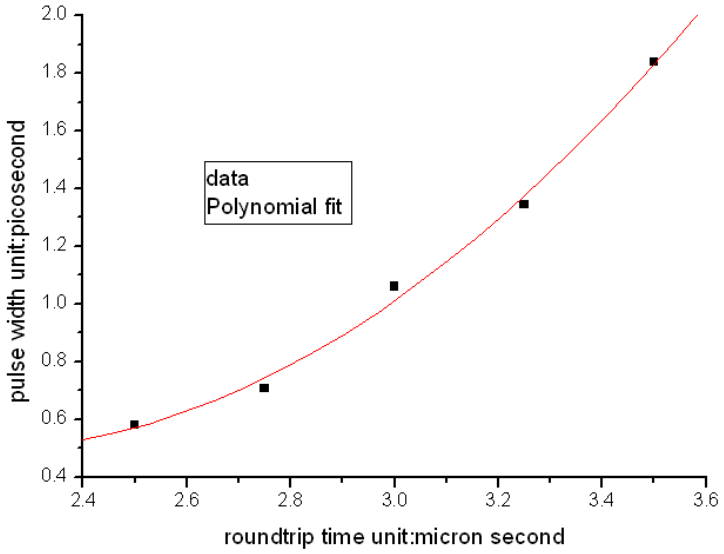

Figure 4.7: Pulse width as a function of the roundtrip time at wavelength 1030 nm.

The Nd:YAG picosecond all-solid-state laser has a simpler structure compared with the other two laser systems. Neither pulse stretching nor dispersion contral is required. One may get a 20 picoseconds pulse with 200μm maximum pulse energy.

The same laser beam delivering system was used to make sure the ablation condition was not changed during the experiment with different laser sources. All excised porcine eyeballs were obtained from the local slaughterhouse as was stated before. The corneas were cut just before the experiment to be sure that the corneas were in the best condition like the live ones. The optical breakdown threshold was determined by monitoring light emitted during plasma formation in the cornea when illuminated by single laser shots and by the intensity change of the second harmonic signals (experimental setup, Fig 4.8). The cornea was moved between shots, so that each site was illuminated only once. After the experiment the tissues were immediately fixed with freshly prepared paraformaldehyde (4% in PBS, pH 7.4). This was done so that one could check the effect with a multi-photon microscope later.

The laser intensity from the laser source was continuously attenuated using a half wave plate and a polarizer. A beam expander was used to totally fill the entry aperture of the focus objective. A 5 ×, 0.12 numerical aperture (NA) objective was used to focus the laser inside the tissue and to collect the plasma spark signal from the cornea sample. Through the PMT these signals are shown in the oscilloscope in real time to determine the threshold immediately. A 20×, 0.4 numerical aperture (NA) was employed to efficiently collect the SHG signal. Through the PMT these signals are connected to a 16bit stereo-mode supported sound card in a computer. The dichroic mirror is used for reflection of near infrared laser light and transmission of plasma spark light. An infrared beam block filer and a second harmonic signal block in front of the reflection light path photo-multiplier tube (PMT) ensured that illumination light and second harmonic signals were excluded and only plasma spark light from the cornea tissue was recorded. An infrared beam block filter and a band pass filter in front of the transmission light path photomultiplier tube (PMT) ensured that illumination light and plasma spark signal were

excluded and only second harmonic signals from the cornea tissue were recorded.

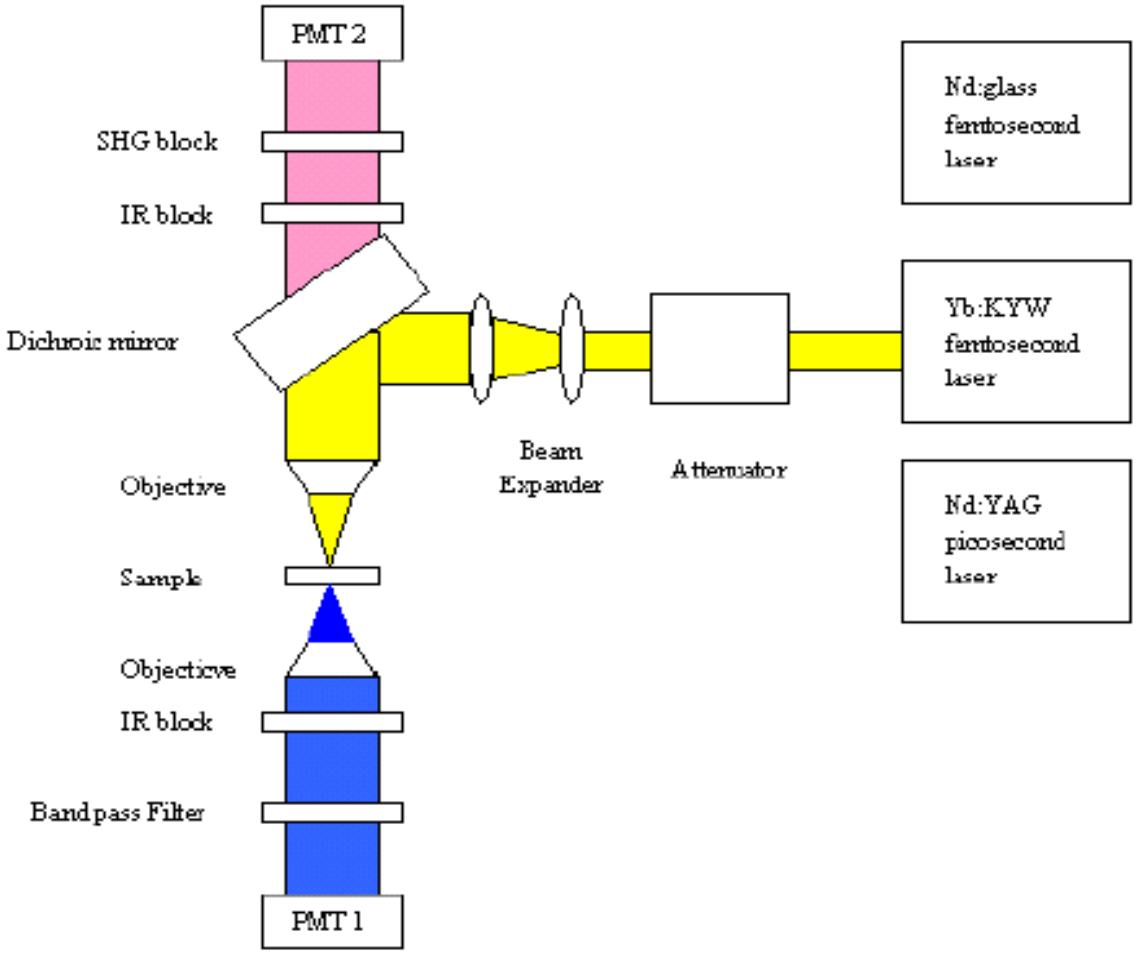

Figure 4.8: Experimental setup: three ultra short laser systems provided laser pulses ranging from 800 femtoseconds to 20 picoseconds in pulse width. The intensity of the input laser beam could be changed continuously while keeping other parameters constant, such as spot size. Porcine cornea was mounted on a computer controlled motorized translation stage for the so-called one-on-one damage experiment. The plasma spark emission from the focal region was collected with the objective to put it into a photo-multiplier tube (PMT) using appropriate filters to block the reflective laser light and second harmonic signal.

The laser-induced optical breakdown (LIOB) has already been investigated by other methods. We use the same focus objective that focuses the laser to the cornea sample. This is done to collect the plasma spark signal to get a precise measurement. At the same time it records the intensity of the second harmonic signals with another confocal objective. It is also more effective and more precise to collect the signal of the plasma spark in this way. By checking the oscilloscope it is easy to determine the threshold for a single laser shot. Figure 4.9 shows that typical signals come from second harmonic signals and plasma sparks. They are synchronized with the laser pulse. From the top to the bottom the first signal in the screen of the oscilloscope in Figure 4.9 is the signal; it comes from the pockell´s cell inside the laser systems and indicates one single laser pulse. The second signal in the screen of the oscilloscope in Figure 4.9 shows that the signal comes from the second harmonic generation in the collagen in cornea stroma. The third signal in the screen of the oscilloscope in Figure 4.9 shows that the signal comes from the plasma spark.

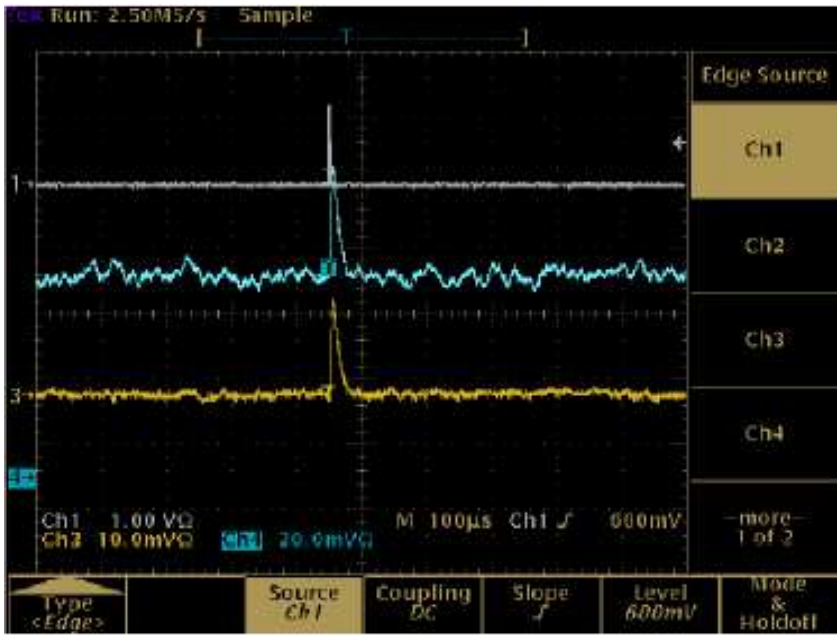

Figure 4.9: This shows that the monitoring of signals from the second harmonic generation also shows that plasma sparks can be measured at the same time with a single oscilloscope.

Figure 4.10 shows the threshold situation. The signal from the plasma spark comes and is the criterion for the threshold. The meaning of the signals in the screen of the oscilloscope is the same as in the figure 4.9.

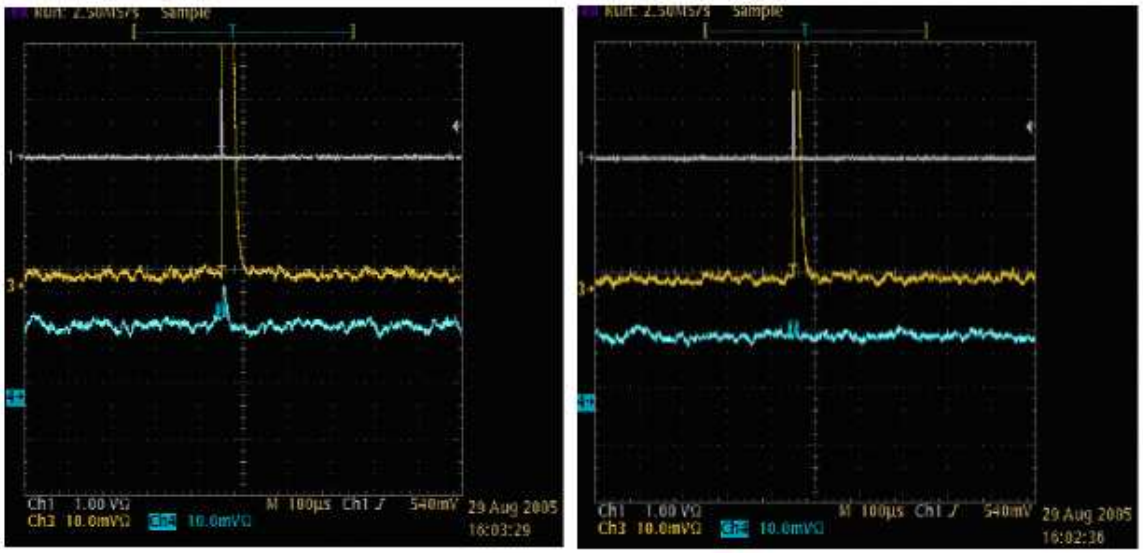

Figure 4.10: Determining the threshold by the plasma spark signal.

While monitoring the signal of the plasma spark in the oscilloscope, the intensity of the second harmonic signal, which comes from the cornea stroma, is recorded by the 16bit stereo-mode supported sound card in a computer. At each power value, signals are recorded for five seconds at a sampling frequency of 44000Hz. Figure 4.11 shows a typical structure of this signal.

When the plasma spark appears it means that the laser-induced optical breakdown (LIOB) is occurring. The tissue in the focus point is ablated and because of this it losses the ability to generate the second harmonic generation (SHG) signals, this causes the intensity of the SHG to decrease. Figure 4.12 clearly shows this phenomenon. The power is recorded by the power meter. Since the only point of concern is the decreasing point of the intensity of SHG, there is no transformation from power to energy needed here. The threshold is the point at 22 mW of power. Figure 4.11 shows the change of the SHG signal as one increases the power of the focus laser

beam. Figure 4.13 shows the change of the plasma signal as one increases the power of the focus laser beam. In Figure 4.14 these two graphs are combined and one can see the tendency at the threshold is very clear: when the plasma increases, the second harmonic signal decreases. By combining the appearance of the plasma spark and the decrease of the second harmonic signals, one can precisly determine the threshold of the corneal stroma.

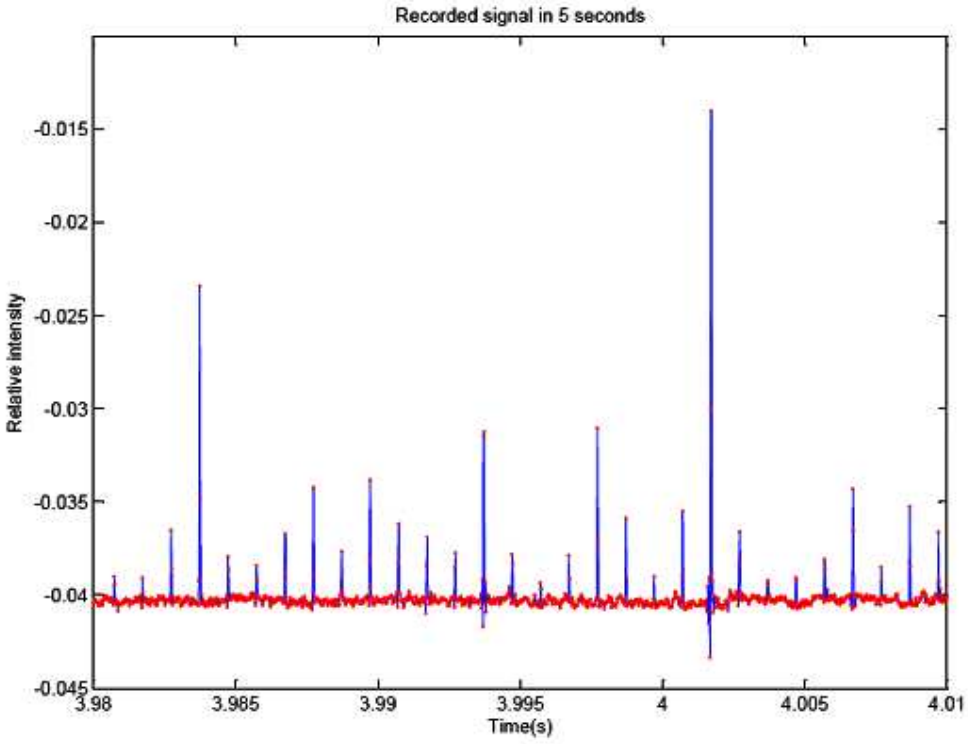

Figure 4.11: SHG intensity is recorded by computer on a sound card.

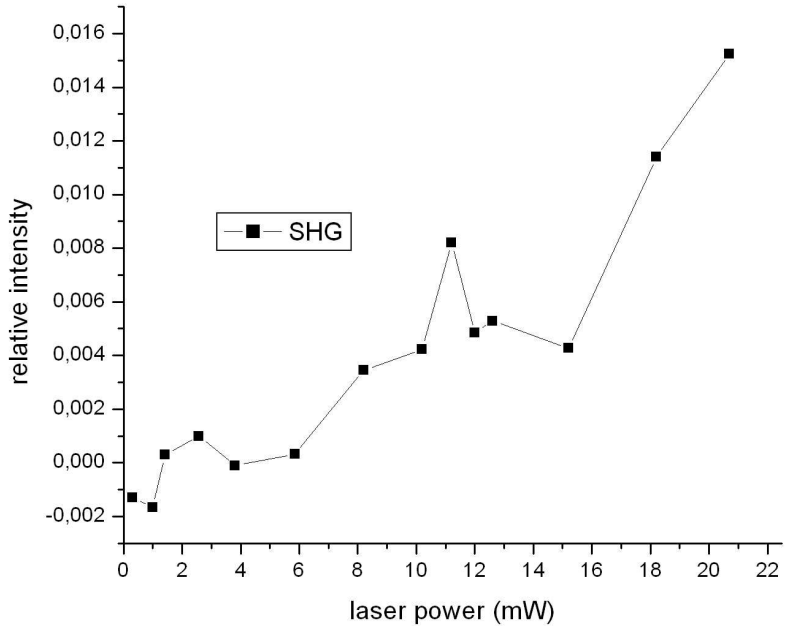

Figure 4.12: SHG intensity decrease at the threshold.

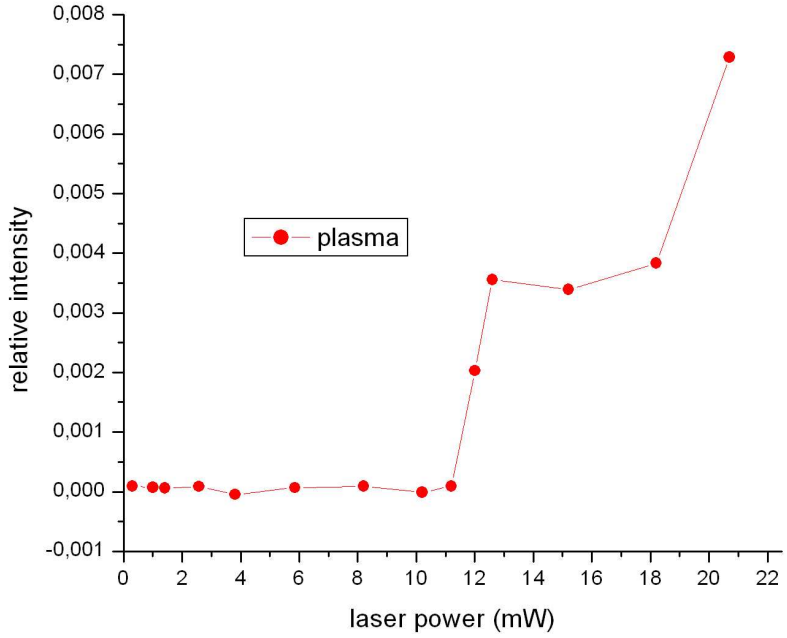

Figure 4.13: Plasma intensity increase at the threshold.

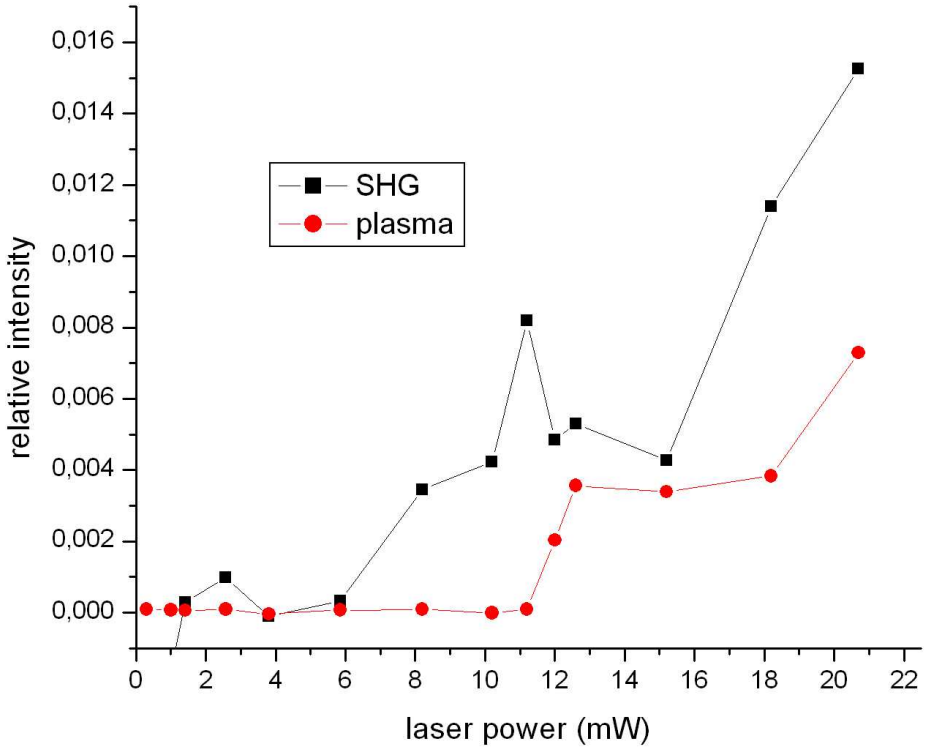

Figure 4.14: The different tendency of plasma and SHG at the threshold.

By ablating the same cornea with different lasers and different pulse widths, the laser ablation threshold dependence on laser pulse width, may be systematically studied. In several experiments, a square-root dependence of the laser fluence at the threshold of LIOB on the pulse duration, is observed [91][92][93]. According to our results the ablation threshold is proportional to the square root of the laser pulse width for 20 picoseconds and a few picoseconds pulse width. As an example the threshold is 4.8 J/cm^2 for 20 picoseconds and 1.57 J/cm^2 for 2.86 picoseconds. This is consistent with previous studies. The ablation threshold is 0.73 J/cm2 for 800 femtoseconds, and 1.15 J/cm2 for 1.63 picoseconds. These values are a little lower than the square root of the laser pulse width. The reason is because for a shorter pulse, a multi-photon phenomena becomes significant. Due to the inhomogenity of the cornea, the variance of the data depends on the

difference between corneas. Some corneas show large differences for the thresholds in different places. It is then necessary for real eye femtosecond laser surgery to use more ablation energy than threshold energy. From Figure 4.15 it is obvious that the shorter laser pulse width introduces the lower threshold. Due to the technical difficulty in the construction of shorter pulse femtosecond laser systems and the fact that, previous research proved with very short laser pulse widths the threshold increases again [94] [95], the few hundred femtoseconds laser is best qualified for eye surgery.

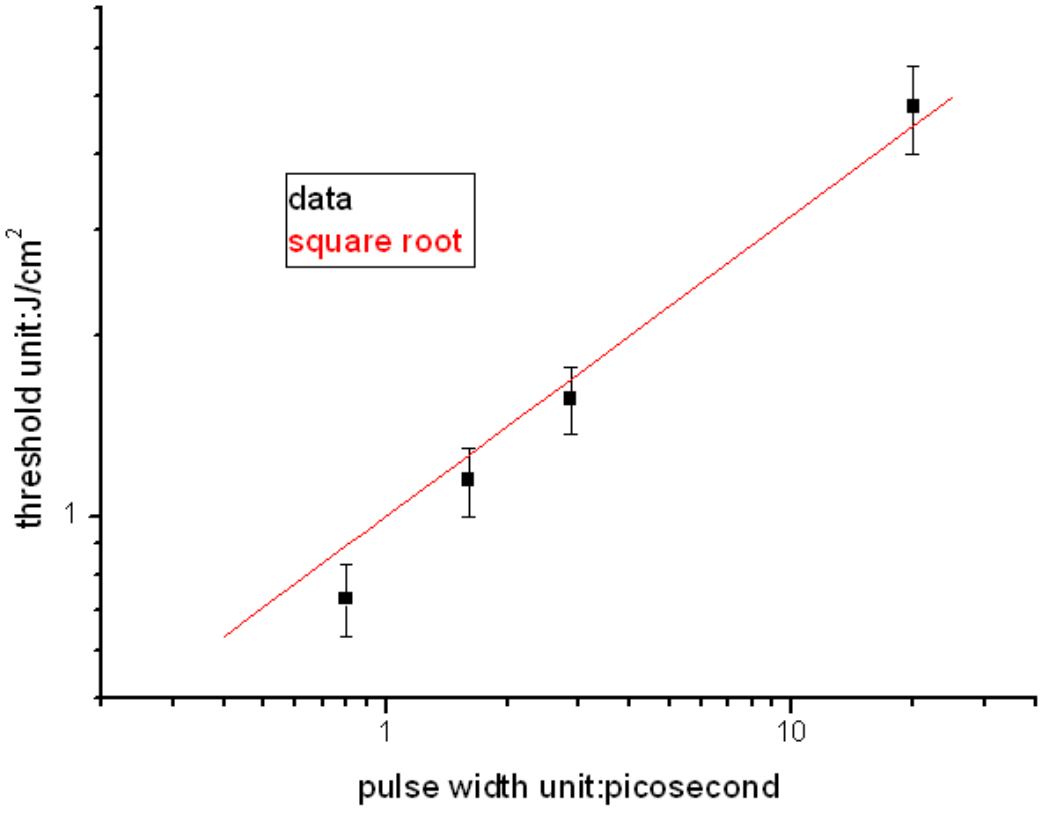

Figure 4.15: The threshold of LIOB as a function of laser pulse width inside the porcine cornea stroma. The solid line represents the square root law.

Because the SHG signal is intrinsic to the collagen, recording the SHG signal makes it possible to focus the input laser beam into the cornea stroma. The depth of the focal laser inside the stroma can be achieved through the computer controlled motorized translation stage. The LIOB threshold using femtosecond laser intrastromal ablation is systematically investigated through the different depths inside the stroma with a series of pulse widths. The dependence of the corneal ablation threshold on the depth of the stroma is not significant in the first 200 μm inside the stroma. Figure 4.16 shows the data for a pulse width of 1.6 picoseconds.

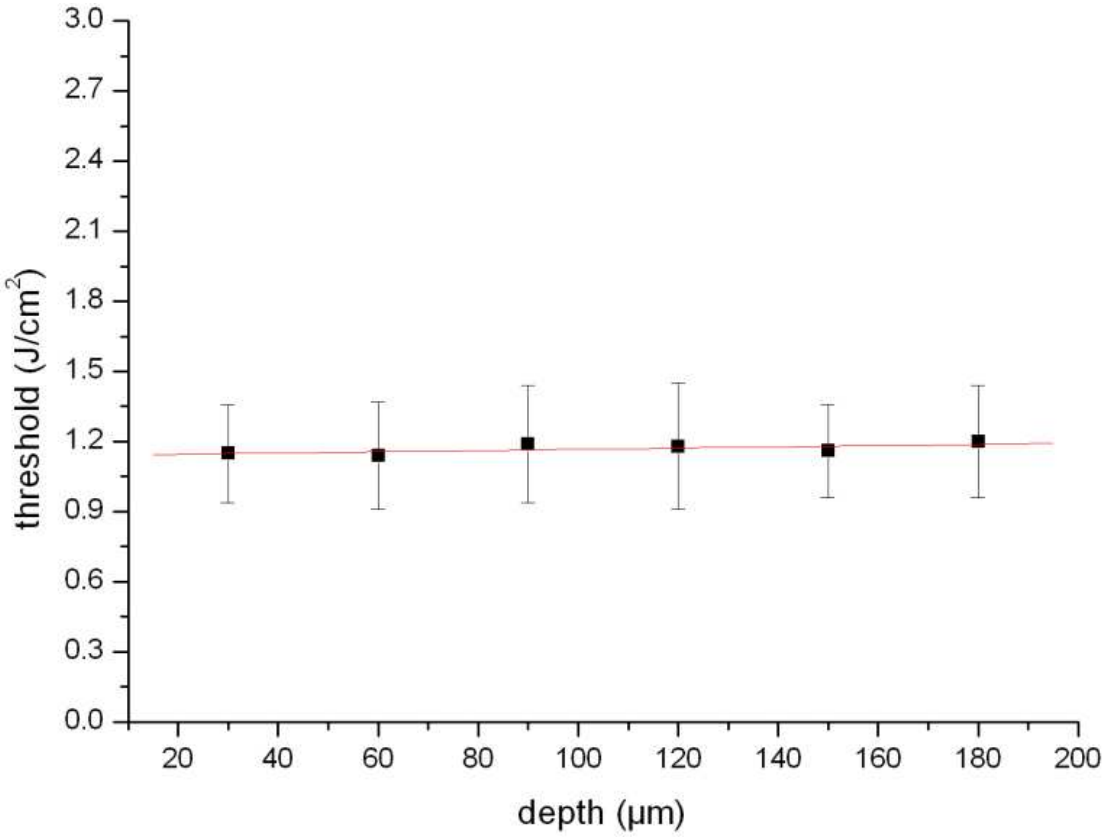

Figure 4.16: The dependence of the threshold of LIOB on the depth of the cornea stroma. The pulse width is 1.6 picoseconds.

Table 4.2 gives the data from 20 picoseconds. From the front surface of the cornea five data were recorded at different depths inside the stroma. First a small amount of energy, which is below the threshold, is used to focus the laser beam inside the cornea storma. The cornea was moved from behind the position of the focal point to the focal point and at the same time the signal from the cornea was monitored by the oscilloscope. When the laser beam was focused on the cornea stroma, there was the signal from the second harmonic generation. Then the laser beam was focused on the surface of the cornea stroma since the second harmonic signal only came from the stroma itself. Using the computer controlled motorized translation stage one can input the laser beam into a few hundred micron meters below the stroma surface. Then the threshold was measured. After this the laser beam was moved into a different depth below the stroma surface and then the threshold was measured again. One typical experiment result is shown in Table 4.2.

Table 4.2 Threshold as a function of depth in stroma for 20 picoseconds laser pulse.

Depth in stroma from surface(μm)	Threshold (J/cm^2)
0	4.12
40	4.43
80	4.30
100	4.19
140	4.52

This study confirmed that the plasma-mediated ablation in the cornea is a function of laser pulse width. Namely the plasma sparks and the second harmonic generation signals were detected at the same time. The ablation threshold is proportional to the square root of the laser pulse width, which is consistent with previous studies. The variance of the data depends on the difference between the corneas. Some corneas display large differences in the threshold measurements. It is necessary for real eye femtosecond laser surgery to use more ablation energy than the threshold.

Due to the real difficulty in construction of shorter pulse width femtosecond laser systems and the fact that, as former research proved, with very short laser pulses the threshold increases again, a few hundred femtosecond laser is the best for eye surgery. A reliable and accurate method to determine the ablation threshold in the different depths of the corneal stroma was proposed. Based on experimental findings, an 800 femtosecond laser pulse is optimal for intra-stromal corneal surgery due to minimized thermal and nonlinear effects. Within the typical flap cutting depth (150 – 200 μm) for microkeratom-free LASIK, the corneal ablation threshold is nearly independent of the corneal depth.

4.3 Ultra fast laser and microscope systems

4.3.1 Experiment set up

From the 1970s a lot of research focused on the laser tissue interaction. The threshold was the basic topic of this field. Ham et al. [96] introduced the first subnanosecond scientific report on injury to the retina. There were three histologic section photographs along with brief explanations of the injury. The threshold was determined as ED50 as the criterion. The ED50 (effective dose 50) is the amount of material required to produce a specified effect in 50% of an animal population. Three of the same authors gave more detail and better descriptions than their original paper in Science [97]. The criterion for determining when damage had occurred, was namely the appearance of an ophthalmscopically visible lesion at the exposure site after irradiation. Electron and light microscopy photographs were presented along with a detailed description of each of this in this paper. Further progress was made by Cain et al. in ascertaining the ED50 pulsed at 530 nm [98]. A unique aspect of this report was the use of both visible lesions and fluorescein angiography (FA) techniques to determine the thresholds. Visible observation was found to be demonstrably more sensitive then FA.

Visible observation of the lesions to determine the threshold was used. Figure 4.17 shows the construction of the ultrafast laser and microscope system. The Nd:Glass femtosecond laser and Nd:YAG picosecond laser were integrated with the microscope. Through a thin film polarizer the two laser beams were integrated together and were put into the microscope. Adding a mirror holder inside the microscope introduced the laser beam into the tissue. By moving the translation stage, which holds the tissue it could burn the tissue with the laser. Removing the mirror holder for the laser and using the eyepiece one can observe the effect of the irradiation. Although the focal point for laser and visible light has little difference, one can still see the lesions with the eyepiece. A little adjustment of the tissue position will give a perfect visible observation of the

lesions.

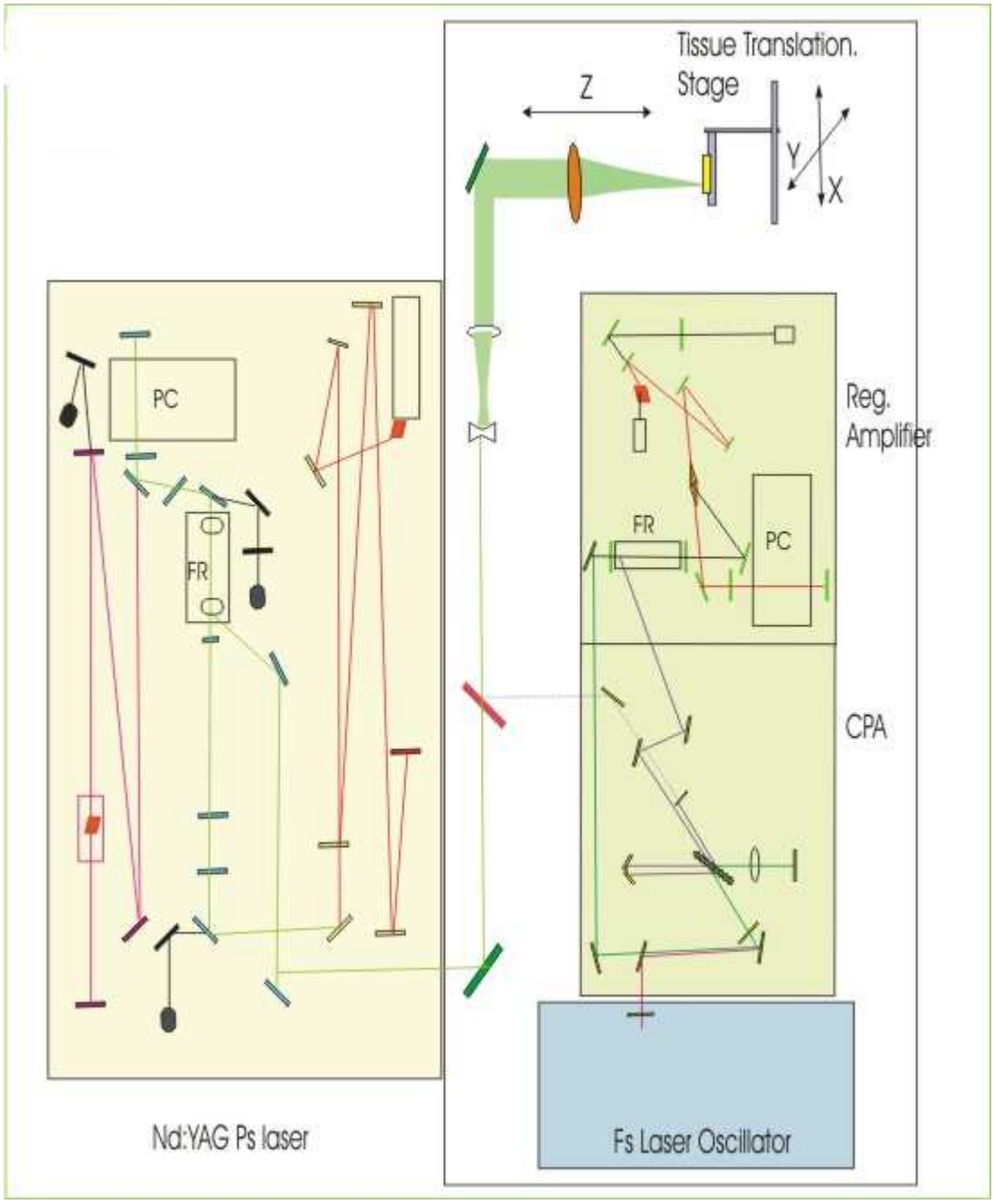

Figure 4.17: Ultra fast laser and microscope system.

4.3.2 Experiment results

By controling the speed of the tissue one can make certain tissue appear in the field of vision of the eyepiece. When half of the ablation bubbles appear then that is ED 50 and one can measure the laser power after the objective, which focuses the laser beam into the cornea. With the help of the eyepiece one can precisely focus the laser beam inside the cornea. Changing the position of the tissue translation stage one can measure the threshold change inside the cornea stroma. Our Nd:Glass femtosecond laser is a CPA system. By changing the distance between the retro reflector and the grating one can easily change the pulse width from 1.6 picooseconds to 5 picoseconds as shown in Figure 4.4. A series of laser pulse widths were studied for the threshold in different depths within the cornea stroma. Table 4.3 shows the threshold change with laser pulse width.

Table 4.3 Threshold as a function of laser pulse width determined by visible observation.

Laser pulse width (ps)	0.8	1.7	3	20
Threshold (J/cm^2)	0.7	1.32	1.77	5.54

Figure 4.18 shows the threshold as function of depth inside cornea stroma for laser pulse width at 1.7 picoseconds. The data is obtained by visible observation.

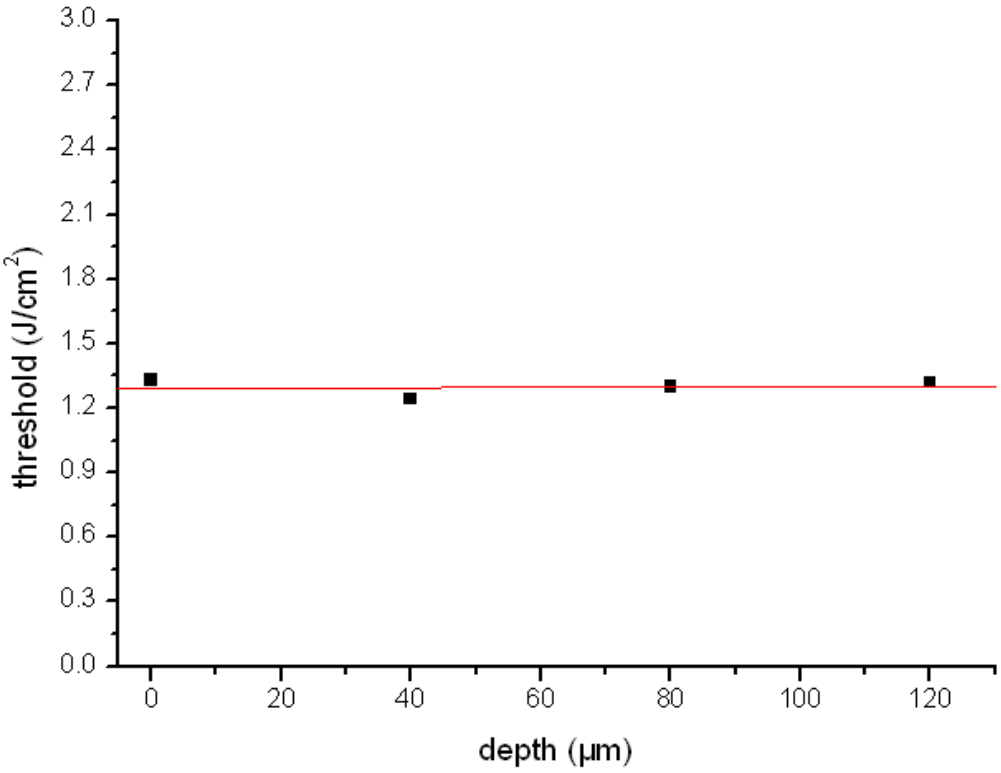

Figure 4.18: The dependence of the threshold of LIOB on the depth of the cornea stroma. The pulse width is 1.7 picoseconds. The data is obtained by visible observation.

4.4 Second harmonic generation imaging of corneal stroma

In the 1990s a new idea for the microscope came from a light source [99]. ultra fast lasers took the place of a normal light sources. The novel two-photon laser scanning fluorescence microscope appears to be a powerful tool in cell biology and tissue physiology [100]. Microscope imaging is obtained from nonlinear optical processes induced by the ultra high photo flux, for example, multi-photon absorption, multi-harmonic generation, four-wave mixing, and coherent Roman scattering [101]. The two-photon microscope has advantages when compared with the traditional optical microscope. The first advantage is that the two-photon microscope does not need an extra pinhole to get diffraction limited resolution and depth discrimination. The second advantage is that the two-photon microscope greatly reduces photo damage or bleaching effect outside the laser focus.

The Zeiss LSM 510 NLO laser scanning multi-photon microscope (Zeiss, Jena, Germany) was used to observe the LIOB effect in cornea stroma by SHG signals from cornea stroma. The SHG imaging experiment setup is illustrated in Figure 4.19. A Ti:sapphire femtoseond laser (Coherent Inc, Santa Clara, USA) is the excitation laser source. An advantage of this laser source is the wavelength tunable from 700 to 1000 nm. The Ti:sapphire emission wavelength was set to 880 nm in our research. The laser intensity was attenuated using an acoustic optic madulator (AOM Zeiss). A 40 $\times$ 0.8 NA water immersion objective was employed for high resolution imaging of the sample. The signal of SHG coherent generating from collagen emits predominantly in the transmission direction [102]. Therefore, a 63 $\times$ 1.4 NA oil immersion objective was employed to efficiently gather SHG signals. Band pass filter (440/10nm) and infrared beam block filters were used to ensure the PMT in transmission direction just recorded the SHG signals from the cornea.

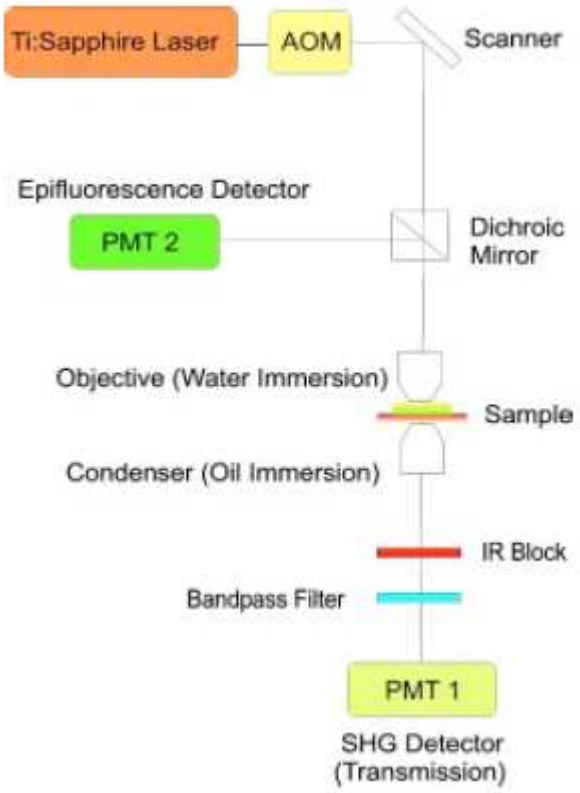

Figure 4.19: Conceptual drawing of SHG imaging experiment.

In the intrastromal ablation procedure the plasma mediated ablation effect ionises the tissue in the focal point. The plasma exits in cornea via diffusion leaving a bubble there. Such bubbles inside the stroma cannot maintain the original shape. When collapse happens the cornea curvature is influenced directly. The multi-photon microscope was used to evaluate the ablation stroma [[103]]. Then the bubble shape introduced by LIOB was most interesting. The typical case is the intrastromal ablation by a single laser pulse. The effect of single laser pulse ablation is illustrated in Figure 4.20. The two-photon microscope gives us a clear concept of the laser tissue interaction effects. When the laser pulse energy is set to about two times above the threshold; then the laser induced cavitation bubble can be recognized very well. The collagen fibers reaction after bubble formation is very clearly seen. From where the red arrows are, the collagen fibers in the edge of the bubble were not coagulated or damaged by the laser pulse, which often happens in laser

thermal ablation. The collagen surrounding the bubble is nearly untouched indicating very small side effects. This smooth edge is good for laser surgery. Furthermore, the reduction of thermal damage minimizes the possibility of side effects in laser surgery, and is beneficial for the wound-healing process.

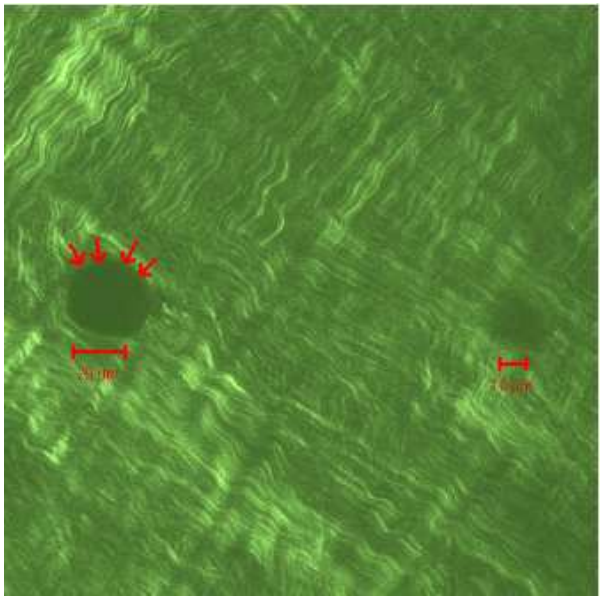

Figure 4.20a: Single laser pulse induced ablation bubble.

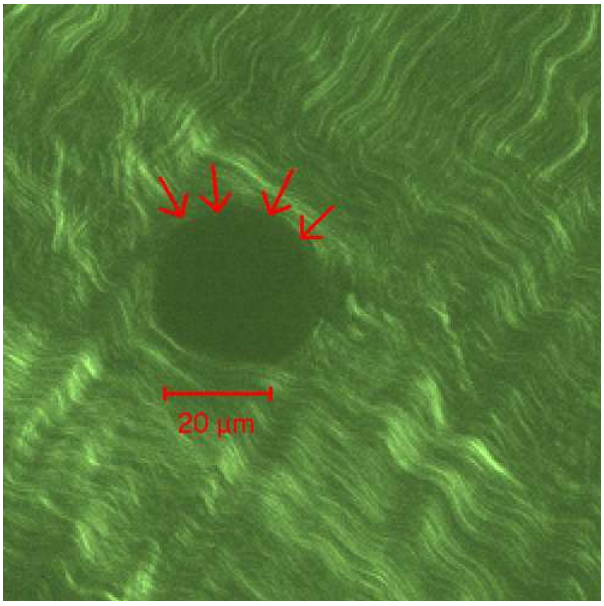

Figure 4.20b: A single laser pulse induced ablation bubble.

A three-dimensional stack imaging of a cornea structure modified by ultra fast laser pulse gives the same conclusion. As shown from any side of the bubble in the Figure 4.21, the pictures shown here give nearly the same outcome. From the XY cross section of the bubble in Figure 4.21, one can see that the bubble is like an ellipse in space, and in Z direction the border of the bubble is also very clear and smooth. No further expansion of the bubble makes it possible to control the ablation depth of femtosecond laser precisely in Z direction.

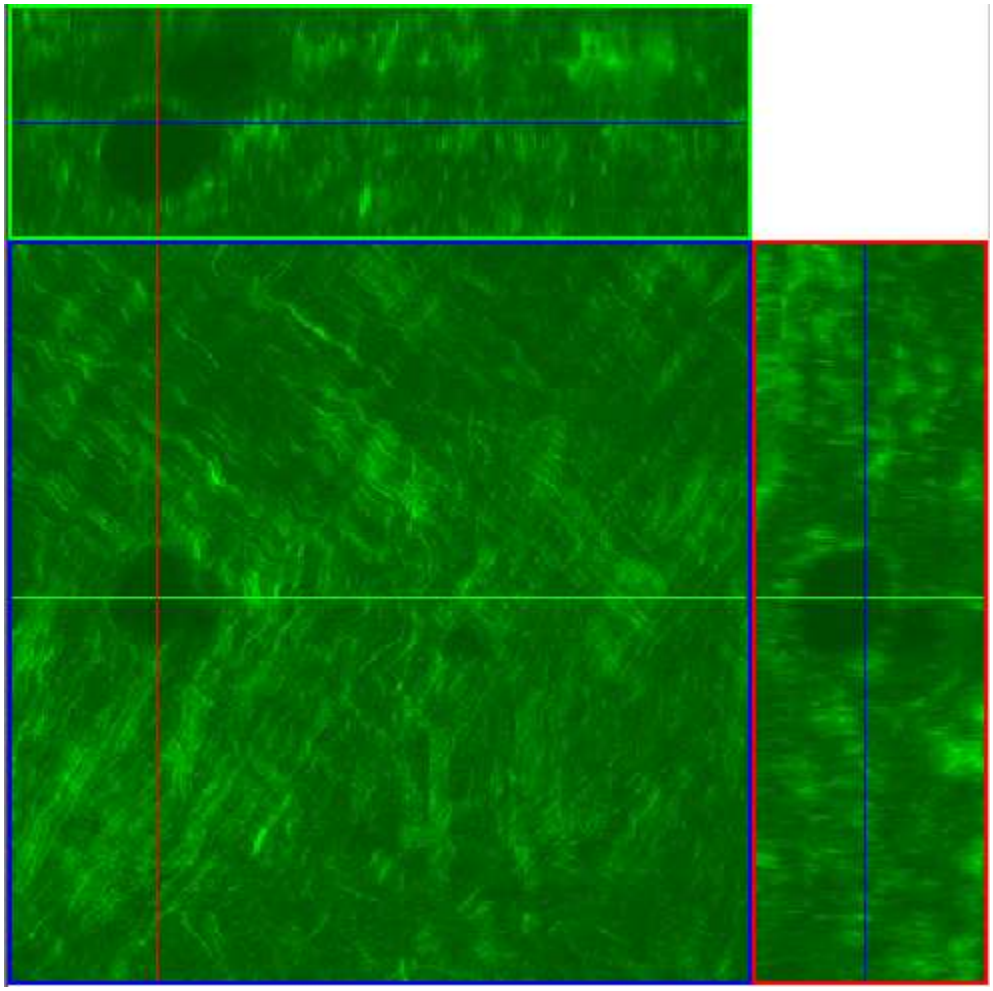

Figure 4.21: Three-dimensional stack imaging of ablation bubbles.

For a single bubble one can get a perfect result but for many bubbles the result is not ideal. The sizes of the different bubbles change over quite a wide range. As can be seen from Figure 4.20, the bubble size in the left is about 20 micro meters in diameter while the bubble size in the right is about 10 micro meters in diameter. The laser pulse signals shown by the oscilloscope are constant so that the laser pulse is stable. From the different laser systems one can get the same structure as shown in Figure 4.20. The best possible reason then comes from the inhomogeneity of cornea stroma itself.

4.5 Spot split grating

The inhomogeneity of cornea stroma introduces the irregular distribution of the ablation bubble size. The uncontrollable difference of ablation bubble size will lead to unexpected curvature of the cornea for the intrastromal refractive surgery. One idea for resolving this problem is to overlap part of the ablation bubbles. One possible method is to divide the input laser beam and let separate beams parallel very near so that the ablation bubbles introduced by them will mix together and give one uniform big bubble.

Damman-grating is employed for this purpose. This element works with homogenous illumination. It works best with collimated beams but also with divergent or convergent beams. The wavefront is modulated by the phase pattern through the element. Two or three beams emerge behind the element by constructive and destructive interference, each consists of the incident angular spectrum. These are shifted by theta according to sin(angle)=wavelength / period length of the phase-pattern. Such spot split grating was put on the laser beam path after the beam expander. By changeing the angle of the grating to the beam path and the distance between the separate lasers beams also changes. This results in the distribution of the ablation bubble size. To put the grating on the right angle introduces a uniform ablation bubble in the cornea stroma as illustrated in Figure 4.22 and Figure 4.23.

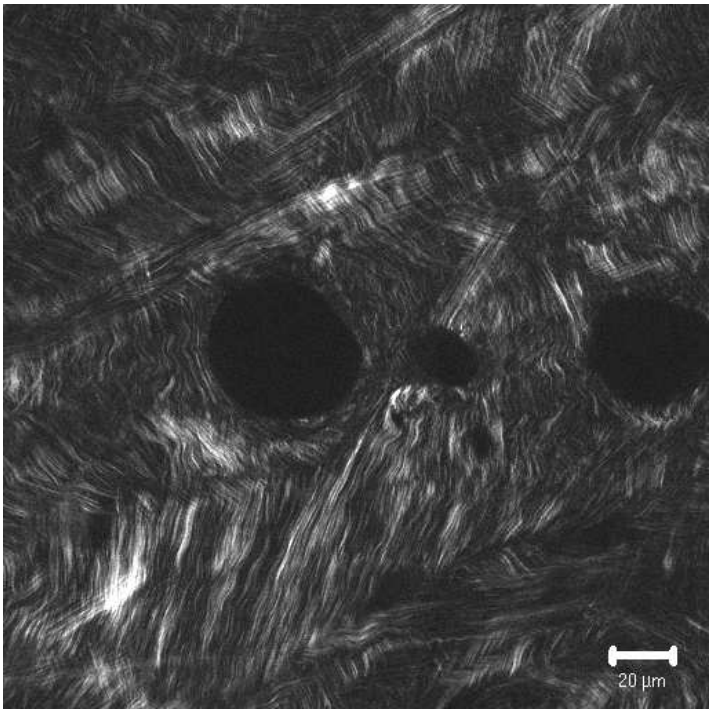

Figure 4.22: The inhomogeneity of cornea stroma introduces the irregular distribution of the ablation bubble size.

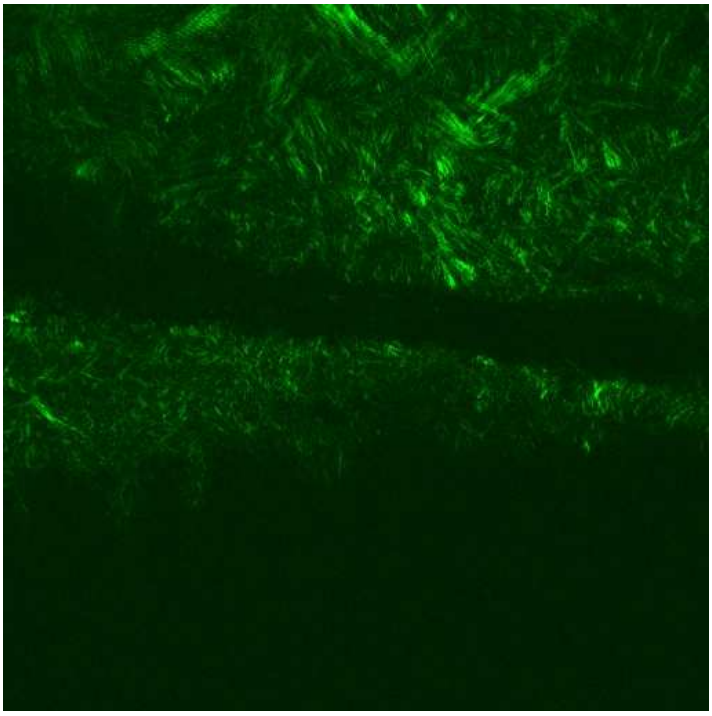

Figure 4.23: More uniform bubble size with the spot split grating introduced.

Chapter 5 Dissertation Conclusions

Diode pumped all-solid-state ultrafast lasers are promising for mini-invasive refractive surgery and keratoplasty. A funda mental systematical study concerning ultrafast laser tissue interactions is crucial before applying the state of the art laser technology to ophthalmic applications.

Porcine cornea samples were treated with three diode pumped all-solid-state ultrafast lasers, namely, a Nd:glass femtosecond laser, a Yb:KYW femtosecond laser, and a Nd:YAG picosecond laser. The pulse width of the ultrafast laser pulses ranges from 800 fs to 20 ps. The corneal ablation threshold as a function of the laser pulse width and the depth in the corneal stroma was precisely determined by simultaneous monitoring of the intensity of the laser-induced plasma and the second harmonic signals coming from the cornea stroma.

This study confirmed in a new way that the plasma mediated ablation in the cornea is a function of laser pulse width. Namely the plasma spark and the second harmonic generation signal were detected at the same time. The ablation threshold is proportional to the square root of the laser pulse width, which is consistent with previous studies. The dependence of the corneal ablation threshold on the depth of the stroma is not significant in the first 200 μm. One can determine the LIOB threshold by observing the ablation bubble. One also can determine the LIOB threshold by observing the plasma spark. These two methods have the same sensitivity level.

Acknowledgements

It is my pleasure to work in the research group of Prof. Bille. I would like to give my sincere thankfulness to Prof. Bille, my supervisor, for his many suggestions, critical insights, and constant support during this research. Prof. Bille gives me a very good example of how a scientist should be and this impression will give me a lot of benefit in my research career. Prof. Bille provided an ideal environment for me to do research, and to discuss with scientists who come from the whole world during the international conference.

I am very indebted to Dr. Meng Han for his guidance through the whole time. He is a really good scientist and I learned a lot from the discussion with him. It is a pleasure to work with him and learn from him how to do the research.

I want to thank my colleagues, Mikael Agopov and Olivier La Schiazza. They gave me plenty of generous help in this job. I do not just thank them for the work but also for the good time in the bar in Inter Harbour, Baltimore, USA.

I want to thank my colleagues, Dr. Nina Korablinova, Dr. Leander Zickler, Dr. Thomas Nirmaier, Dr. Klaus Greger, Hong Guo, Yanyan Wang, Matthias Walter, Gopal Pudasaini, Cristina Alvarez Diez, Sarah Snyder, Feng Shao, Yu Jiayi, Yifei Liu, Yuansen Chen, Wei Jiang and Hongwei Zhang of the Prof. Bille group. They created a friendly, stimulanting atmosphere and always nice cooperation.

I lost my heart in Heidelberg because I fell in love with my girlfriend Yang Xinxin here. She is a part of my life in Germany and will be forever.

The last ones I want to thank are my parents and friends, who always support me in my studies, and share my happiness and sadness.

List of Figures

List of tables

Publication List

1, “Mini-invasive corneal surgery and imaging with femtosecond lasers”

M. Han, G. Giese, L. Zickler, **H. Sun**, and J. F. Bille., Optic Express, 12, 4275-4281(2004).

2, “Confocal and two-photon excited autofluorescence imaging of human retinal pigment epithelial cells”

Meng Han, AlmutBindewald-Wittich, Frank Holz, Sarah Snyder, GuenterGiese, **Hui Sun**, Olivier La Schiazz, Michael Agopov, Markolf H. Niemz, and Josef F.Bille

Journal of Biomedical Optics, Vol. 11, 010501 (Feb. 10, 2006)

3, “Second harmonic generation microscopy imaging of cornea after femtosecond laser intrastromal ablation”

Wang yanyan, Han meng, **Sun hui**, Josef Bille, and Ren qiushi

Acta Laser Biology Sinica, Vol 14, No.5, 321-326 (2005)

4, “Ultrafast all solid state lasers for mini-invasive eye surgery” poster

Hui Sun, Meng Han, L.Zickler, G.Giese and J.F.Bille

Association for Research in Vision and Ophthalmology conference 2004

April 25—29, 2004, Fort Lauderdale Florida, The United States

5, “Femtosecond lasers for mini-invasive refractive surgery and non-invasive ocular tissue imaging” poster

Hui Sun, Meng Han, L.Zickler, G.Giese and J.F.Bille

the 8th Corneal Conference

July 8—9, 2004, Cardiff, the United Kingdom

6, “Ultrafast all solid state lasers for non-invasive ocular tissue imaging” poster

M. Han, L. Zickler, **H. Sun**, G. Giese and J. F. Bille

Imaging in the eye II: Technologies and Clinical Applications

May 26,2004, The Institute of Physics, 76 Portland Place, London, the United Kingdom

7, “Femtosecond laser ablation threshold dependence on corneal depth and laser pulse width” poster

Hui Sun, Meng Han, Mikael Agopov, Feng Shao, Yifei Liu, G. Giese , Markolf H. Niemz, and J.Bille

Association for Research in Vision and Ophthalmology conference 2006

April 29----May 4, 2006, Fort Lauderdale Florida, The United States

8, “Femtosecond laser ablation threshold dependence on corneal depth and laser pulse width”

Hui Sun, Meng Han, Markolf H. Niemz, and J.Bille

paper in preparation

References

[1] "New Frontiers in Vision and Aberration-Free Refractive Surgery," edited by J.F. Bille, C.F.H Harner, F. Loesel, Springer Press, Heidelberg, Germany, 2002.

[2] T. Juhasz, F.H. Loesel, C. Horvath, R.M. Kurtz, G. Mourou, "Corneal Refractive Surgery with Femtosecond Lasers," IEEE J. Sel. Top. Quantum Electron. 5, 902-910, 1999.

[3] F.H. Loesel, M.H. Niemz, J.F. Bille and T. Juhasz, "Laser-Induced Optical Breakdown on Hard and Soft Tissues and Its Dependence on the Pulse Duration: Experiment and Model,"IEEE J. Quantum Electron. 32, 1717-1722, 1996.

[4] L.Zickler, M. Han, G. Giese, F. H. Loesel, and J. F. Bille., "Femtosecond All-Solid- State Laser for Refractive Surgery", Proceedings of The International Society for Optical Engineering (SPIE), San Jose, 4978, 94-207, 2003.

[5] U.Morgner, F.X.Kärtner, S.H.Cho, Y.Chen, H.A.Haus, J.G.Fujimoto, E.P.Ippen, V.Scheuer, G.Angelow, and T.Tschudi. "Sub-Two-cycle pulses from a kerr-lens mode-locked Ti:Sapphire laser" Optics Letters, 24 (6): 411-13, 1999.

[6] Anthony E. Siegman "LASERS" University Science Books Mill Valley, California

[7] E.B.Treacy, "Optical pulse compression with diffraction gratings" IEEE J.Quantum Electron, QE—5,454—460, 1969.

[8] F.J.Duarte and J.A.Piper "dispersion theory of multiple prisms beam expanders for pulsed dye lasers" Optics Comm.43: 303—307, 1982.

[9] R.L.Fork, O.E.Martinez, and J.P.Gordon "negative dispersion using pairs of prisms" Vol.9,No.5 / May 1984/OPTICS LETTERS 150

[10] E.B.Treacy, “Optical pulse compression with diffraction gratings” IEEE J.Quantum Electron, QE—5,454—460, 1969.

[11] C.Froehly, B.Colombeau, and M.Vampouille “shaping and analysis of picosecond light pulses” in Progress of Modern Optics, Vol.XX:115—125, 1981.

[12] O.E.Martinez “grating and prism compressor in the case of finite beam size” J.Opt.Soc.Am.B, 3:929—934,1986.

[13] M.Born and E.Wolf “Principles of Optics----electromagnetic theory of propagation, interference and diffraction of light” Pergamon Press, Oxford, New York, 1980.

[14] O.E.Martinez, J.P.Gordon, and R.L.Fork “negative group velocity dispersion using diffraction” J.Opt.Soc.Am .A1:1003—1006, 1984.

[15] F.J.Duarte “generalized multiple prism dispersion theory for pulse compression in ultrafast dye lasers” Opt. And Quant. Electr., 19:223—229, 1987.

[16] V.Petrov, F.Noack, W.Rudolph, and C.Rempel “intracavity dispersion compensation and extracavity pulse compression using pairs of prisms” Exp. Technik der Physik, 36:167—173, 1988.

[17] C.P.J.Barty, C.L.GordoⅢ, and B.E.Lemoff “Multiterawatt 30 fs Ti:sapphire laser system” Optics Lett., 19:1442----1444, 1994.

[18] P.F.Curley, Ch.Spielmann, T.Brabec, F.Krausz, E.Wintner, and A.J.Sxhmidt, “Operation of a fs Ti:sapphire solitary laser in the vicinity of zero group delay dispersion”Opt.Lett., 18:54—57, 1993.

[19] M.T.Asaki, C.P.Huang, D.Garvey, J.Zhou, H.Kapteyn, and M.M.Murnane “generation of 11 fs pulses from a self mode locked Ti:sapphire laser” Opt.Lett., 18:977—979,1993.

[20] E.B.Treacy. “Optical pulse compression with diffraction gratings”. IEEE J.Quantum Electron.QE-5 :454-460, 1969.

[21] J.Desbois, F.Gires, and P.Tournois. “A new approach to picosecond laser pulse analysis and shaping”. IEEE J.Quantum Electron., QE-9: 213-218, 1973.

[22] M.A.Duguay and J.W.Hansen. “Compression of pulses from a mode-locked He-Ne laser”. Appl.Phys.Lett., 14:14-15, 1969.

[23] J.Heppner and J.Kuhl. “Intra cavity chirp compensation in a colliding pulse mode-locked laser using thin-film interferometers”. Appl.Phys.Lett., 47:453-455, 1985.

[24] J.Kuhl and J.Heppner. “Compression of fs optical pulses with dielectric multi-layer interferometers”. IEEE J.Quantum Electron., QE-22:182-185, 1986.

[25] David N. Fittinghoff, Barry C. Walker, Jeff A. Squier, Csaba. S Toth, Christoph Rose Petruck, and Christopher P. J. Barty “Dispersion Considerations in Ultrafast CPA Systems” IEEE JOURNAL OF SELECTED TOPICS IN QUANTUM ELECTRONICS. VOL.4, NO.2, MARCH/APRIL 1998.

[26] Jean-Claude Diels, Wolfgang Rudolph “ Ultrashort Laser Pulse Phenomena” OPTICS AND PHOTONICS

[27] G.H.C.New “mode locking of quasi continuous lasers” Optics Comm. 6:188—193, 1972.

[28] G.H.C.New “pulse evolution in mode locked quasi continuous lasers” IEEE J.of Quantum Electron., QE-10:115—124, 1974.

[29] S.V.Chekalin, P.G.Kryukov, Yu.A.Matveetz, and O.B.Shatherashvili “the processes of formation of ultrashort laser pulses” Opto Electronics, 6:249—261, 1971.

[30] H.W.Kogelnik and T.Li, “laser beams and resonators”, Appl.Opt., 5:1550----1567, 1966.

[31] A.Agnesi and G.C.Reali, “analysis of unidirectional operation of Kerr lens mode locked ring oscillators.”, Optics Comm., 110:109----114, 1994.

[32] J. Liang, B. Grimm, S. Goelz, andJ. F. Bille, “Objective measurement of wave aberrations of the human eye with the use of a hartmann-shack wave-front sensor,” J. Opt. Soc. Am. A 11, pp. 1949–57, 1994.

[33] L. Zickler, ‘‘Femtosecond laser for highly precise ophthalmic surgery and novel imaging method of corneal ultrastructure modifications,’’ PhD dissertation, University of Heidelberg, 2003.

[34] G. Mourou, “The ultrahigh-peak-power laser: Present and future,” Applied Physics B (Lasers and Optics) B65(2), 205–211, 1997.

[35] D.Stricland, G.Mourou, “Compression of amplified chirped optical pulses”, Opt.Commun. 56, 219-221, 1985.

[36] M.H. Niemz1, A. Kasenbacher, M. Strassl, A. Backer, A. Beyertt, D. Nickel, and A. Giesen, “Tooth ablation using a CPA-free thin disk femtosecond laser system” Appl. Phys. B, 2004.

[37] Otori T. “Electrolyte content of rabbit corneal stroma”. Exp Eye Res 6: 356-367, 1967.

[38] Kern P, Menasche M, and Robert L. “Relative rates of biosynthesis of collagen type Ⅰ, type Ⅴ and type Ⅵ in calf cornea”. Biochem J 274: 615-617, 1991.

[39] Komai Y, Ushiki T. “The three-dimensional organization of collagen fibrils in the human cornea and sclera”. Invest Ophthalmol Vis Sci 32: 2244-2258, 1991.

[40] Giraud JP, Pouliquen Y, and Offret G. “Statistical morphometric studies in normal human and rabbit corneal stroma”. Exp Eye Res 21: 221-229, 1975.

[41] Hamada R, Pouliquen Y, and Giranud JP. “Quantitative analysis on the ultrastructure of human fetal cornea.” In Yamada E, Mishima S, editors: The structure of the eye Ⅲ, Tokyo, 1976, Jpn J Ophthalmol, 49-62

[42] Hamada R, Giraud JP, and Graf B. “Etude analytique et statistique des lamellas, des keratocytes, des fibrilles de collagene de la region centrale de la cornee humaine normale | Analytical and statistical study of the lamellae, keratocytes and collagen fibrils of the central region of the normal human cornea. (light and electron microscopy)”. Arch Ophtalmol Rev Gen Ophtalmol 32: 563-570, 1972.

[43] Iozzo RV. “Matrix proteoglycans: from molecular design to cellular function”. Amm Rev Biochem. 67: 609-652, 1998.

[44] Ueda A, Nishida T and Otori T. “Electron-microscopic studies on the presence of gap junctions between corneal fibroblasts in rabbits”. Cell Tissue Res 249: 473-475, 1987.

[45] Markolf H.Niemz “Laser-Tissue Interactions: Fundamentals and Applications” Springer-Verlag Berlin Heidelberg 2004.

[46] Boulnois, J.-L. “Photophysical processes in recent medical laser developments: a review”. Laser Med. Sci. 1, 47-66, 1986.

[47] Parrish J.A and Deutsch T.F, “laser photomedicine”. IEEE J. Qu. Electron. QE-20, 1386-1396, 1984.

[48] Srinivasan R and Mayne-Banton V, “self-developing photoetching of poly (ethylene terephthalate) films by far-ultraviolet excimer laser radiation”. Appl. Phys. Lett. 41, 576-578, 1982.

[49] Teng P, Nishilka N.S, Anderson R.R and Deutsch T.F, “Acoustic studies of the role of immersion in plasma mediated laser ablation”. IEEE J. Qu. Electron. QE-23, 1845-1852, 1987.

[50] Stern D, Schoenlein R.W, Puliafito C.A, Dobi E.T, Birnngruber R and Fujimote J.G, “Corneal ablation by nanosecond, picosend and femtosecond lasers at 532 and 625 nm”. Arch. Ophthalmol. 107, 587-592, 1989.

[51] Niemz M.H, Klancnik E.G and Bille J.F, “Plasma mediated ablation of corneal tissue at 1053 nm using a Nd:YLF oscillator/regenerative amplifier laser”. Lasers Surg. Med. 11, 426-431, 1991.

[52] Puliafito C.A and Steinert R.F, “Short-pulsed Nd:YAG laser microsurgery of the eye: biophycisal considerations”. IEEE J. Qu. Electron. QE-20, 1442-1448, 1984.

[53] Smith D.C and Haught A.F, “Energy loss processes in optical frequency gas breakdown”. Phys. Rev. Lett. 16, 1085-1088, 1966.

[54] Krasnov MM, “Laserpuncture of anterior chamber angle in glaucoma” Am. J. Ophthalmol. 75, 674-678, 1973.

[55] Aron-Rosa D, Aron J, Griesemann J, Thyzel R, “Use of the neodym-YAG laser to open the posterior capsule after lens implant surgery: a preliminary report”. J. Am. Intraocul. Implant Soc. 6, 352-354, 1980.

[56] Fankhauser F, Roussel P, Steffen J, van der Zypen E, Chrenkova A, “Clinical studies on the efficiency of high power laser radiation upon some structures of the anterior segment of the eye”. Int. Ophthalmol. 3, 129-139, 1981.

[57] Niemz M.H, “Investigation and spectral analysis of the plasma-induced ablation mechanism of dental hydroxyapatite”. Appl. Phys. B. 58, 273-281, 1994.

[58] S. Roth and I. Freund, ”Coherent Optical Harmonic Generation in Rat-tail,” Opt. Commun. **33**, 292-296, 1980.

[59] Samuel Roth and Isaac Freund. “Second harmonic generation in collagen”. Journal of ChemicalPhysics, 70((04)):1637–1643, 1979.

[60] E. Fukada. Advanced Biophysics, 6:121, 1974.

[61]D.A. Kleinman, “Second harmonic generation of light”. Physical Review, 128:1761–1775, 1962.

[62] G. Rinker and G. Bohannon, IEEE Trans. Plasma Sci. PS-8, 55, 1980.

[63] E. H. A. Granneman and M. J. van der Wiel, Rev. Sci. Instrum. 46, 332, 1975.

[64] S. M. Sorscher and M. P. Klein, Rev. Sci. Instrum. 51, 98, 1980.

[65] Y. C. Kiang and R. W. Lang, Appl. Opt. 22, 1296, 1983.

[66] J. G. Edwards, W. M. Hubbard, and R. M. Quilliam, J. Phys. E. 10, 699, 1977.

[67] Luciano Bachmann, Denise Maria Zezell, and Edison Puig Maldonado, “Determination of Beam Width and Quality for Pulsed Lasers Using the Knife-Edge Method”, Instrumentation Science & Technology, Vol31, No.1, 47-52, 2003

[68] John M. Khosrofian and Bruce A. Garetz, “Measurement of a Gaussian laser beam diameter through the direct inversion of knife-edge data”, Applied Optics, Vol.22, No.21, 3406-3410, 1983.

[69] A. H. Firester, M. E. Heller and P. Sheng, “Knife-edge scanning measurements of subwavelength focused light beams”, Applied Optics, Vol. 16, No. 7, 1971-1974, 1977.

[70] D. W. Tenquist, R. M. Whittle and J. Yarwood, “University Optics”, LONDON ILIFFE BOOKS, 1970.

[71] Meng Han, Gunter Giese, Leander Zickler, Hui Sun, Josef F. Bille, “Mini-invasive corneal surgery and imaging with femtosecond lasers,” Opt. Express **12**, 4275-4281 2004.

[72] Baogui Wang, Karl-Juergen Halbhuber , Karsten Koenig , “Intrastromal Ablation with Epithelium Intact by Infrared Nanojoule Femtosecond Lasers” Proceeding of SPIE 2005, San Jose.

[73] Nordan LT, Slade SG, Baker RN, Suarez C, Juhasz T, Kurtz R. “Femtosecond laser flap creation for laser in situ keratomileusis: six-month follow-up of initial U.S. clinical series”. J Refract Surg. Jan-Feb;19(1):8-14. 2003.

[74] Meng Han, Leander Zickler, Guenter Giese, Matthias Walte, Frieder H. Loesel, Josef F. Bille, “Secondharmonic imaging of cornea after intrastromal femtosecond laser ablation” Journal of Biomedical Optics 9,760-766, 2004.

[75] Tibor Juhasz, Frieder H. Loesel, Ron M. Kurtz, Christopher Horvath, Josef F. Bille, and Gerard Mourou, “Corneal Refractive Surgery with Femtosecond Lasers,” IEEE Journal of Selected Topics in Quamtum Eelctronics 5, 902-910, 1999.

[76] Kurtz RM, Horvath C, Liu HH, Krueger RR, Juhasz T. “Lamellar refractive surgery with scanned intrastromal picosecond and femtosecond laser pulses in animal eyes.” J Refract Surg. Sep-Oct;14(5):541-548, 1998.

[77] Heisterkamp A, Mamom T, Kermani O, Drommer W, Welling H, Ertmer W, Lubatschowski H. “Intrastromal refractive surgery with ultrashort laser pulses: in vivo study on the rabbit eye.” Graefes Arch Clin Exp Ophthalmol. Jun;241(6):pp511-517, 2003.

[78] F.H. Loesel, M.H. Niemz, J.F. Bille, and T. Juhasz, “Laser-Induced Optical Breakdown on Hard and Soft Tissues and Its Dependence on the Pulse Duration: Experiment and Model,” IEEE J. Quantum Electron 32, 1717-1722, 1996.

[79] R. G. Borland, D. H. Brennan, J. Marshall, and J. P. Viveash, “The role of fluorescein angiography in the detection of laser-induced damage to the retina: A threshold study for Q-switched, neodymium and ruby laser”, Exp. Eye Res., Vol.27, 471-493, 1978.

[80] M.H.Niemz, T.P.Hoppeler, T.Juhasz and J.F.Bille, "Intrastromal ablations for refractive corneal surgery using picosecond infrared laser pulses," Lasers and Light in Ophthalmology **5,** 149-155, 1993.

[81] Ron M. Kurtz, Xinbing Liu, Victor M. Elner, Jeffrey A. Squier, Detao Du, Gerard A. Mourou, "Photodisruption in the Human Cornea as a Function of Laser Pulse Width," Journal of Refractive Surgery **13,** 653-658, 1997.

[82] "Laser-Tissue Interactions: Fundamentals and Applications" Second, Revised Edition edited by M. Niemz, Springer Press, Heidelberg, Germany 2002.

[83] A.Beyertt, D.müller, D.Nickel, and A.Geisen, "Femtosecond thin disk Yb:KYW regenerative amplifier without CPA," OSA Trends in Optics and Photonics **83**, 407, 2003.

[84] C. Horvath, A. Braun, H. Liu, T. Juhasz, and G. Mourou, "Compact directly diode-pumped femtosecond Nd:glass chirped-pulse-amplification laser system", Optics Letters. Vol. 22, No. 23, 1790-1792, 1997.

[85] F. H. Loesel, C. Horvath, F. Grasbon, M. Jost and M. H. Niemz, "Selfstarting femtosecond operation and transient dynamics of a diode-endpumped Cr:LiSGaF laser with a semiconductor saturable absorber mirror", Applied Physics B. 65, 783-787, 1997.

[86] R. Mellish, S. C. W. Hyde, N. P. Barry, R. Jones, P. M. W. French, J. R. Taylor, C. J. van der Poel, and A. Valster, "All-solid-state diode-pumped Cr:LiSAF femtosecond oscillator and regenerative amplifier", Appl. Phys. B 65, 221-226, 1997.

[87] Klass Wynne, Gavin D. Reid, and Robin M. Hochstrasser, "Regenerative amplification of 30-fs pulses in Ti:sapphire at 5 kHz", Optics Letters, Vol. 19, No. 19, 895-897, 1994.

[88] C. H. Brito Cruz, P. C. Becker, R. L. Fork, and C. V. Shank, "Phase correction of femtosecond optical pulses using a combination of prisms and gratings", Optics Letters, Vol. 13, No. 2, 123-125, 1988.

[89] D. Strickland, G. Mourou: Opt. Commun. 56, 219, 1985.

[90] F. Gires and P. Tournois, Compt. Rend. Acad. Sci. (Paris), 258, 6112, 1964.

[91] D. W. Fradin, N. Bloembergen, and J. P. Letellier, "Dependence of laser-induced breakdown field strength on pulse duration," Appl. Phys.Lett. **22**, 635-631, 1973.

[92] E. W. van Stryland, M. J. Soileau, A. L. Smirl, and W. E. Williams, "Pulse-width and focal-volume dependence of laser-induced break-down," Phys. Rev. B. **23**, 2144-2151, 1981.

[93] D. Stern, R. W. Schoenlein, C. A. Puliafito, E. T. Dobi, R. Bimgmber, and J. G. Fujimoto, "Comeal ablation by nanosecond, picosecond, and femtosecond lasers at 532 and 625 nm," Arch. Ophthalmol. **1,** 587-592, 1989.

[94] F. H. Loesel, A.-C. Tien, S. Backus, H. Kapteyn, M. Murnane, R. M. Kurtz, S. Sayegh, and T. Juhasz, "Effect of reduction of laser pulse width from 100 ps to 20 fs on the plasma-mediated ablation of hard and soft tissue," in Thermal Therapy, Laser Welding, and Tissue Interaction, Stephen G. Bown; Guy P. Delacretaz; Guilhem Godlewski; Gerhard J. Mueller; Roberto Pini; Hans-Dieter Reidenbach; Rudolf W. Steiner; Lars O. Svaasand; Karl-Goran Tranberg; eds. Proc. SPIE 3565**,** 116-123, 1999.

[95] Ron M. Kurtz, Xinbing Liu, Victor M. Elner, Jeffrey A. Squier, Detao Du, Gerard, and A. Mourou, "Photodisruption in the Human Cornea as a Function of Laser Pulse Width", Journal of Refractive Surgery, Vol. 13, 653-658, 1997.

[96] William T. Ham. Jr., Harold A. Mueller, Arnold I. Goldman, Brian E. Newnam, L. M. Holland, and T. Kuwabara, "Ocular hazard from picosecond pulses of Nd:YAG laser radiation", Science, Vol. 185(26), 362-363, 1974.

[97] Arnold I. Goldman, William T. Ham Jr, and Harold A. Mueller, "Mechanisms of Retinal Damage Resulting from the Exposure of Rhesus Monkeys to Ultrashort Laser Pulses", Experimental Eye Research, Vol. 21(5), 457-469, 1975.

[98] Clarence P. Cain, Cyntbia A. Totb, Gary D. Noojin, Val Carotbers, David J. Stolarski, and Benjamin A. Rockwell, “Thresholds for Visible Lesions in the Primate Eye Produced by Ultrashort Near-Infrared Laser Pulses”, Investigative Ophthalmology & Visual Science, Vol. 40 (10), 2343-2349, 1999.

[99] W. Denk, J. H. Strickler, and W. W. Webb, “Two-Photon laser scanning fluorescence microscope”, Science 248, 73-76, 1990.

[100] Meng Han, AlmutBindewald-Wittichc, Frank Holzc, Sarah Snyderb, GuenterGiesed, Hui Sun, Olivier La Schiazz, Michael Agopov, Markolf H. Niemza, and Josef F.Bille, “Confocal and two-photon excited autofluorescence imaging of human retinal pigment epithelial cells”, Accepted by Journal of Biomedical Optics.

[101] J. X. Chen, Y. K. Jia, G. F. Zheng, and X. S. Xie, “Laser-scanning coherent anti-Stocks Raman scattering microscope and applications to cell biology”, Biophys. J. 83, 502-509, 2002.

[102] G. H. Patterson, and D. W. Piston, “Photobleaching in two-photon excitation microscope”, Biophys. J. 78, 2159-2162, 2000.

[103] Wang yanyan, Han meng, Sun hui, Josef Bille, and Ren qiushi, “Second harmonic generation microscopy imaging of cornea after femtosecond laser intrastromal ablation”, Acta Laser Biology Sinica, Vol 14, No.5, 321-326, 2005.